SYNTHESIS AND CHARACTERIZATION OF CERIUM OXIDE NANOPARTICLES AND THEIR COMPOSITES

Thesis submitted to Mahatma Gandhi University
in partial fulfilment of the requirements for the degree of
Doctor of Philosophy in Physics
Under the Faculty of Science

By

BABITHA K KUNIYIL

Under the Supervision of

Dr. THOMAS VARGHESE

LEAD KINDLY LIGHT

DEPARTMENT OF PHYSICS
NEWMAN COLLEGE, THODUPUZHA

October 2017

Dr. Thomas Varghese
Associate Professor
Dept. of Physics
Nirmala College, Muvattupuzha
www.nsrc.in
email:tv@nirmalacollege.ac.in

Certificate

This is to certify that the thesis entitled **SYNTHESIS AND CHARACTERIZATION OF CERIUM OXIDE NANOPARTICLES AND THEIR COMPOSITES** is an authentic record of the original research work carried out by **Ms. Babitha K Kuniyil** in the Research Department of Physics, Newman College, Thodupuzha, under my guidance in partial fulfilment of the requirements for the award of the degree of Doctor of Philosophy, under the faculty of Science of Mahatma Gandhi University, Kottayam. The work presented in this thesis has not been submitted for any other degree or diploma earlier. It is also certified that **Ms. Babitha K Kuniyil** has fulfilled the course requirements for the Ph.D degree of the university.

Muvattupuzha
October 2017

Dr. Thomas Varghese
(Supervising Teacher)

Declaration

I hereby declare that the present work entitled ***SYNTHESIS AND CHARACTERIZATION OF CERIUM OXIDE NANOPARTICLES AND THEIR COMPOSITES*** *is a bonafide report of the original research work done by me under the supervision of Dr. Thomas Varghese, in the Department of Physics, Newman College, Thodupuzha, Kerala in partial fulfilment of the requirements for the degree of Doctor of Philosophy in Physics. The work is original and has not been submitted earlier for the award of any degree or diploma of any other university or institution.*

Thodupuzha ***Babitha K Kuniyil***

October 2017

Acknowledgement

'Knowledge is power'

I feel great pride as I take this opportunity to express a token of gratitude to various persons who helped me in my endeavor of completing this research work. First and foremost, I bow before God Almighty for his blessings bestowed upon me in the accomplishment of this research work.

I wish to pay my deep sense of gratitude and profound thanks to Dr. Thomas Varghese, my guide, for his excellent guidance, encouragement, inspiring suggestions and constant help provided to me in carrying out of this research. I appreciate his unfailing support during incessant days of my research without which I could not have completed this work successfully.

It has been an honour and a privilege to express my gratitude to Rev. Dr. Vincent Joseph, Principal, Newman College, Thodupuzha and Dr. T. M. Joseph, Principal, Nirmala College, Muvattupuzha, who gave me a great opportunity to carry out my research work at these colleges.

I express my indebtedness towards Vice Chancellor, MG University, Kottayam for providing me the support and an opportunity to do my research under MG University. I

gratefully remember Dr.Beena Mathew, Research Director, MG University. I thankfully acknowledge all the members in the research division, MG University, Kottayam for their valuable academic advice and instructions throughout my study.

It is with a deep sense of reverence, I thank Ms. Rajeena Joseph, Head of the Department of Physics, Newman College; Ms. Susan Varghese, Head of the Department of Physics, Nirmala College; and the former Heads and faculty members of the Department of Physics for their immense support. I remember with gratitude all the faculty members and staff, Department of Physics of these two colleges.

I dearly reminisce all the friends of the NSRC family who helped me in my struggle to complete my Ph.D. I am also grateful to Mr. N Aloysius Sabu, Associate Professor, Department of Physics, Nirmala College, Muvattupuzha for his help and support. Words fail me, as I thank Ms. K P Priyanka, Ms. A Sreedevi, Ms. P. A. Sheena, Ms. Seenamol Stephen Ms. H Hitha and Ms. Anjaly Jose for their love, care, help and support. I remember with great gratitude the aid rendered by Mr. Boby Sabu and Mr. Muhammed M.H.

I greatly acknowledge Dr. M S Rintu and Ms. Viji, Maharajas college Ernakulam; Dr. S Sankararaman, University of Kerala, Trivandrum; Dr.J.K.Thomas and Bincy Abraham Department of Physics, Mar Ivanios College, Thiruvananthapuram; Ms. Ambili, Department of Micro biology, Calicut University for their help in material characterization.

I would like to take this opportunity to acknowledge M.G. University, Kottayam, STIC CUSAT, SAIF-IIT Madras, Maharaja's College, Microtron Centre Mangalore University, U.C.College, Aluva and Department of Microbiology Calicut University for various experimental measurements. I wish to thank the reviewers of my articles and their critical comments that helped me to improve the quality of the work presented in the thesis.

I also take this opportunity to thank all my school and college teachers. I would like to acknowledge all the members of Vidya family (Vidya Academy of Science and Technology, Thrissur). I would like to include a special note of thanks to Ms.Julia, Ms. Alphonsa and Ms.Jolly for their help and support.

I express my heartfelt gratitude to my family as they have always been there as a constant source of

encouragement and moral support and whose love and prayers enabled me to reach this mark in my life. I dearly dedicate my thesis to the memory of my achan, who first held my arms and led me to the world of letters and always believed in my ability to be successful wherever l go. Your absence still and will always hurt me, but your memories will stay in my heart forever.

I am deeply and forever indebted to Dwaraka and Sreevalsam. I do not have words to express my affection and gratitude to my beloved parents and my loving siblings Kavitha and Nibin, who are the real propellants behind me. Their love, support and constant patience have taught me so much about sacrifice, discipline and compromise. I owe a great debt of gratitude to my better half Mr. Krishna Prasad for his immense understanding and support during the research period, that helped me to complete the research work on time.

Our little prince Karthikeyan came into our world during my research career, and immensely inspired me to work harder and ensure timely delivery of my thesis. I can not thank him enough for showing lot of patience so that I could concentrate on my work. It is my great pleasure to thank those who helped me to make this thesis possible.

Babitha. K. Kuniyil

Dedicated to

The Memory of My Achan

CONTENTS

PREFACE

Nanomaterials have received tremendous attraction in the field of research due to its high surface area to volume ratio and unique quantum confinement nature, which makes the system highly reactive and changes the properties of materials. Among the different metal oxide semiconductors, CeO_2 has gained substantial interest because of its distinct characteristics and multiple applications.

Method of synthesis plays a major role in the properties of nanomaterials. In order to understand the novel properties of nanophase CeO_2, a better morphological control is necessary. Chemical environment is also important. All these can be tailored by proper synthesis methods. Several researchers reported synthesis and properties of ceria prepared by different routes. During this thesis we have analyzed in detail the room temperature precipitation method for cerium oxide nanoparticle synthesis because of its relatively low cost, good reproducibility, simple mode of operation and ease of mass production. Calcination process also has remarkable

importance in the synthesis of nanoceria. More attention has been paid towards the changes in the structural, optical and electrical properties of nanoceria due to calcinations.

Most of the studies reported in the literature for other materials prove that the electron beam irradiation is an efficient method to improve the structural, optical and electrical performance of nanomaterials. However, no studies have been reported on the effect of electron beam irradiation on the properties of CeO_2 nanoparticles.Hence, we put a special emphasis on the dose dependent effect of electron beam irradiation on the properties of cerium oxide nanoparticles.

Literature report shows that, till date, no studies have been reported on the structural, optical and electrical properties of CeO_2/CoPc and CeO_2/SnPc nanocomposites. Hence, more extensive and systematic studies are required to explore the properties of CeO_2 nanoparticles and CeO_2 based phthalocyanine nanocomposites. Details about the synthesis of CeO_2/CoPc and CeO_2/SnPc nanocomposites by solvent evaporation method and the results of the

structural and functional characterization are also incorporated in this thesis.

The works presented in this thesis are focused on the study of synthesis and characterization of CeO_2 nanoparticles, CeO_2/CoPc and CeO_2/SnPc nanocomposites. The effect of electron beam irradiation on the properties of nanoceria is also investigated. The proposed thesis entitled "**SYNTHESIS AND CHARACTERIZATION OF CERIUM OXIDE NANOPARTICLES AND THEIR COMPOSITES"** consists of seven chapters.

Chapter 1 presents a general introduction on nanomaterials and cerium oxide nanoparticles. A brief survey of the investigations on cerium oxide nanoparticles and objectives of the present work are delineated in this chapter. In Chapter 2, synthesis methods adopted for the fabrication of CeO_2, CeO_2/CoPc and CeO_2/SnPc, and characterization techniques used for their studies are described.

Chapter 3 presents the properties of cerium oxide nanoparticles synthesized by chemical precipitation

method. The effect of calcination temperature on the structural, electrical and optical properties of cerium oxide nanoparticles is also discussed in the chapter. In Chapter 4, dose dependent effect of 8 MeV electron beam irradiation on the structural, optical and electrical properties of nanoceria is discussed.

Chapter 5 and 6 present the synthesis and characterization of CeO_2/CoPc and CeO_2/SnPc nano composites respectively. The effect of CoPc and SnPc on the structural, electrical and optical properties of cerium oxide is also detailed. The summary of the major findings along with a brief report of the future prospects is presented in chapter 7.

The work presented in this thesis has either been published in or communicated to national/international journals or conference proceedings.

PUBLICATIONS

1. CeO_2/CoPc nanocomposite for potential applications in electronics, **K.K. Babitha**, K.P. Priyanka, H. Hitha, S. Rintu Mary, E.M. Mohammed, S. Sankararaman and Thomas Varghese, ***Journal of electronic materials***, Springer (2017); doi: 10.1007/s11664-017-5653-z.

2. Studies on the structural, optical and electrical properties of CeO_2/SnPc nanocomposite for electronic applications, **K. K. Babitha**, K. P. Priyanka, A. Sreedevi, Bincy Abraham, J. K. Thomas and Thomas Varghese, ***Journal of Material Science: Materials in Electronics,*** Springer, 28 (2017) 1115–1123; doi:10.1007/s10854-016-5636-5.

3. Structural modifications and extended spectral response of CeO_2/CoPc nanocomposites for potential applications, **K. K. Babitha**, K. P. Priyanka, A. Sreedevi, O. P. Jaseentha and Thomas Varghese, ***International Journal of Applied Ceramic Technology***, Wiley,13 (2016) 670-677; doi:10.1111/ijac.12542.

4. Structural characterization and optical studies of CeO_2 nanoparticles synthesized by chemical precipitation**, K. K Babitha**, A. Sreedevi, K. P. Priyanka, Boby Sabu and Thomas Varghese, ***Indian Journal of Pure and Applied Physics,*** 53(9) (2015) 596-603.

5. Effect of 8 MeV electron beam irradiation on the structural and optical properties of CeO_2 nanoparticles, **K. K. Babitha**, K. P. Priyanka, A. Sreedevi, S. Ganesh and Thomas Varghese, ***Materials Characterization***, Elsevier, 98 (2014) 222–227; doi: 10.1016/j.matchar.2014.11.004.

6. Chemical synthesis, structural characterization and electrical studies of nanoceria for CMOS applications, K. P. Priyanka, **K. K. Babitha,** A. Sreedevi, X. Sheena, E. M. Mohammed and Thomas Varghese, ***Journal of Electroceramics,*** Springer, 32(4) (2014) 361-368; doi: 10.1007/s10832-014-9919-z.

PAPERS PUBLISHED OTHER THAN THIS WORK

1. Synthesis and Characterization of Silver Tungstate/Iron Phthalocyanine Nanocomposite for Electronic Applications, A. Sreedevi, K. P. Priyanka, **K. K. Babitha**, S. Sankararaman and Thomas Varghese, ***The European Physical Journal B***, Springer, 90 (2017) 102-113; doi: 10.1140/epjb/e2017-80149-9.

2. Structural and optical modifications of the Ag_2WO_4/CoPc nanocomposite for potential applications, A. Sreedevi, K. P. Priyanka, **K. K. Babitha**, O.P. Jaseentha and Thomas Varghese, ***European Physical Journal Plus,*** Springer,131(2016) 7. doi: 10.1140/epjp/i2016-16007-9.

3. Influence of Electron Beam Irradiation on Structural and Optical Properties of α- Ag_2WO_4 Nanoparticles, A. Sreedevi, K. P. Priyanka, **K. K. Babitha**, Ganesh Sanjeev and Thomas Varghese, ***Micron,*** Elsevier, 88 (2016) 1-6;
doi: 10.1016/j. micron.2016.05.003.

4. Chemical Synthesis, Structural Characterization and Optical Properties of Nanophase α- Ag_2WO_4, A. Sreedevi, K. P. Priyanka, **K. K. Babitha**, N. Aloysius Sabu, T. S. Anu and Thomas Varghese, ***Indian Journal of Physics,*** Springer, 89(9) (2015) 889-897; doi: 10.1007/S12648-015-0664-1.

BOOK CHAPTERS PUBLISHED

1. CeO_2/CoPc-A novel nanocomposite for potential applications, **K.K. Babitha**, K. P. Priyanka, A. Sreedevi, O.P. Jaseentha, Thomas Varghese, In: V. Rajendran, R. Suriyaprabha and K.E.Geckeler (Eds.), **Industrial Applications of Nano structured Materials,** Bloomsbury Publi. (2015) 89-92.

PRESENTATIONS

1. Synthesis and characterization of ceria based cobalt phthalocyanine nanocomposite, **K.K. Babitha**, K.P. Priyanka, A. Sreedevi and Thomas Varghese, National conference on technologies behind nanoscience (NCTN-2016), 22-23 January (2016), Mar Athanasius College, Kothamangalam, Kerala.

2. CeO_2/CoPc-A novel nanocomposite for potential applications, **K. K. Babitha**, K. P. Priyanka, A. Sreedevi, O. P. Jaseentha and Thomas Varghese, International conference on nanomaterials-NANO-15, 7-10 December (2015), KSRCT campus, Thiruchengode, Tamilnadu, India.

3. Dielectric studies of TiO2/CoPc nanocomposite with varying frequency, K.P. Priyanka, **K. K. Babitha**, A. Sreedevi and Thomas Varghese, Seventh International Conference on Smart Materials Structures & Systems (ISSS-2014), 8-11 July (2014), Indian Institute of Science, Bangalore, India.

LIST OF FIGURES

LIST OF TABLES

Table No.	Title	Page No.

LIST OF ABBREVIATIONS

CIE	International Commission on Illumination (Commission Internationale de l'Eclairage)
DTA	Differential Thermal Analysis
DTG	Differential Thermo Gravimetry
EB	Electron Beam
EDX	Energy Dispersive X-ray Spectroscopy
FTIR	Fourier Transform Infrared Spectroscopy
FWHM	Full Width at Half Maximum
HRTEM	High Resolution Transmission Electron Microscopy
Hz	Hertz
JCPDS	Joint Committee on Powder Diffraction Standards
kGy	kilogray
nm	Nanometer
PL	Photoluminescence
SAED	Selected Area Electron Diffraction
SEM	Scanning Electron Microscopy
TEM	Transmission Electron Microscopy
TGA	Thermo Gravimetric Analysis
UV-Vis	UV-Visible
XRD	X-ray Diffraction

Chapter 1
INTRODUCTION

1.1 Nanoscience and nanotechnology

Nanoscience and nanotechnology have received tremendous scientific attention because of the novel physiochemical properties of nanophase materials. Nanoscience is an emerging and enabling field which involves the feasibility of creating nanomaterials with high reactivity and size (shape) dependent properties. The impact of nanotechnology in human life is greatly appreciated. Synthesis of nanoparticles with a better control over its size and shape, characterization of their properties and analysis of these data along with the theoretical explanations are necessary for understanding the nanoscale phenomena of materials. The potential of nanotechnology can contribute more advancement in various fields including electronics, material science, medicine, biotechnology, environment and information technology.

Nanomaterials have been defined by the European Commission as "a natural, incidental or manufactured material containing particles, in an unbound state or as an aggregate or as an agglomerate and where, for 50% or more of the particles in the number size distribution, one or more

external dimensions is in the size range 1-100nm" (*European Commission, 2011/696/EU*). The nanoparticles have large surface area to volume ratio due to their small size, which results in higher reactivity and unique surface properties.

The structural, thermal, optical, electrical, mechanical and magnetic properties of a material are modified in this state of matter and are superior to its bulk form. In addition to high aspect ratio, quantum confinement is also responsible for these modifications.

1.2 Cerium oxide nanoparticles

Metal oxides play a very important role in diverse areas of chemistry, physics and material science [1,2]. Oxide nanoparticles can exhibit unique physical and chemical properties due to their small size and a high density of corner or edge surface atoms. Cerium oxide is a requisite material in this category due to its multiple applications in the areas of catalysis, electrochemistry, photochemistry and material science. Nanophase cerium oxide (nanoceria) is a very interesting material because of its ability to buffer electrons from an oxidant or reducing environment due to the unfilled *4f* electronic structure.

Cerium is a lanthanide series rare earth element. Elemental cerium was first discovered from a mineral named “cerite” by Jons Jakob Berzelius and Wilhelm Hisinger in Sweden [3]. Elemental cerium is an

iron-gray, ductile and malleable metal [4]. Cerium can exist either in the free metal or oxide form, and can cycle between the cerous-cerium (Ce^{3+}) and ceric-cerium (Ce^{4+}) oxidation states [5]. This property provides several technological uses. The most stable oxide of cerium is cerium dioxide, CeO_2, also called ceria or ceric oxide. Ceria is a nontoxic, inorganic and n-type semiconductor with wide band gap. Bulk CeO_2 has a cubic fluorite structure with lattice constant of 0.5411 nm at 300 K [6]. In the fluorite structure each cerium site is surrounded by 8 oxygen sites in FCC arrangement and each oxygen site has a tetrahedron cerium site. Crystal structure of cerium oxide is presented in Fig.1.1. Ceria has only one crystallographic form throughout the range of temperatures. This material has a strong tendency to remain in the fluorite structured lattice even after losing considerable amount of oxygen, thus stabilizing a structure with an elevated number of oxygen vacancies [7]. Experimental and theoretical studies indicate that CeO_2 is described as an ionocovalent compound or covalent insulator. Some important crystallographic properties of cerium oxide are presented in Table 1.1.

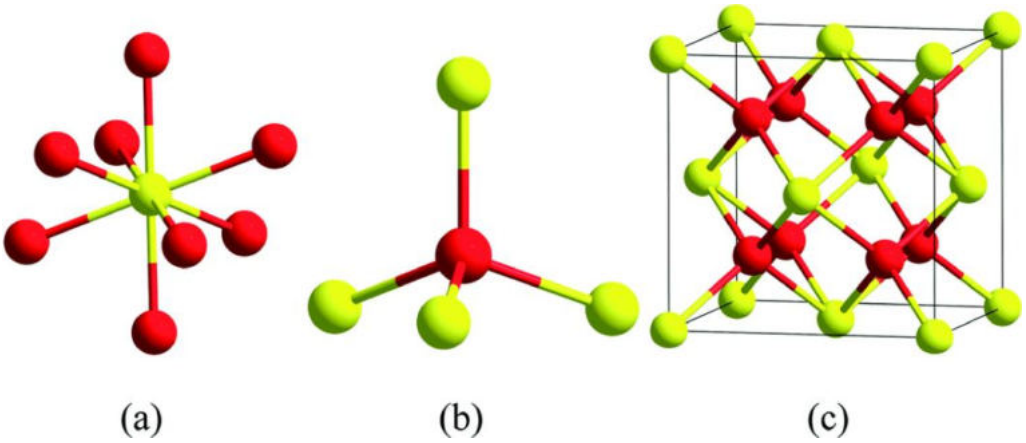

Fig.1.1 Crystal structure of cerium oxide: (a and b) eight-fold coordinated cerium atoms (yellow) with four-fold coordinated oxygen atoms (red) in ceria crystals, (c) the primitive unit cell [8]

Table1.1 Properties of cerium oxide [8-11]

Crystal system	Cubic (fluorite)
Appearance	Pale yellow solid
Space group	Fm3m, #225
Density (g/cm^3)	7.21g/cm^3
Melting point	2400^{o}C
Dielectric constant (room temperature)	52
Optical band gap (eV)	3.19eV

Comparing with bulk cerium oxide, nanoceria consists of large number of oxygen vacancy defects, which will improve the performance of the material. Because of its ability to alter its oxidation state, cerium oxide creates oxygen vacancies or surface defects by loss of either

electron or oxygen [12,13]. Oxygen atoms in CeO_2 have good mobility and are ready to leave the ceria lattice fast, and produce a large number of non-stoichiometric oxides with CeO_2 and Ce_2O_3. The amazing properties of nanoceria include UV absorbing ability [14], high thermal stability [15], facile electrical conductivity and diffusivity [16], high hardness, specific chemical reactivity [17], large oxygen storage capacity with ability to store and transport oxygen [18], high refractive index, and expedient mutation of the oxidation state of cerium between Ce(III) and Ce(IV) [5]. These properties make nanoceria a promising candidate in glass polishing materials [19], UV-blockers and filters [20-22], automotive exhaust promoter [23,24], as a coating for corrosion protection for metals and alloys [25,26], as an additive in glass to protect light-sensitive material [27], as an oxidation catalyst [28], as an oxygen ion conductor in solid oxide fuel cells [29], electrolyzers [30], oxygen pumps and amperometric monitors [31], an effective high temperature oxidation resistant coating [32], sunscreens [33], solid electrolytes [34], additives in ceramics [35], abrasive of the chemical mechanical planarization (CMP) slurry in semiconductor fabrication [36], selective hydrogenation catalysis of unsaturated compounds [37,38], photocatalytic oxidation of water [39], as an anode material for lithium ion battery system [40], buffer layers with silicon wafer [41], gates for metal-oxide semiconductor device [42], solar cells [43], low-temperature water gas shift catalyst [44], free-radical scavenger [45], removal of soot

from diesel engine exhaust [46], removal of organics from wastewater [47], water splitting for the generation of hydrogen gas [48], photo-degradation of toluene in the gas phase [49], photocatalytic behavior under sunlight irradiation to degrade dyes [50,51], protective of primary cells from the detrimental effects of radiation therapy [52], neuro-protection to spinal cord neurons and prevention of retinal degeneration induced by intercellular peroxide [53], potent antioxidant in cell culture model [54] and gas sensor [55].

A wide range of synthesis methods have been reported for the preparation of cerium oxide nanoparticles. Based on the method of preparation and the oxidation state of cerium in the precursor salt, the amount of O vacancies and the presence of Ce^{3+} in a ceria nanoparticle can change. Since Ce^{3+} is larger than Ce^{4+} (atomic sizes 1.14 and 0.97 Å, respectively), the presence of O vacancies increase the size of the unit cell and distort it. In addition to this, structural imperfections and surface defects present in the ceria nanoparticles introduce strain in the lattice. These O vacancies and defects present in ceria nanoparticles can lead to special electronic properties, introducing electronic states within the band gap of the oxide. Ceria particles with diameters of less than 10 nm have a substantially higher electronic conductivity than bulk ceria. Nanoceria shows very strong absorption in the UV region and emission in the blue region of the visible spectrum. The methods of synthesis,

properties, and applications of CeO_2 and CeO_2 based materials have been covered in a number of excellent reviews and extensive studies have been conducted on this topic. A brief survey of some of the important studies related to nanoceria, ceria based nanocomposite and effect of electron beam (EB) irradiation on the properties of nanomaterials are presented below.

1.3 Literature survey

1.3.1 Synthesis of CeO_2 nanoparticles

In recent years, significant advancements have been achieved in synthesis methods and characterization techniques of nanomaterials. Numerous methods have been adopted to prepare pure nanoceria and ceria based nanocomposites, based on both top-down and bottom-up methods, including laser processing and milling [56], chemical vapour deposition [57], coprecipitation [58], sol-gel methods [59], spray pyrolysis [60], microemulsion methods [61], hydrothermal synthesis [62], thermal hydrolysis [63], flux method [64], solvothermal method [65], sonochemical method [66], reverse micellar synthesis [67], precipitation [68, 69], thermal decomposition [70], oxidant precipitation [71], electrodeposition [72], microwave technique [73], combustion synthesis [74], gas condensation method [75], mechano-chemical method [76], composite hydroxide method [77], wet chemical synthesis, polymer method [79], electrochemical method [80], low temperature

decomposition method [81], polyol method [82] and freeze drying [83]. Among these methods, the precipitation technique has attracted extensive attention, because it is comparatively simple, scalable and inexpensive [84]. This method involves simultaneous occurrence of nucleation, growth, coarsening and agglomeration processes, which will dramatically affect the size, morphology and properties of the product [85]. In addition to this, type of cerium source has a great effect on the morphology of the final product.

Literature reports show that inorganic cerium salt such as, $Ce(NO_3)_3$, $CeCl_3$, $(NH_4)_2Ce(NO_3)_6$ can be used as cerium precursors for the synthesis of nanoceria [86-90]. It is reported that cerium source from nitrate is most favourable for the formation of uniformly sized cerium oxide nanoparticles [91-95]. It can be seen that the concentration of precursors, reaction temperature, pH and the rate of addition of precipitating agent are the main factors influencing the particle size and morphology of ceria nanoparticles [95]. Djuricic and Pickering synthesized nanocrystalline powders of cerium oxide from cerium(III) nitrate solution through a two-stage precipitation process which yielded weakly-agglomerated powders with a crystallite size smaller than 5 nm. Hydrogen peroxide was added to cerium nitrate at 5°C to slowly oxidize Ce^{3+} to Ce^{4+} [96].

1.3.2 Properties of CeO_2 nanoparticles

In nanoceria, decrease of particle size leads to the production of more oxygen vacancies [97]. Hailstone and his team observed a systematic lattice expansion in ceria when its particle size is decreased to nanoscale. A large fraction of cerium atoms occupy the fully reduced state in ultra-small-sized (1.1 nm) ceria nanoparticle, even though the ceria nanoparticles retain a cubic-shaped lattice [98]. The lattice expansion in nanoceria is due to the increased concentration of point defects with decreasing particle size [99].

Kamruddin *et al* have studied the structural properties of nanoceria. They found that nanoceria exhibit stable fluorite structure [100]. Deshpande *et al* established the correlation between the particle size and the lattice parameters in nanoceria. The variation in lattice parameters is attributed to the lattice strain induced by the introduction of Ce^{3+} due to the formation of oxygen vacancies [101]. Feng Zhang has suggested that the larger lattice parameter in nanocrystalline ceria results in a higher ionic conductivity and more efficient fuel cells [102]. The systematic increase in lattice parameter with decrease in particle size provides specific control of the surface oxygen spacing [102, 103]. Anwar Ali *et al* (2017) reported the synthesis and properties of CeO_2 nanoparticles by thermal treatment [104].

The effect of calcination temperature on the growth of CeO_2 nanoparticles synthesized by different techniques were reported in the literature [94,105-111]. Neto and Schmal confirmed that increase in calcination temperature leads to an increase in the concentration of Ce^{+3} species, which results in enhancement of oxygen vacancies [112]. Chen *et al* studied the effects of reaction temperature and atmosphere on the properties of CeO_2 particles [113]. Sujana *et al* have reported the characterization of nanoceria particles synthesized by surfactant-mediated precipitation technique [114].

Tao *et al* have reported that the intensity of PL emission increased sharply when the morphology of ceria changed from nanoparticles to nanowires [115]. Yang *et al* reported that CeO_2 nanocubes exhibit excellent reducibility and high oxygen storage capacity [116]. Zhaoxia *et al* have synthesized a series of cerium oxide nanorods and nanowires with precisely controlled lengths and aspect ratios [117]. Chunwen Sun *et al* observed that the UV–visible absorption spectrum and photoluminescence spectrum of the CeO_2 nanorods synthesized by solvothermal route have unusual red-shift and enhanced light emission [118].

The Raman active modes of ceria are attributed to a symmetrical stretching mode of the Ce-O8 vibrational unit, and therefore, they are very sensitive to any disorder in the oxygen sub-lattice [119]. The first

order Raman line at around 465 cm^{-1} corresponds to the triply degenerate Raman active optical phonon mode (F_{2g}) [10,120]. Decreased phonon lifetime with smaller grain size is the main reason for the broadening effect in Raman spectra [121-123].

In nanomaterial, reduction in particle size will affect optical absorption and emission properties in a superior manner. The calculations of quantum size effect establish that there are no significant variations in the chemical composition of metal oxide as a result of particle size reduction [124]. According to Bensalem *et al,* the spacing of the electronic levels and the band gap energy (E_g) are highly dependent on the particle size [125]. The mechanism of absorption is a $Ce^{+4} \leftarrow O^{2-}$ charge-transfer optical transition. Tsunekawa *et al* have observed blue shift in the ultraviolet absorption spectra in cerium oxide nanocrystallites [126]. Reduction in particle size in ceria leads to an enhanced optical absorption in the ultraviolet region and a blue shift in the absorption spectra. Tsan Liu *et al* observed a red shift in the UV absorption band with increase in calcination temperature [127]. The optical band gap of nanoceria is 3.65 eV and that of CeO_2 calcined at 550^{o}C is 3.5 eV [127].

Room temperature PL emission of nanoceria is in the blue region. The emission bands ranging from 400 to 500 nm for cerium oxide samples are attributed to the hopping from different levels of *Ce 4f*

and *O 2p* band (valence band) [86,128]. Sathyamurthy *et al* observed strong UV absorption and room temperature photoluminescence for cerium oxide nanoparticles with an average particle size of 3.7 nm. The photoluminescence peak is sensitive to the particle concentration and shows a blue-shift upon dilution [129].

Bojana *et al* reported violet emission at 427 nm (excitation at 356 nm) which corresponds to $5d^1 \rightarrow 4f^1$ transition of cerium trivalent ion. The observed spectral blue shift revealed the presence of fine crystallites [130].

Ansari observed quantum size effect in the absorption spectra of CeO_2 films with a direct band gap of 3.23 eV. The photoluminescence spectra of the films showed a strong band at 378 nm [131]. Maksimchuk *et al* have reported the occurrence of two different luminescence centers (viz. the charge transfer complexes formed by Ce^{4+} and O^{2-} ions and Ce^{3+} ions stabilized by vacancies) in cerium oxide nanoparticles [132].

Dielectric behavior of cerium oxide strongly depends on temperature and frequency. The dielectric constant and the dielectric loss of cerium oxide nanoparticles is found to decrease with increase in frequency [10, 120]. When compared with microcrystalline ceria, nanocrystalline ceria materials show enhanced electronic conductivity. Suzuki *et al* observed the transition from extrinsic to intrinsic type of

conductivity as the grain size decreased to <100 nm, which is attributed to a decrease in the enthalpy of oxygen vacancy formation in CeO_2 [12]. It has been reported that the nature of bonds present in CeO_2 is polarized ionic [133].

The electronic conductivity of nanocrystalline samples is larger than the intrinsic electronic conductivity of pure single crystalline cerium oxide and is increasing with decrease in grain size [134]. Takenori theoretically investigated the dielectric properties of fluorite CeO_2 [135]. Zhao *et al* suggested that the tuning properties for improved frequency dispersion can be achieved by controlling the grain size and hence the strain at the nanoscale dimensions [121].

1.3.3 CeO_2 based nanocomposite

Nanocomposites, a high performance material, exhibit unusual property combinations and unique design possibilities [136]. Nanocomposites based on CeO_2 with various materials have drawn much interest because of their magnetically induced optical and electrical properties. Recently, the synthesis of organic–inorganic nanocomposite materials have attracted substantial attention from various researchers due to its potential to combine distinct physical properties of organic and inorganic components [137].

There are several reports available on the synthesis, properties and applications of cerium oxide based nanocomposites. Ansari *et al* studied the optical and electrical properties of electrochemically deposited

polyaniline/cerium oxide hybrid nanocomposite film onto indium-tin-oxide (ITO) glass substrate [137]. Wang *et al* synthesized cerium oxide/montmorillonite nanocomposite and studied its structural and mechanical properties [138].

It is reported that the nanocomposites have significantly high dielectric constant and comparatively low dielectric loss facilitating its use as a high-k dielectric material for embedded capacitor applications [139]. Saranyoo *et al* prepared $BiVO_4/CeO_2$ nanocomposites with rod-like, plate-like and spheroidal shapes[140]. Maria *et al* synthesized CeO_2/Y_2O_3 nanocomposites by hydrothermal method and studied its photocatalytic and antibacterial activities [141]. Structural and optical properties of polyvinyl alcohol–cerium oxide nanocomposite films have been reported by Hemalatha and Rukmani [142]. The UV-Visible spectrum of the composite exhibits a red shift in the optical band gap with respect to pure PVA, and both red and blue shift with respect to nano CeO_2 depending on the concentration of the filler [142]. The photoluminescence intensity of the CeO_2– graphene nanocomposite is about 30 times higher than that of pristine CeO2 crystals [143].

The organic materials such as phthalocyanine (Pc) shows high thermal and chemical stability, nontoxicity, semiconductivity and interesting optical properties [144]. Due to the semiconducting properties, metal phthalocyanines (M-Pc) are promising candidates for

photovoltaic devices, photodetectors, organic transistors, organic electroluminescence devices and sensors [145]. Large number of works were reported on the synthesis, properties and applications of M-Pcs. Nanocomposite based on ceria with metal phthalocyanine (M-Pc) is an inorganic-organic hybrid system. Pawan Kumar *et al* synthesized tin phthalocyanine (SnPc)/mesoporous ceria (CeO_2) nanocomposite and used as photocatalyst for CO_2 reduction under visible light [146]. However, the studies on electrical properties of cerium oxide/ tin phthalocyanine (CeO_2/SnPc) nanocomposite is not available. Literature reports have shown that no studies have been reported on the synthesis and properties of cerium oxide/cobalt phthalocyanine (CeO_2/CoPc) nanocomposite.

1.3.4 Effect of electron beam irradiation

Electron beam (EB) irradiation is a new and efficient method for modifying the optical, electronic, magnetic and mechanical properties for potential applications [147]. Yun *et al* studied the effect of electron beam irradiation on the properties of ZnO film [148]. Studies on the effect of EB irradiation on the properties of nickel oxide nanocubes and α-Ag_2WO_4 nanoparticles were reported [149, 150]. Raghu *et al* reported the effect of EB irradiation on the structural and dielectric properties of polymer electrolyte film [151]. Studies on the use of electron beam irradiation for controlling the surface properties of nanoparticles are

sparse. Few works were reported on the effect of electron beam irradiation on structural and optical properties of nanoparticles [152-155]. The detailed literature survey indicates that no studies are reported for the effect of electron beam irradiation on the properties of nanoceria.

1.4 Motivation

Several studies have been reported on the synthesis and characterization of CeO_2 nanoparticles. However, systematic studies on the structural, optical and electrical properties of cerium oxide/cobalt phthalocyanine and cerium oxide/tin phthalocyanine nanocomposites are sparse. Hence, more extensive and systematic studies on the structural, optical and electrical properties of these nanocomposites are needed. The electron beam irradiation technique can be used to improve the structural, optical and electrical performance of nanoparticles. To date, no studies have been reported on the effect of high energy electron beam irradiation on the properties of nanocrystalline CeO_2. In order to throw more light on the influence of high energy electron beam irradiation on the CeO_2 nanoparticles, systematic investigation based on various characterization tools are required.

1.5 Objectives of the present work

The main objectives of the present investigation are as follows:

- Synthesis of nanocrystalline CeO_2 by chemical precipitation method.
- Investigation of thermal, structural, optical and electrical properties of the synthesized nanophase CeO_2 using various characterization techniques.
- Evaluation of the effect of calcination temperature on the thermal, structural, optical and electrical properties of CeO_2 nanoparticles.
- Study the impact of 8 MeV electron beam irradiation on the structural, thermal, optical and electrical properties of nanophase CeO_2.
- Characterization of CeO_2/CoPc nanocomposite prepared by solvent evaporation method.
- Characterization of CeO_2/SnPc nanocomposite synthesised by solvent evaporation method.

References

[1] C. Noguera, Physics and Chemistry at Oxide Surfaces; Cambridge University Press: Cambridge, UK, (1996).

[2] H. H. Kung, Transition Metal Oxides: Surface Chemistry and Catalysis; Elsevier: Amsterdam, (1989).

[3] https://www.webelements.com/cerium.

[4] O'Neil, The Merck index: an encyclopedia of chemicals, drugs, and biologicals. 13th edition 89(2011) 342–344.

[5] Z. Y. Hu, S. HaneklauS, G. Sparovek and E. Schnug, Commun. Soil. Science Plan., 37(9-10) (2006) 1381.

[6] A. Trovarelli, Catalysis by Ceria and Related Materials, Imperial College Press, UK, (2002).

[7] B. T. Kilbourn, Cerium and cerium compounds; encyclopedia of chemical technology, New York, John Wiley and sons (2003).

[8] Kenneth Reed, Alastair Cormack, Anirudha Kulkarni, Mark Mayton, Dean Sayle,Fred Klaessig and Brad Stadler, Environ. Sci:Nano., 1(2014) 390-405.

[9] https://en.wikipedia.org/wiki/Cerium(IV)_oxide.

[10] D. M. D. M. Prabaharan, K. Sadaiyandi, M. Mahendran, Suresh Sagadevan, Mater. Res., 19 (2) (2016) 478-482.

[11] D. Matsushita, Y. Nishikawa, N. Satou, M. Yoshiki, T. Schimizu, T. Yamaguchi, H. Satake, N. Fukushima, Jpn. J. Appl. Phys., 43(2004) 1795.

[12] T. Suzuki, I. Kosacki, H. U. Anderson, and P. Colomban, J.Am. Ceram. Soc., 84 (9) (2001) 2007-2014.

[13] G. S. Herman, Surface Science, 437 (1-2) (1999) 207-214.

[14] S. Tsunekawa, R. Sahara, Y. Kawazoe, A. Kasuya, Mater. Trans. JIM 41 (2000) 1104–1107.

[15] A. Trovarelli, C. de Leitenburg, M. Boaro, G. Dolcetti, Catal. Today 50 (1999) 353–367.

[16] F. Zhou, X. Zhao, H. Xu, C. Yuan, J. Phys. Chem. C 111 (2007) 1651–1657.

[17] H. I. Chen, H. Y. Chang, Solid State Commun., 133 (2005) 593–598.

[18] A. M. Shahin, F. G. Grandjean, J. Long, T. P. Schuman, Chem. Mater., 17 (2005) 315–321.

[19] E. Bekyarova, P. Fornasiero, J. Kaspar, M. Graziani, Catal. Today, 45 (1998) 179 – 183.

[20] T. Morimoto, H. Tomonaga, A. Mitani, Thin Solid Films, 351 (1999) 61–65.

[21] S. Tsunekawa, T. Fukuda, A. Kasuya, J. Appl. Phys., 87 (2000) 1318–1321.

[22] M. Yamashita, K. Kameyama, S. Yabe, S. Yoshida, Y. Fujishiro, T. Kawai, T. Sato, J. Mater. Sci., 37 (2002) 683–687.

[23] G. R. Rao, P. Fornasiero, R. Di Monte, J. Kaspar, G. Vlaic, G. Balducci, S. Meriani, G. Gubitosa, A. Cremona, M. Graziani, J. Catal., 162 (1996) 1–9.

[24] P. Fornasiero, G. Balducci, R. Di Monte, J. Kašpar, V. Sergo, G. Gubitosa, A. Ferrero, M. Graziani, J. Catal., 164 (1996) 173-183.

[25] A. S. Hamdy, Mater. Lett., 60 (2006) 2633–2637.

[26] X. Zhong, Q. Li, J. Hu, Y. Lu, Corros. Sci., 50 (2008) 2304.

[27] C. Lin, J. D. C. Basil, R. M. Hunia, P. P. Bihuniak, US Patent 1994, 5316854.

[28] M. S. Yakimova, V. K. Ivanov, O. S. Polezhaeva, A. A. Trushin, A. S. Lermontov, Y. D.Tretyakov, Dokl. Chem., 427 (2009) 186-189.

[29] H. Yahiro, Y. Baba, K. Eguchi, H. Arai, J. Electrochem. Soc., 135 (1988) 2077–2081.

[30] O. A. Marina, L. R. Pederson, US Patent, 2008, 7468218.

[31] M. Hirano, E. Kato, J. Am. Ceram. Soc., 79 (1996) 777-780.

[32] S. Patil, S. C. Kuiry, S. Seal, R. Vanfleet, J. Nanoparticles Res., 4 (2002) 433–438.

[33] T. Masut, M. Yamamoyo, T. Sakata, H. Mori, G. Adachi, J. Mater. Chem., 10 (2000) 353–357.

[34] H. Inaba, H. Tagawa, Solid State Ionics, 83 (1996) 1–16.

[35] G. L. Messing, S. C. Zhang, G. V. Jayanthi, J. Am. Ceram. Soc., 76 (1993) 2707–2726.

[36] M. Jiang, N.D. Wood, R. Komanduri, J. Eng. Mater. Technol. Trans. ASME 120 (1998) 304–312.

[37] J. L. G. Fierro, J. Soria, J. Sanz, M.J. Rojo, J. Solid State Chem., 66 (1987) 154–162.

[38] K. S. Sim, L. Hilaire, F. Le Normand, R. Touroude, V. Paul-Boncour, A. Percheron- Guegan, J. Chem. Soc., Faraday Trans., 87 (1991) 1453–1460.

[39] G. R. Bamwenda, H. Arakawa, J. Mol. Catal. A 161 (2000) 105–113.

[40] F. Zhou, X. Ni, Y. Zhang, H. Zheng, J. Colloid, J. Colloid Interface Sci., 307 (2007)135-138.

[41] J. Tashiro, A. Sasaki, S. Akiba, S. Satoh, T. Watanabe, H. Funakubo, M.Yoshimoto, Thin Solid Films, 415 (2002) 272–275.

[42] S .F. Galata, E. K. Evangelou, Y. Panayiotatos, A. Sotiropoulos, A. Dimoulas, Microelectron. Reliab., 47 (2007) 532–535.

[43] A. Corma, P. Atienzar, H. Gara, J.Y. Chane-Ching, Nat. Mater., 3 (2004) 394–397.

[44] S. Hilaire, X. Wang, T. Luo, R.J. Gorte, J. Wagner, Appl. Catal. A: Gen. 215 (2001)271-278.

[45] S. Babu, A. Velez, K. Wozniak, J. Szydlowska, S. Seal, Chem. Phys. Lett., 442 (2007) 405-408.

[46] J. Lahaye, S. Boehm, P.H. Chambrion, P. Ehrburger, Combust. Flame, 104 (1996) 199-207.

[47] Y. I. Matatov-Meytal, M. Sheintuch, Ind. Eng. Chem. Res., 37 (1998) 309-326.

[48] K. H. Chung, D. C. Park, Catal. Today, 30 (1996) 157-162.

[49] M. D. Herna´ndez-Alonso, A. B. Hungrı´a, A. Martı´nez-Arias, M. Ferna´ ndez-Garcı´ a,J.M. Coronado, J.C. Conesa, J. Soria, J. Appl. Catal. B: Environ., 50 (2004) 167-175.

[50] Y. Q. Zhai, S.Y. Zhang, H. Pang, Mater. Lett., 61 (2007) 1863-1867.

[51] P. Borker, A.V. Salker, Mater. Chem. Phys., 103 (2007) 366-370.

[52] R.W. Tarnuzzer, J. Colon, S. Patil, S. Seal, Nano Lett., 5 (2005) 2573-2577

[53] M. Das, S. Patil, N. Bhargava, J.-F. Kang, L.M. Riedel, S. Seal,Biomaterials, 28 (2007) 1918-1925.

[54] S. Patil, A. Sandberg, E. Heckert, W. Self, S. Seal, Biomaterials 28, (2007) 4600-4607.

[55] T. S. Stefanik, H. L. Tuller, J. Eur. Ceram. Soc., 21 (2001) 1967–1970.

[56] V. Alan Chadwick and L. P. Shelley Savin, J Alloys Compd., 488(2009)1-4; doi:10.1016/j.jallcom. 2006.10.164.

[57] Kimberly D. Pollard, Hilary A. Jenkins and Richard J. Puddephatt, Chemistry of Materials, 12(3) (2000)701-710; doi:10.1021/ cm990455r.

[58] C. J. Shih, Y. J. Chen, M. H. Hon, Mater. Chem. Phys., 121(1-2) (2010) 99-102.

[59] L. P .Li, X. M. Lin, G. S. Li and H. Inomata, J Mater. Res., 16(2001)3207-3213.

[60] H. S. Kang, Y. C. Kang, H. Y. Koo, S. H. Ju, D. Y. Kim, S. K. Hong, J. R. Sohn, K. Y. Jung and S. B. Park, Maters. Sci. Eng. B,127(2-3)(2006)99-104 ;doi:10.1016/j.mseb.2005.09. 063.

[61] Yan Mei, Yebin Han, Yan Li, Wei Wang and Zuoren Nie, Mater. Lett., 60(25- 26)(2006)3068-3072.

[62] Y. C. Zhou and M. N. Rahaman, J. Mater. Res. 8 (1993) 1680

[63] G. Renu, V. Divya Rani, S. V. Nair, K .R. V. Subramanian and L. Vinoth Kumar, Advanced Science Letters, 5 (2012) 1

[64] F. Bondioli, A. B. Corradi, C. Leonelli, T. Manfredini, Mat. Res. Bull.34 (14-15) (1999) 2159

[65] E. Kumar, P. Selvaraj and D. Muthuraj, Mat. Res.,16 (2013) 269.

[66] L. Yin, Y. Wang, G. Pang, Y. Koltyp in and A. Gedanker. J Colloid Interface Sci.,246(1) (2002) 78-84; doi:10.1006/jcis.2001.8047.

[67] Toshiyuki Masui, Kazuyasu Fujiwara, Ken-ichi Machida and Gin-ya Adachi, Chem. Mater., 9(10) (1997) 2197–2204; doi**:** 10.1021/cm 970359v.

[68] H. R. Pouretedal, A. Kadkhodaie, Chinese Journal of Catalysis 31 (2010) 1328.

[69] Chanjira Kitiwiang and P. Sukon, J. Microscopy Society of Thailand, 23(2009) 83.

[70] Seung Soo Lee, Huiguang Zhu, Elizabeth Q. Contreras, Arjun Prakash, Hema L. Puppala and Vicki L. Colvinbv, Chem. Mater.,24(3) (2012) 424–432; doi: 10.1021/cm200863q.

[71] Masoumeh Tabatabee and S.Reyhaneh, Oriental Journal of Chem., 28 (2012) 243.

[72] L. Yang Pang, Xiaofeng Fox-Rabinovich, S.C. German Veldhuis and I. Zhitomirsky, Surf. Coat. Tech., 206(2011) 1-7; doi: 10. 1016 /j.surfcoat. 2011.06.029.

[73] B. S. Shirke A. A. Patil P. P. Hankare K. M. Garadkar,J. Mate. Sci., Materials in Electronics, 22(2)(2011)200–203.

[74] Tommy Mokkelbost, Ingeborg Kaus, Tor Grande and Mari-Ann Einarsrud, Chem. Mater.,16 (25)(2004) 5489–5494.

[75] N. Guillou, L. C. Nistor, H. Fuess, H. Hahn, Nanostruct.Mater., 8(5) (1997)545-557.

[76] Y. X. Li, W. F. Chen, and X .Z. Zhou, Mater. Lett., 59 (2005) 4.

[77] Hong Liu, Chenguo Hu and Zhong Lin Wang, Nano Lett., 6 (7) (2006) 1535–1540.

[78] Mahsa Zarinkamar, Majid Farahmandjou and Tahereh Pormirjafari Firoozabadi, J. Ceramic Processing Research 17(3)(2016)166-169

[79] Boby Samai, SoumenSarkar, SayantaniChall, Soumyadipta Rakshit and Subhash Chandra Bhattacharya, Cryst. Eng. Comm., 40(18) (2016) 7873-7882.

[80] V. Lair, A. Ringuedé, P. Vermaut, and S. Griveau, Phys. Status Solidi (c), 5(2008) 3492–3495.

[81] Y. Wang, T. Mori, J. G. Li, T. Ikegami, J. Am. Ceramic Soc.,85 (12) (2002)3105–3107.

[82] Siba Soren, Monalisa Bessoi, Purnendu Parhin, Ceramics Int., 41 (2015) 8114–8118.

[83] R. Dalia, Abd El-Hafiz, A. Mohamed, Ebiad and Lamia, S. Mohamed, Chemistry and Materials Research, 6 (12)(2014).

[84] J. C. Chen, W. C. Chen, Y .C. Tein and C. J. Shish, J Alloys Compd., 496 (2010) 364.

[85] L. Brian Cushing , L.V ladimi Kolesnichenko and J. Charles O'Connor, Chem. Rev., 104(9) (2004)3893–3946.

[86] S. Phokha, S. Pinitsoontorn, P. Chirawatkul, Y.Poo-arpornand S. Maensir, Nanoscale Res. Lett., 7 (2012) 425.

[87] L. Eyring, Synthesis of Lanthanide and Actinide Compounds, eds. G. Meyer and L. R. Morss, Springer Netherlands 2(1991)187-224.

[88] C. deLeitenburg, A. Trovarelli and J. Kaspar, J. Catal.,. 166 (1997)98-107

[89] S. Nakane, T. Tachi, M. Yoshinaka, K. Hirota and O. Yamaguchi, J. Am. Ceram. Soc.,80 (1997)3221-3224.

[90] N. Audebrand, J. P. Auffredic and D. Louer, Chem. Mater.,12 (2000)1791-179.

[91] X. D. Zhou, W. Huebner, H. U. Anderson, Appl. Phys. Lett., 80 (20) (2002) 3814–3816.

[92] E.Matijevic, W. P. Hsu, J. Colloid Interf. Sci., 118(2) (1987) 506-523.

[93] P. L. Chen, I. W. Chen , J. Am. Ceram. Soc., 76 (6) (1993) 1577–1583

[94] J.G. Li, T. Ikegami, Y.Y. Wang, T. Mori, J. Am. Ceram. Soc., 85 (9) (2002) 2376- 2378.

[95] N. Uekawa, M. Ueta, Y.J. Wu, K. Kakegawa, Chem. Lett., 8 (2002) 854-855.

[96] B. Djuricic and S. Pickering, J. Eur.Ceram.Soc., 19 (1999)1925-1934.

[97] H. L. Tuller, Solid State Ionics, 131(2000) 143-157.

[98] R. K. Hailstone, A. G. Di Francesco, J. G. Leong, T. D. Allston, K. J. Reed, J.phy.chem. C 113(34)(2009)15155-15159.

[99] A. Migani, G. N. Vayssilov, S. T. Bromley, F. Illas, K. M. Neyman, J. Mate.Chem., 20(2010)10535-10546.

[100] M. Kamruddin, P.K. Ajikumar, R. Nithya, A.K. Tyagi, Baldev Raj, Scripta Mater., 50 (2004) 417– 422.

[101] Sameer Deshpande, Swanand Patil, Satyanarayana, V.N.T. Kuchibhatla, and Sudipta Seal, Appl. Phys.Lett., 87(2005) 133113.

[102] Feng Zhang, Siu-WaiChan,a) Jonathan E. Spanier, Ebru Apak, Qiang Jin, Richard D. Robinson, and Irving P. Herman, Appl. Phys. Lett.,80(1)(2002)7.

[103] Bing Yan, Hongxia Zhu, J Nanopart Res.,10 (2008)1279-1285.

[104] Anwar Ali Baqera, Khamirul Amin Matoria, Naif Mohammed Al-Hada, Abdul HalimShaari, Elias Saion, Josephine Liew and Ying Chyi, Results in Physics, 7 (2017) 611–619.

[105] H. S.Kang, Y. C.Kang, H. Y. Koo, Mater. Sci.Eng., B127 (2006) 99–104.

[106] Y. X. Li, X. Z. Zhou, Y. Wang, X. Z. You, Mater. Lett., 58(2003)245–249.

[107] M. Hirano, E. Kato, J. Am. Ceram. Soc., 82 (1999) 786-788.

[108] M. Hirano, M. Inagaki, J. Mater. Chem., 10 (2000) 473-477.

[109] F. Zhang, S. P.Yang, H. M. Chen, X. B. Yu, Ceram.Int., 30 (2004) 997-1002.

[110] M. Zawadzki, J. Alloys Compd., 454(2008)347–351.

[111] T. Mokkelbost, I. Kaus, T. Grande, M. A. Einarsrud, Chem. Mater., 16 (2004) 5489–5494.

[112] R. C. R. Neto and M. Schmal, Appl. Catal. A 450 (2013) 131–142.

[113] Huey-Ing Chen, Hung-Yi Chang, Ceram. Int., 31 (2005) 795–802.

[114] M. G. Sujana, K. K. Chattopadyay, S. Anand, Appl. Surf. Sci., 254 (2008) 7405-7409.

[115] G. L. Tao, X. L. Lu, Z. H. Su, Y. Tao, H. P. Wu, Proceedings of Shanghai International Nanotechnology Cooperation Symposium, Nano micro letters (2011) 5-9.

[116] Zhiqiang Yang, Kebin Zhou, Xiangwen Liu, QunTian, Deyi Lu and Sen Yang, Nanotechnology, 18 (2007).

[117] ZhaoxiaJi, Xiang Wang, Haiyuan Zhang,Sijie Lin, HuanMeng, Bingbing Sun, Saji George, Tian Xia, André E. Nel, and Jeffrey I. Zink, ACS Nano. 6 (6) (2012) 5366-5380.

[118] Chunwen Sun, Hong Li, Huairuo Zhang, Zhaoxiang Wang and Liquan Chen, Nanotechnology, 16 (2005) 1454-1463.

[119] I. Kosacki, T. Suzuki, V. Petrovsky, H. U. Anderson, P. Colomban, Solid State Ionics, 149 (2002) 99–105.

[120] R. Zamiri, H. Abbastabar Ahangar, A. Kaushal Kuzyk, Plos One 10 (4) (2015) e0122989.

[121] Chun Zhao, Ce Zhou Zhao, Matthew Werner, Steve Taylor, Paul Chalker and Peter King, Nanoscale Research Letters, 8(2013)172.

[122] S. H. Lee, Z. Y. Lu, S.V. Babu, E. Matijevic, J. Mater. Res., 7 (2002) 2744.

[123] C. Laberty-Robert, J. W. Long, E. M. Lucas, K. A. Pettigrew, R. M. Stroud, M. S. Doescher, D. R. Rolison, Chem. Mater., 18 (2006) 50-58.

[124] A. Corma, P. Atienzar, H. García, and J.Y. Chane-Ching, Nature Materials, 3(6) (2004)394–397.

[125] A. Bensalem, J. C. Muller, and F. Bozon-Verduraz, J. Chem.Soc., Faraday Trans., 88(1)(1992) 153–154.

[126] Shin Tsunekawaa, Jian-Tao Wang ,Yoshiyuki Kawazoe, Atsuo Kasuya, J. Appl. Phys., 94(5) (2003) 3654.

[127] Tsan Liu, Min-Hsiung Hon, And Lay Gaik Teoh, J. Electron. Mater., 42(8) (2013)

[128] C.W. Sun, H. Li, H.R. Zhang, Z.X. Wang, L.Q. Chen, Nanotechnology 16 (2005) 1454–1463.

[129] Srivatsan Sathyamurthy, Keith J Leonard, Reza T Dabestani and M Parans Paranthaman, Nanotechnology 16(9) (2005).

[130] Bojana Andri , Nadica Abazovi, Radenka Krsmanovi, Miodrag Mitri, Amelia Montonea and D.D. Miroslav, Acta Chim. Slov.,55 (2008) 486-491.

[131] Anees A. Ansari , Journal of Semiconductors, 31(5) (2010).

[132] P.O. Maksimchuk, A. A. Masalov, V. V. Seminko, Yu. V. Malyukin, Proceedings of the International Conference Nanomaterials: Applications and Properties 1(4) (2012).

[133] N. V. Skorodumova, R. Ahuja, S. I. Simak, I. A. Abrikosov, B. Johansson, I. Lundqvist, Physical Review B (Condensed Matter and Materials Physics) 64(11) (2001).

[134] A. Tscho¨pe, Solid State Ionics, 139 (2001) 267–280.

[135] Takenori Yamamoto,Hiroyoshi Momida,Tomoyuki Hamada, Tsuyoshi da, Takahisa Ohno, Thin Solid Films, 486(1-2) (2005) 136-140.

[136] P. H. Cury Camargo, K. G. Satyanarayana, F. Wypych, Mat. Res.,12(1) (2009).

[137] A. A. Anees, M. A. M. Khan, K. M. Naziruddin, A. A. Salman, M.Alhoshan, and M. S. Alsalhi, J. Semiconductors,32(2011) 043001–043006.

[138] Adele Qi Wang and Teresa Diane Golden, Journal of Nanotechnology, 2016 (2016) Article ID 8459374 ; doi: 10.1155/ 2016/ 8459374.

[139] Arianfar M, Chem Sci J, 7(143) (2016) doi: 10.4172/2150-3494.1000143.

[140] Saranyoo Chaiwichian, Burapat Inceesungvorn, Kanlaya Pingmuang, Khatcharin Wetchakun, Sukon Phanichphant and Natda Wetchakun, Engineering Journal 16(3)(2012)

[141] M. C. Maria, K. Kaviyarasu , J. Judith Vijaya, B. Siddhardha and B. Jeyaraj, Photochem. Photobiol., B173 (2017) 23-34.

[142] K. S. Hemalatha and K. Rukmani , RSC Adv., 6 (2016) 74354-74366.

[143] Linhai Jiang, Mingguang Yao, Bo Liu, Quanjun Li, Ran Liu, Hang Lv, Shuangchen Lu, Chen Gong, Bo Zou, Tian Cui, Bingbing Liu, Guangzhi Hu, and Thomas Wågberg, J. Phys.Chem., C 116 (21) (2012) 11741-11745.

[144] N. Kobayashi, Bull. Chem. Soc. Jpn., 75(2002) 1–19.

[145] C. C. Leznoff and A. B. P. Lever, Phthalocyanines: Properties and Applications, Wiely, New York (1989).

[146] Pawan Kumar, Arvind Kumar, Chetan Joshi, Raghuvir Singh, Sandeep Saran and Suman L. Jain, RSC Adv., 5(2015) 42414.

[147] A. V. Krasheninnikov and K. Nordlund, J.Appl.Phys., 107(7) (2010) 071301.

[148] E. J. Yun, J. W. Jung, Y. H. Han, M.-W. Kim, and B. C. Lee, J Appl.Phys., 105 (12) (2009) 123509.

[149] P. A. Sheena, K. P. Priyanka, S. Aloysius, N., S. Ganesh, and V. Thomas, Bull. Mater.Sci., 38 (4) (2015) 825.

[150] A. Sreedevi, K. P. Priyanka, K. K. Babitha, S. Ganesh, and V. T, Micron 88(1) (2016).

[151] S. Raghu, K. Archana, C. Sharanappa, S. Ganesh and H. Devendrappa, J. Radiat. Res. Appl.Sci., 9 (2016) 0117-124.

[152] Pai S. Chethan, M. P. Joshi, S. Raj Mohan, T. S. Dhami, Jayakrishna Khatei, K. S. Koteshwar Rao, L. M. Kukreja, S.Ganesh , Adv. Mater. Lett., 4 (6) (2013) 454.

[153] M. Pattabi, B.S. Amma, K. Manzoor, S.Ganesh , Sol. Energy Mater. Sol. Cells,. 91 (2007) 1403.

[154] K. P. Priyanka, Joseph Sunny, Anu Tresa Sunny, O. P. Jaseentha, T. Varghese, Int. J.Emerg. Technol. Adv. Eng., 2 (2012) 11.

[155] K. P. Priyanka, N. Aloysius Sabu, Anu Tresa Sunny, P. A. Sheena, T. Varghese, J. Nanotechnol., (2013) 580308; http:// dx.doi.org/ 10.1155/ 2013/ 580308.

....

Chapter 2
EXPERIMENTAL TECHNIQUES

2.1 Introduction

Characterization of nanoparticle is mandatory to establish the understanding and control of synthesis, properties and applications. In order to take full advantage of synthesized nanoparticle, a clear analysis about its structural, compositional and functional properties is needed. In this chapter fundamentals and basic principles of characterization tools used in the present investigation are discussed. A list of the chemicals used for the synthesis of CeO_2 nanoparticles, CeO_2/CoPc and CeO_2/SnPc nanocomposites and a snapshot of the method of synthesis of these nanomaterials are also presented.

2.2 Materials

- Cerium(III) nitrate ($Ce(NO_3)_3.6H_2O$; 434.2 g/mole; 99.9% purity, Sigma Aldrich), ammonium carbonate ($NH_4\ HCO_3{\cdot}NH_2\ COONH_4$; 157.13 g/mole; 99.9% purity, Sigma Aldrich) and EDTA (Merck, 99.9% purity) are the chemicals used for the synthesis of cerium oxide nanoparticles.
- Cobalt phthalocyanine (Sigma Aldrich), dimethyl formamide (Merck), dimethyl sulphoxide (Merck) and ethanol (Merck) and

cerium oxide nanoparticles synthesized by chemical precipitation method are the materials used for the synthesis of cerium oxide/cobalt phthalocyanine nanocomposite.

- Tin phthalocyanine (Sigma Aldrich), dimethyl formamide (Merck), dimethyl sulphoxide (Merck) and ethanol (Merck) and cerium oxide nanoparticles synthesized by chemical precipitation method are the chemicals used for the synthesis of cerium oxide/tin phthalocyanine nanocomposite.

Distilled water is used in all the synthesis process.

2.3 Synthesis method

The investigation of new properties of nanostructures and their applications is possible only when materials are synthesized with suitable size, morphology and chemical composition [1]. Today, a wide variety of techniques are available for the production of nanoparticles. Solution based processing of nanomaterials is a very important synthesis route and has been used in many materials to achieve a variety of fabrication goals. Usually chemical methods can provide better control over the size, shape and functionalization of the nanomaterials synthesized [2].

Chemical precipitation

Precipitation technique of rare earth compounds from aqueous solutions using suitable reagents is useful for the production of metal oxide nanoparticles for various applications. Usually solutions of

different ions are mixed in well defined quantities and under controlled physical conditions such as temperature and pressure, to stimulate the formation of insoluble compounds, which precipitate out of solution. The precipitate is then collected through filtering. The obtained product is then dried to get powder sample. This reaction highly depends on the concentration of reactants, temperature, pH of the solutions and the order in which the reagents are added to the solution and mixing. This method is extremely useful for the synthesis of large variety of compounds. In the present study simple chemical precipitation method is employed for the synthesis of cerium oxide nanoparticles.

2.4 Characterization techniques

Most of the characterization techniques involve elementary particles like electrons or photons as a probe beam striking the sample material to be analyzed. This beam interacts with the sample and the changes induced in the beam (energy, intensity) are monitored after the interaction. Finally analytical information is derived from the observation of these changes. In this work, thermogravimetric (TGA) and differential thermal analysis (DTA) are the two different techniques used to analyze the thermal stability of the materials synthesized. The structural characterizations include X-ray diffraction (XRD), scanning electron microscopy (SEM) and transmission electron microscopy (TEM) techniques. Fourier transform infrared spectroscopy (FTIR) and

Raman spectroscopy are employed to identify the functional groups and to analyze the vibrational motion of atoms and molecules. Energy-dispersive X-ray spectroscopy (EDX) is used to examine the chemical composition of the sample. Optical characterization of the samples are performed using UV-visible absorption spectroscopy and photolumin escence spectroscopy (PL) .

2.4.1 Thermal characterization

In thermal analysis, a series of techniques are used for measuring the temperature dependence of a physical property of certain substances. In this work, thermogravimetric analysis and differential thermal analysis techniques are employed for this purpose.

Thermogravimetric analysis

Thermogravimetric analysis is a method of thermal analysis, which is used for studying the changes in the physical and chemical properties of a material by measuring weight change with increasing temperature under inert or reactive atmospheres. TGA will provide the information about the physical phenomena such as crystallization and phase transformation or chemical processes like decomposition, oxidation and reduction that occurred when temperature increases [3]. When a substance is subjected to continuous heating, the material will exhibit either mass loss or gain due to decomposition, oxidation, or loss of volatiles such as moisture. This change in weight of the sample is

measured as a function of temperature in TGA. The rate of change of weight with respect to temperature or time is recorded using derivative thermogravimetry (DTG).

Differential thermal analysis

In this thermo analytic technique, the sample material under study and an inert reference are made to undergo identical thermal cycles, while recording any temperature difference between sample and reference. In DTA, this differential temperature (exothermic or endothermic) is then plotted against time. A DTA curve provides the information about glass transitions, crystallization, melting and sublimation. The area under a DTA peak is the enthalpy change and is not affected by the heat capacity of the sample. DTA is used for the analysis of phase diagrams, heat change measurements and decomposition in various atmospheres.

In the present work, the thermal behavior of the synthesized CeO_2 nanoparticles, electron beam irradiated CeO_2 nanoparticles and CeO_2 based phthalocyanine composites are analyzed by thermogravimetric analyzer and differential thermal analyzer using *Perkin Elmer STA 6000*.

2.4.2 Structural characterization

2.4.2.1 Powder X-ray diffraction

X-ray diffractometry is a non-destructive quantitative technique to investigate the crystal structure of solids. Information related to phase composition, grain size, internal lattice strain, preferred crystal orientation, lattice constant, unit cell and degree of crystallinity of the material can be determined from XRD results. It is based on the constructive interference of monochromatic X-rays. A narrow beam of X-rays, with a wavelength ranging from 0.07 to 0.2 nm, is diffracted by the crystalline phases of the specimen according to Bragg's law [4] :

$$n\lambda = 2d \sin\theta \ (n=1,2,3\ldots), \qquad \textbf{(2.1)}$$

where d is the interplanar distance and λ the wavelength of the X-rays. The intensity of the diffracted beam is measured as a function of the diffraction angle (2θ) and the specimen's orientation. Structural properties of the specimen can be studied from the diffraction pattern. The quantitative identification can be determined by comparing the XRD pattern of the unknown material with standard data files of the *Joint Committee on Powder Diffraction Standards (JCPDS)*.The mean grain size (D) of the crystallite is determined by using Scherrer equation [5],

$$D = K\lambda / (\beta\cos\theta), \qquad \textbf{(2.2)}$$

where K is the Scherrer's shape factor (0.9), β the full width at half maximum of the peak at 2θ value and λ the X-ray wavelength (1.5406 Å). The lattice constants 'a' is calculated from the lattice spacing of (111) peaks of cerium oxide nanoparticles in accordance with the Bragg equation. For cubic crystal structure, $a=b=c$ and

$$1/d^2_{hkl} = (h^2+k^2+l^2)/a^2, \qquad \textbf{(2.3)}$$

where d_{hkl} is the spacing between the planes corresponding to Miller indices (hkl) and a is lattice constant.

The length of dislocation lines per unit volume of the crystal is called as the dislocation density and the term dislocation indicates a crystallographic defect or irregularity within the crystal structure. Homogeneous nucleation and grain boundary initiation are the two main mechanisms for dislocation. A larger dislocation density implies more hardness [6]. Dislocation density (δ) is calculated from particle size by using the formula,

$$\delta = 1/D^2. \qquad \textbf{(2.4)}$$

Williamsons –Hall (W-H) method

The strain induced in nanopowders due to crystal imperfection and distortion is calculated using the formula,

$$\sigma = \beta/4\tan\theta \qquad \textbf{(2.5)}$$

From equations **(2.2)** and **(2.3)**, it is noticed that the peak width varies *1/cosθ* changes, and strain varies with *tanθ*. Assuming that the particle size and strain contributions to line broadening are independent of each other and both have a Cauchy-like profile, the observed line breadth is simply the sum of equation **(2.2)** and **(2.5)** [7]

$$\beta = K\lambda/D\cos\theta + 4\sigma \tan\theta \qquad \textbf{(2.6)}$$

By rearranging Eq. **(2.6)**,

$$\beta \cos\theta = K\lambda/D + 4\sigma \sin\theta \qquad \textbf{(2.7)}$$

The equations **(2.6)** and **(2.7)** are W-H equations. The micro strain induced in the nanomaterial can be calculated from W-H plot, which is drawn with *4 sinθ* along the x-axis and *β cosθ* along the y-axis . From the linear fit to the data, the crystallite size is estimated from the y-intercept, and the strain σ from the slope of the fit.

In this research work, XRD analysis is carried out in reflection mode by X-ray powder diffraction method, using *Bruker D8 Advance X-ray diffractometer* with Cu-Kα radiation (λ=1.5406 Å, X-ray tube voltage = 40 kV and current = 35 mA). The scan is taken in the 2θ range from 0-70^{o} with step size of 0.02^{o}. Fig.2.1 shows the photograph of a *Bruker D8 Advance X-ray diffractometer.*

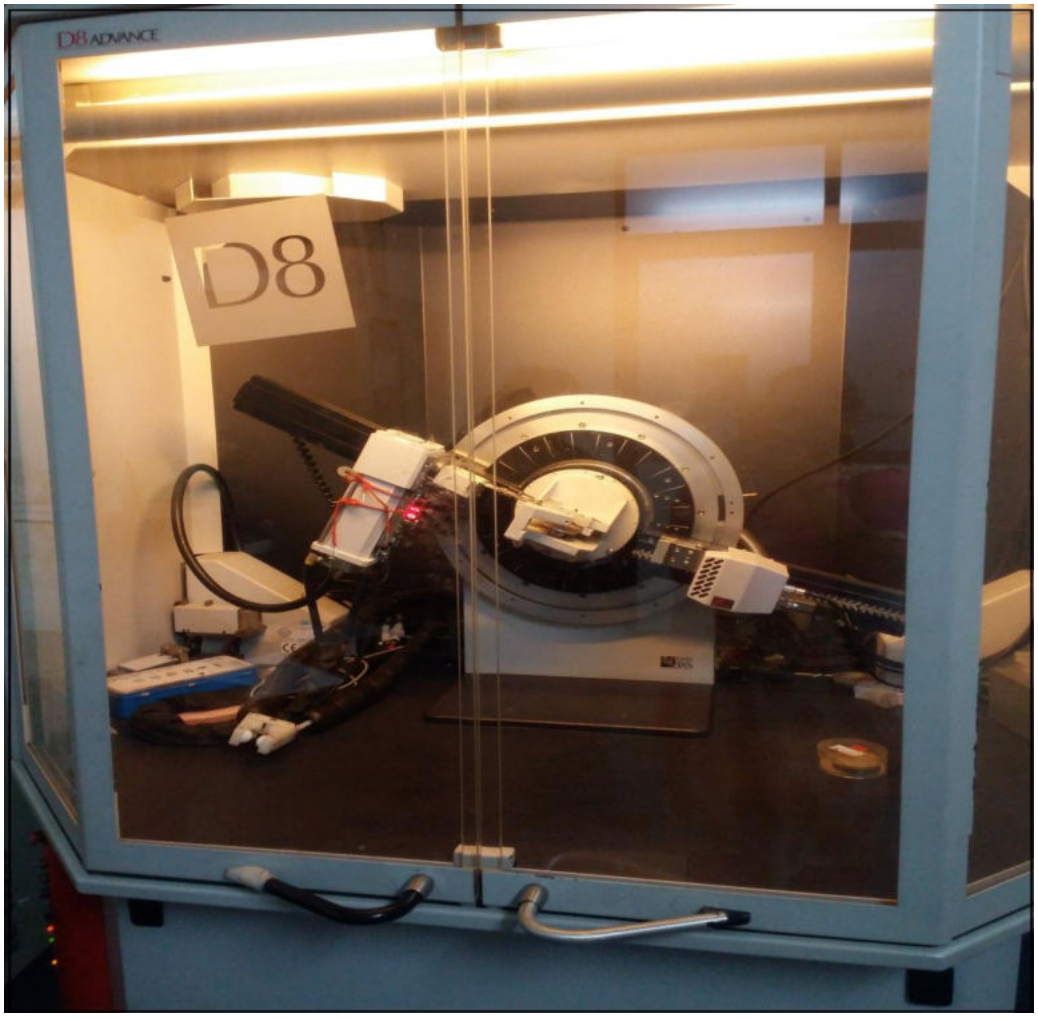

Fig.2.1 Photograph of Bruker D8 Advance X-ray diffractometer

2.4.2.2 Transmission electron microscopy

In a transmission electron microscope a beam of electrons is used in the place of ordinary light and focusing is done by electric and magnetic fields. It can provide structural, phase and crystallographic data of materials down to atomic levels with high spatial resolution. This high spatial resolution of TEM is due to the small de Broglie wavelength of electrons ($\lambda = h/mv$) [8]. In this imaging technique, a beam of electrons

is generated from an electron gun by thermionic discharge and is focused onto a specimen. The electromagnetic lenses and electrostatic plates in the instrument guide the electron beam as required. The transmitted electrons through the specimen can be used to develop images. The enlarged version of this image is detected using a photographic film, or fluorescent screen or CCD camera.

In TEM, one can collect images either by TEM image observation mode (magnified image of a magnified specimen) or selected area electron diffraction (SAED) method. SAED patterns can be used to find whether the sample is amoprohous (diffuse rings) or crystalline (bright spots) or polynanocrystalline (small spots making up rings, each spot arising from Bragg reflection from an individual crystallite). Dark Field (DF) images are ready to provide the information about planar defects, stacking faults or particle size, in which the direct beam is blocked by the aperture while one or more diffracted beams are allowed to pass. In the bright field (BF) mode, all the beams except direct beam are blocked. In this case, the image results from a weakening of the direct beam by its interaction with the sample. In the case of lattice images, image is formed by the interference of the diffracted beams with the direct beam. High resolution TEM (HRTEM) images are used to investigate the atomic structure of a specimen directly.

Fig.2.2 JEOL model JEM-2100 transmission electron microscope

For TEM studies, the powder samples are dispersed in ethanol using an ultrasonic bath. A drop of the suspension is placed on a copper grid coated with carbon film. After drying, the copper grid containing nanoparticles is placed on a holder for the imaging process. TEM images of all samples are taken on a *JEOL model JEM-2100* electron microscope

operated at 200 kV with a resolution of 0.23 nm and analysis of the results is done by *Image J* software. Fig.2.2 shows the photograph of JEOL model JEM-2100 transmission electron microscope.

2.4.2.3 Scanning electron microscopy

The scanning electron microscope is used to study the surface morphology of solid specimens by a focused beam of high energy electrons. Due to the manner in which the image is created, SEM images have a characteristic three-dimensional appearance and are useful for judging the surface of the sample. In SEM, high energy electrons from an electron gun are made to incident on a sample surface. When these electrons interact with the sample, KE of the electrons are dissipated and secondary electrons, backscattered electrons, diffracted backscattered electrons, photons and heat are produced. Secondary electrons are most valuable for showing morphology and topography of samples and backscattered electrons are responsible for crystal structure and orientation of materials. The combination of higher magnification, larger depth of focus, greater resolution and ease of sample observation makes the SEM one of the most heavily used techniques in research areas today.

In the present study, the surface morphology of samples is analyzed with a scanning electron microscope *JEOL model JSM-6390LV*, operating at 20 kV and having a resolution of 3 nm. Fig.2.3 shows the photograph of JSM-6390LV scanning electron microscope.

Fig.2.3 JEOL model JSM-6390LV scanning electron microscope

2.4.2.4 Energy dispersive X-ray spectroscopy

Qualitative elemental analysis, standard less quantitative analysis, X-ray line scans and mapping can be performed with SEM-EDX combination. Energy dispersive X-ray spectroscopy is used to analyze

the chemical composition of a specimen by the interaction of some source of X-ray excitation and a sample. A small change in composition of elements may cause high variations in the electrical and optical properties of nanoparticles. Its characterization capability is mainly related to the fundamental principle that every element has its own atomic structure allowing X-rays that are characteristic of an element's atomic structure. Ionization of an atom by high energy charged particle may cause X-ray emission, and an electron-hole pair is produced within the atom. During de-excitation, an electron from a higher energy outer shell fills the vacant inner shell, and an amount of energy equal to the energy difference between the two shells is released. This excess energy will be emitted in the form of a photon or as an auger electron. In this study, a *JEOL model JED – 2300 and BRUKER X Flash 6/10EDS* detectors are used to record EDX spectrum of the synthesized nanosamples.

2.4.2.5 Fourier transform infrared spectroscopy

FTIR spectroscopy is employed to identify the functional groups and to analyze the vibrational motion of atoms and molecules [9]. Absorption of IR radiation can results in vibrational transitions of molecules. In FTIR spectroscopy, when IR radiation incident on a sample, each molecule in the sample absorbs only IR light of certain frequencies based on the characteristic for each molecule. Hence, it is

possible to identify the molecule type (qualitative analysis) and the amount of molecule in the sample (quantitative analysis) by studying the absorption spectrum.

Source, interferometer and detector are the main parts of FTIR spectrometer. IR beam from the source are directed towards the Michelson interferometer present in the FTIR system. The beam splitter in the interferometer splits the incident beam into reflected and transmitted beams. Either reflected or transmitted beam is passed through the sample and collected by the detector. The sample absorbs certain frequency of radiation based on the characteristics of each molecule present in the sample. In Fourier transform, time domain is converted in to frequency spectrum and intensity is plotted as a function of frequency in the IR spectrum. From the characteristic peaks, different functional groups present in the compound can be identified [10].

In this study, Fourier transform infrared spectrum of the nanoparticles are recorded by FTIR spectrophotometer (*Thermo Nicolet, Avatar 370*) in the range 2000 to 400 cm^{-1}. The spectral output are recorded by transmittance (*%T*) as a function of wave number ($1/\lambda$) cm^{-1}.

2.4.2.6 Raman spectroscopy

Raman spectroscopy is an analytical tool for molecular finger printing as well as monitoring changes in molecular bond structure. It

can be employed to estimate the vibrational, rotational and other low-frequency modes in a system. A beam of monochromatic light from a laser source interacts with the sample and emits light during de-excitation process. As a result, energy of the laser photons being shifted up or down (Raman effect) depending upon the vibrational state of the molecule under study. The study of change in frequencies gives the information about the transitions in molecules of solid, liquid or gaseous samples [10]. Raman spectra are collected at room temperature using *Bruker FRA/106/S Raman spectrometer* with a scan range of 50-4000 cm^{-1} and having a resolution of 2 cm^{-1}. The laser source used is Nd: YAG with an output wavelength of 1064 nm.

2.4.3 Optical characterization

2.4.3.1 Ultraviolet-visible spectroscopy

Ultraviolet-visible spectroscopic technique is useful to characterize the absorption, transmission and reflectivity of materials [11]. The incident UV or visible rays excites outer electrons in the test sample to a higher energy level and the degree of absorption is characteristic of the material under illumination. This transition from highest occupied molecular orbit in the valence band (HOMO) to lowest unoccupied molecular orbital in the conduction band (LUMO) is possible only when the incident photon energy is equal or greater than the energy difference between a possible electronic transition. As a result, there is a

sharp increase in absorption at energy close to band gap that manifests itself as an absorption edge (or reflection threshold) in the UV-visible absorption spectrum [12, 13]. This technique is very useful to find the band gap energy of semiconducting materials.

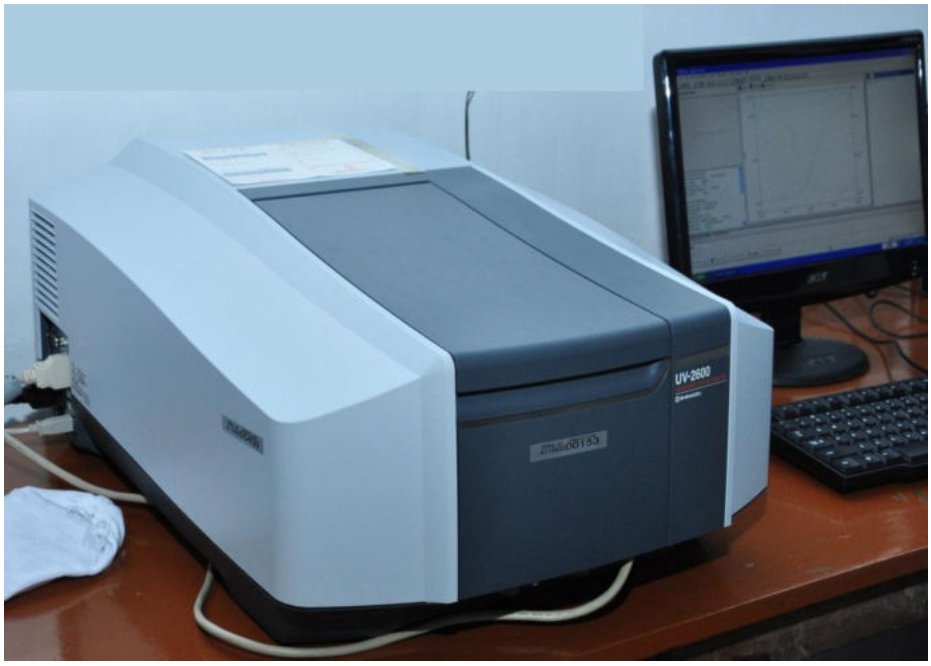

Fig.2.4 Shimadzu UV-2600 model UV-Visible spectrophotometer

The basic components of a spectrophotometer are a light source, a sample holder, a diffraction grating in a monochromator to separate the different wavelengths of light, detector and a recorder. The ultraviolet or visible light is split into two beams before it reaches the sample. One beam is used as the reference and the other beam passes through the sample (liquid) which is taken in a cuvette. By base line correction, the reference beam intensity is taken as 100% transmission. A complete absorption spectrum at all wavelengths can be produced and

identification is done by comparing this absorption spectra with the spectra of reference material. The amount of absorption is recorded by a plot of absorbance (A) versus wavelength (λ). A shift in the absorption edge of the sample depends upon the variation in particle size . The shifting of absorption edge to shorter wavelength is known as blue shift (Hypsochromic shift) and shift towards higher wavelength is termed as red shift (Bathochromic shift)

Band gap energy

Band gap energy is determined from the Tauc relation [14],

$$(\alpha hv)=A(hv—E_g)^n, \qquad \textbf{(2.8)}$$

where E_1 is the band gap, v the frequency, A is a constant and n can have values *1/2, 3/2, 2* and *3* depending upon the mode of inter band transition i.e. direct allowed, direct forbidden, indirect allowed and indirect forbidden transition, respectively. The direct optical band gap *Eg* is estimated from the plot $(hv\alpha)^2$ *vs.* (hv) by extrapolating the curve to absorption equal to zero (Tauc plot).

In the present research work, the absorption spectra of the samples are collected by Kubelka Monk transformation method [15] using a double beam UV-Visible spectrophotometer (*Shimadzu UV-2600 model).* For the measurement, powder samples are pressed into a thick pellet and placed at the entrance port of integrating sphere using a sample holder.

Calibration of the absorbance scale is done using barium sulphide. Fig. 2.4 represents the photograph of *Shimadzu UV-2600 model* UV-Visible spectrophotometer.

2.4.3.2 Photoluminescence spectroscopy

Photoluminescence spectroscopy is used for the characterization of optical and electronic properties of semiconductors and molecules by analyzing the optical emission spectra of these materials. The incident light promotes the transition of electrons from the ground state to excited levels, producing electron-hole pairs. During recombination extra energy is released as photons and this emitted light is termed as luminescence. The intensity of emitted radiation as a function of either the excitation wavelength or the emission wavelength is plotted in the PL spectrum. The excitation spectrum can provide the best excitation wavelength for a quantitative or qualitative analysis.

Initially one can select the exact wavelength of excitation for a particular sample. Sample molecules are exposed to this wavelength from the source. After completing the life time in the excited state, molecule undergoes de-excitation. Detector detects the emitted photons in terms of its wavelength. The intensity and time dependence of the light emission are related to the possibility of electronic transition within the sample and it is used for qualitative and sometimes, quantitative analysis such as chemical composition, structure,

impurities, kinetic process and energy transfer. The wavelength versus intensity of the emission spectra will be displayed on the screen. The energy of the emitted photon,

$$E = h\nu = hc/\lambda \ \ in\ eV \qquad \textbf{(2.9)}$$

In the present study, photoluminescence spectra of the samples are measured at room temperature using a *Fluoromax-3 spectrophotometer* having a 20-kW continuous powered high-pressure Xe lamp as the excitation source and an R928 photomultiplier as the photo-detector. Fig. 2.5 shows the photograph of a *Fluoromax-3 spectrophotometer.* The emission spectra are recorded in the range 350–650 nm at an excitation wavelength of 330 nm using an excitation slit width of 5 nm.

Fig.2.5 Fluoromax-3 spectrophotometer

CIE chromaticity diagram

The international commission on illumination (Commission Internationale de l'Eclairage -CIE) is an internationally accepted standard for quantifying visible colours. Fig.2.6 shows 1931 CIE chromaticity diagram.Visible luminescence spectrum from the sample are measured and expressed by the resultant chromaticity coordinates *(x, y)* on a two dimensional plane. The light in the range of 380 to 780 nm are distinguished by human visual system (HVS) and spectral power density (SPD). Any of the visible colour is represented as a combination of three primary colours. These are denoted by tristimulus values *(X,Y,Z).* These values are determined by integrating the product of the light source $P(\lambda)$ and the CIE colour matching functions $x(\lambda)$, $y(\lambda)$ and $z(\lambda)$ over the entire visible range.

$$\left.\begin{aligned} X &= \sum x(\lambda)\, P(\lambda)\, \Delta\lambda \\ Y &= \sum y(\lambda)\, P(\lambda)\, \Delta\lambda \\ Z &= \sum z(\lambda)\, P(\lambda)\, \Delta\lambda, \end{aligned}\right\} \qquad \textbf{(2.10)}$$

where $\Delta\lambda$ is the interval between the points. These tristimulus values are used to calculating the CIE coordinates by the equation

$$\left.\begin{aligned} x &= X/X+Y+Z \\ y &= Y/X+Y+Z \\ z &= Z/X+Y+Z \end{aligned}\right\} \qquad \textbf{(2.11)}$$

The position of the colours in CIE diagram is obtained by plotting only *x* and *y* values since $x+y+z = 1$.

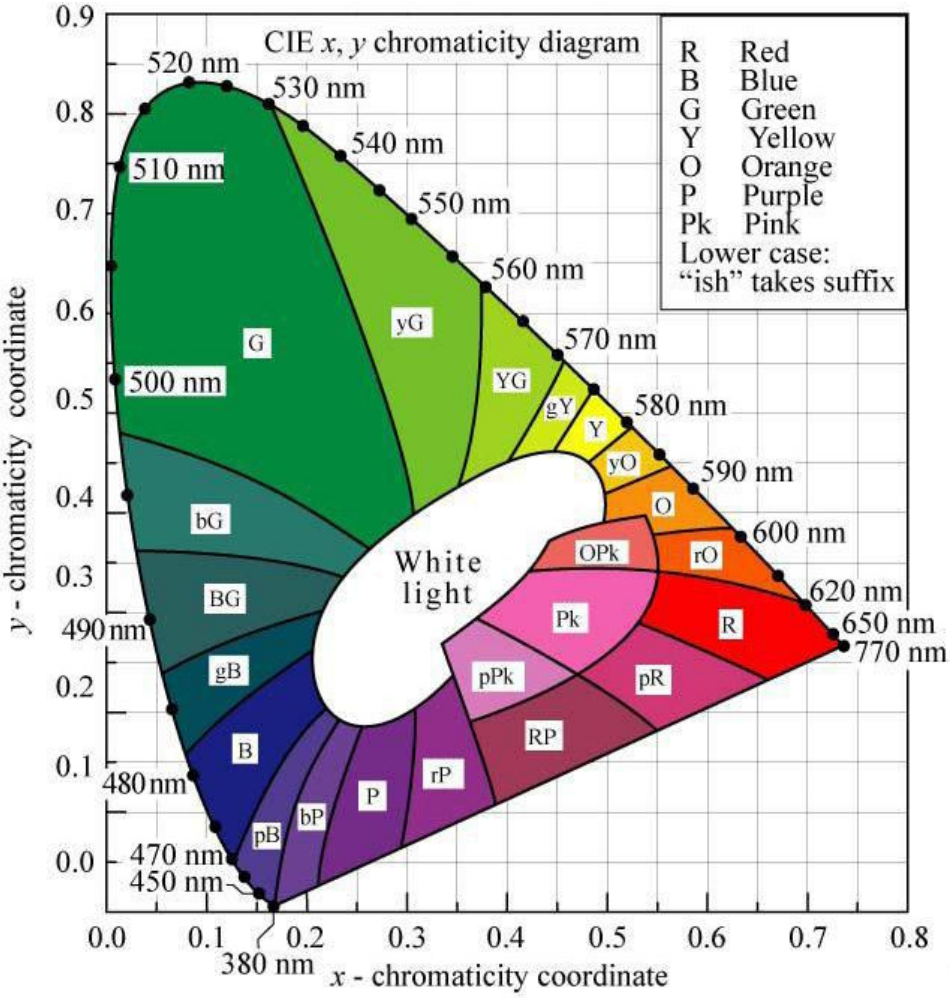

Fig. 2.6 1931 CIE chromaticity diagram [16]

2.4.4 Electrical characterization

Electrical impedance analysis is a powerful technique for identifying and characterizing the charge transport phenomenon in various materials. AC measurements yield information which can be used to determine whether the intrinsic conduction process can be

described by hopping model or band theory, under particular operating conditions [17]. The principle of parallel plate capacitor is employed for the evaluation of permittivity. For dielectric studies, the powder sample is consolidated in the form of cylindrical pellets using a hydraulic press. Both the faces of the pellets are coated with air drying silver paste for good electrical contact. The system will act as a metal-insulator-metal capacitor.

The experiments are carried out using a cell assembly for holding the sample and an impedance analyzer. The capacitance *C* and loss factor *(Tanδ)* can be measured as a function of frequency at selected temperatures. The dielectric parameters and AC conductivity can be calculated from the capacitance value by the equation,

$$C=A\,\varepsilon_0\varepsilon'/d, \qquad \textbf{(2.12)}$$

where *A* the face area, ε_0 the permittivity of vacuum, ε' the dielectric permittivity of the given sample and *C* the measured capacitance of the pellet. The complex dielectric permittivity is represented by $\varepsilon^*=\varepsilon'-i\varepsilon''$, where ε' is the real part of the dielectric permittivity that describes the stored energy, while ε'' is the imaginary part of the dielectric permittivity related to the dissipation energy (or loss of energy) within the medium [18]. The dielectric constant of the sample is determined by using the expression

$$\varepsilon' = Cd/A\varepsilon_0 \qquad \textbf{(2.13)}$$

Any capacitor when charged under a voltage will have some loss current due to ohmic resistance or impedance by heat diffusion. The dielectric loss is a measure of energy loss in the dielectric during AC operation, which is a material property and does not depend on the geometry of capacitor [19].

The dissipation factor (loss tangent),

$$Tan\delta = \varepsilon'' / \varepsilon' \qquad \textbf{(2.14)}$$

The loss tangent (*Tanδ)* is directly obtained from the experiment. The AC conductivity (σ_{ac}) is obtained from the dielectric constant *(ε′)* and tangent loss (*Tanδ)* using the relation,

$$\sigma_{ac} = \varepsilon' \varepsilon_0 \omega \, Tan\delta, \qquad \textbf{(2.15)}$$

where ε_0 is the permittivity of free space and ω the angular frequency *($\omega = 2\pi f$).*

Conductivity is an increasing function of frequency in the case of hopping conduction. While in a band conduction, it is a decreasing function of frequency. Then the total conductivity is considered as the sum of both hopping and band conduction.

In the present study, the powder samples are consolidated in the form of cylindrical pellet of diameter 13 mm at a pressure of ~7 GPa using a hydraulic press. The pellet prepared is then sintered at 150^{o}C for

2 h. Both the faces of the pellets are coated with air drying silver paste for good electrical contact. Dielectric measurements as a function of frequency in the range of 100 Hz−10 MHz are measured at various temperatures (303- 423 K) using *Wayne Kerr H-6500B* model impedance analyzer (Fig. 2.7) in conjunction with a portable furnace and a temperature controller (±1 K). The standard measurement accuracies for capacitance and loss tangent values are ± 0.05% and ± 0.0005% respectively. Capacitance (C) and loss factor (*Tanδ*) are directly collected from the experimental data. The temperature, frequency and compositional dependence of dielectric constant, loss tangent and AC conductivity are measured for all the samples.

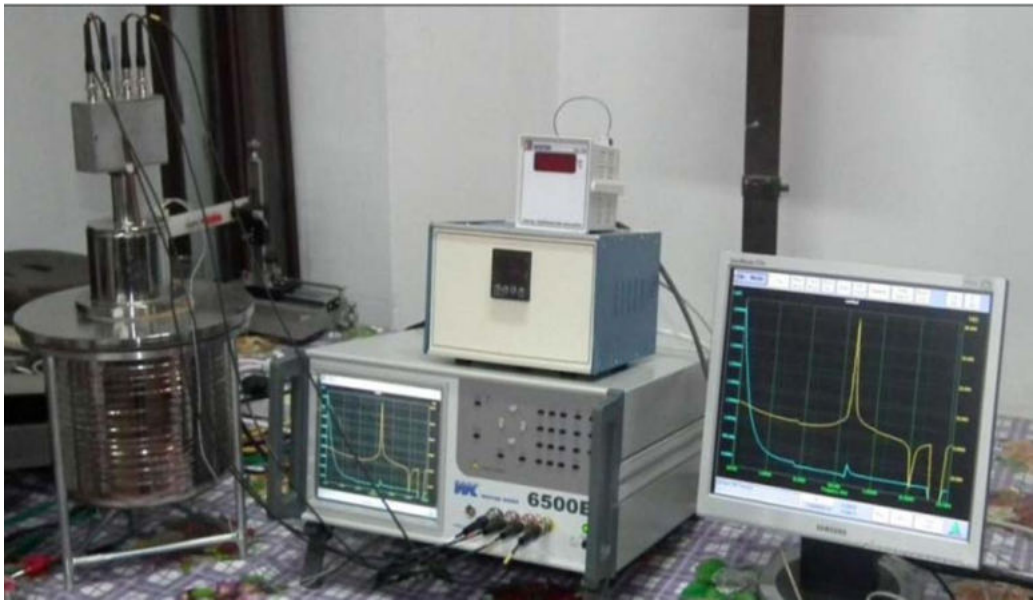

Fig 2.7 Wayne Kerr Impedance Analyzer (6500B)

Power Law

The total conductivity of the material can be considered as the sum of both AC and DC conductivities represented by the equation [20],

$$\sigma_{total} = \sigma(T) + \sigma(\omega, T) \quad \textbf{(2.16)}$$

The term $\sigma(T)$ is due to the band conduction, and is frequency independent which can be considered as the electronic or DC conductivity. The second term $\sigma(\omega, T)$ is due to the hopping process, and is frequency dependent, which can be considered as the AC conductivity [21]. The frequency dependence of AC conductivity can be expressed by empirical power law as described by Jonscher and referred to as universal dynamic response [20, 22]

According to Jonscher's universal power law,

$$\sigma(\omega, T) = \sigma_{AC} = A\,\omega^{S}, \quad \textbf{(2.17)}$$

where $\omega = 2\pi f$ is the angular frequency, A is a pre-exponential constant and S is the frequency exponent. The frequency exponent S $(0 \leq S \leq 1)$ characterizes the low frequency region, corresponding to translational ion hopping. The value of S can be determined by best fitting ($log\ \sigma_{ac}$) versus ($log\ \omega$) lines using the least squares method.

2.5 Electron beam irradiation

The Microtron facility at Mangalore University, Karnataka, India has been used for the electron beam irradiation of CeO_2 samples (Fig. 2.8). In a microtron accelerator, the electrons revolve in a uniform magnetic field and accelerate each time they pass through the electric field of the accelerator cavity. Once the accelerated electrons reach a predefined energy level, they are expelled as a beam via an exit pipe to an external device.

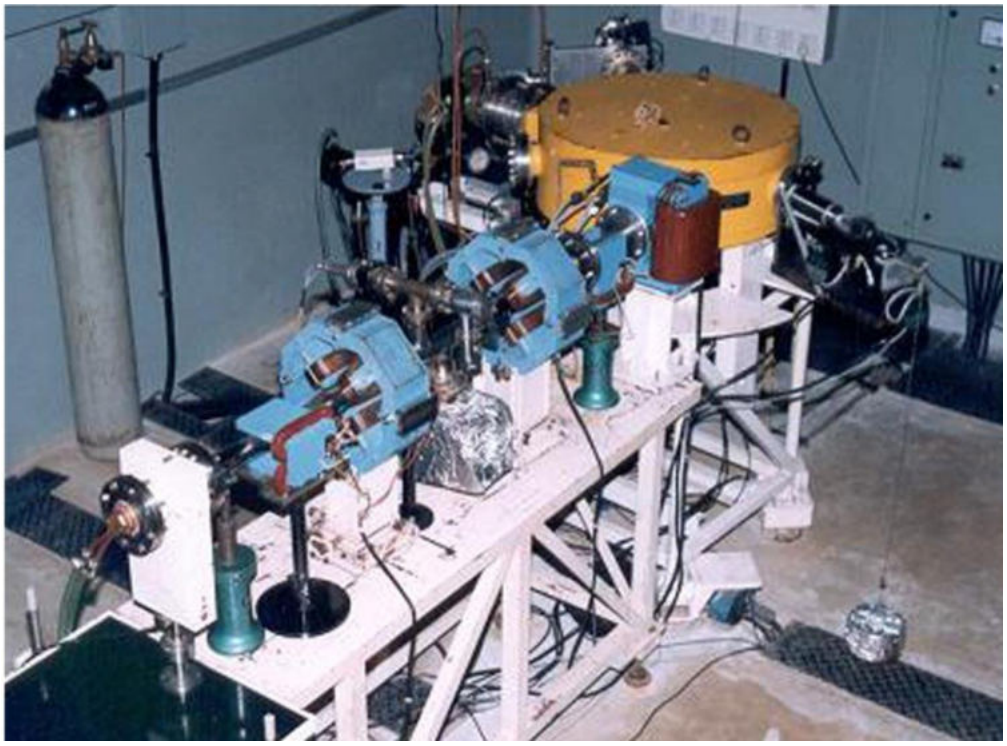

Fig 2.8 Microtron facility at Mangalore University

The synthesized powder samples are taken in polythene bags for irradiation. Samples are exposed to 8 MeV electron beam at a distance of 30 cm from the beam exit port. The doses absorbed by the samples are evaluated by glutamine dosimetry using a *Secomam-Anthelie-70MI0291 UV– visible spectro photometer* [23]. A standard ^{60}Co gamma chamber is used for the calibration of doses. In this research work, nanoceria samples are irradiated at a dose of 5 and 10 kGy with a pulse current of 50 mA and a pulse rate of 50 Hz.

References

[1] T. Varghese, K.M. Balakrishna, Nanotechnology: An Introduction to Synthesis, Properties and Applications of Nanomaterials, Atlantic Pub., 2012, pp. 1-212.

[2] C. N. R. Rao, S. R. C. Vivekchand, K. Biswas, A. Govindaraj, Dalton Trans., 34 (2007) 3728- 3749.

[3] A.W. Coats, J. P. Redfern, Analyst 88 (1053) (1963) 906-924.

[4] Charles Kittel, Introduction to Solid State Physics, John Wiley and Sons,New York 1997.

[5] B. D. Cullity, Elements of X-Ray Diffraction. Addison-Wesley, MA,1967.

[6] S. W. Chen, J. M. Lee, K. T. Lu, C. W. Pao, J. F. Lee, T. S. Chan, J. M. Chen, Appl. Phys. Lett., 97 (2010) 012-104..

[7] G. K. Williamson, W. H. Hall, Acta.Metall. 1 (1953)22

[8] D. Williams, C. B. Carter, Transmission Electron Microscopy, Plenum Press, 1996.

[9] S. Ankita, P. S. Bhanu, K. G. Arvind, Indian J. Pure and Appl. Phys. 52 (2014) 93.

[10] R. H. Atalla, U. P. Agarwal, Science 227 (1985) 636-38.

[11] C. N. R. Rao, Ultraviolet-visible Spectroscopy, 2nd Edition, Butter worth Co Publi., London, 1967.

[12] S. H. Mohamed, M. El-Hagary, A. S. Radwan, Indian J. Phys., 87 (2013) 223.

[13] N. Venkatachalam, M. Palanichamy, V. Murugesan, Mater. Chem. Phys., 104 (2007) 457.

[14] J. Tauc, A. Menth, Non Cryst. Solids., 8 (1972) 569-585.

[15] H. S. Kim, C .R. Lee, J. H. Im, K. B. Lee, T. Moehl, A. Marchioro, S. J.Moon, R. Humphry-Baker, J. H. Yum, J. E. Moser, M. Grätzel, and N.G. Park, Scientific reports 2 (2012) 591.

[16] S. Gage, D. Evans, M. W. Hodapp, H. Sorensen, Optoelectronics Applications Manual, McGraw Hill, New York, 1977.

[17] N. M. Khusayfan, Australian Journal of Basic and Applied Sciences 5 (11) (2011) 1290-1295.

[18] A. M. M. Farea, S. Kumar, K. M. Batoo, A. Yousef, and C. G. Lee, J. Alloys Compd. 464 (2008) 361.

[19] K. K. Babitha, K. P. Priyanka, H. Hitha, S. Rintu Mary, E. M. Mohammed, S. Sankararaman, Thomas Varghese, Journal of Electronic Materials (2017); doi: 10.1007/s11664-017-5653-z.

[20] A. K. Jonscher, Nature 267 (1977) 673.

[21] M. A. El Hiti, J. Phys. D: Appl. Phys., 29 (1996) 501-505.

[22] A. K. Joncher, Thin Films., 11 (1980) 232.

[23] V. Jain, Gupta B L, Appl. Radiat. Isot., 45 (1994) 973.

Chapter- 3
THERMAL, STRUCTURAL, OPTICAL AND ELECTRICAL PROPERTIES OF CERIUM OXIDE NANOPARTICLES

3.1 Introduction

The ability to tailor the properties so as to optimize the performance requires a detailed understanding of the relationship between structural, optical and electrical properties particularly at nanoscale dimensions [1].In this chapter, synthesis and characterization of cerium oxide nanoparticles are presented. Cerium oxide nanoparticles are synthesized by simple cost effective chemical precipitation method. Studies based on the structural features, optical and electrical properties of synthesized nanoceria along with the effect of calcination temperature on these properties are also presented in this chapter.

3.2 Synthesis of cerium oxide nanoparticles

Cerium oxide nanoparticles are prepared by reacting aqueous solutions of Cerium(III) nitrate and ammonium carbonate (0.1 M each) at room temperature. Stoichiometrically prepared EDTA solution is added drop by drop to the solution of cerium nitrate to control the size of

nanoparticles and avert the reverse reaction. This mixture solution is then added slowly into ammonium carbonate solution. The whole mixture is then stirred for 2 h using magnetic stirrer. The final product is a pale yellow precipitate, which is filtered and washed with distilled water several times. The product is then heated at 60°C for 24 h to form powder samples. The powder samples are calcined at 400, 550, 700 and 850°C for 3 h in a porcelain crucible using a muffle furnace in an ambient atmosphere. CeO_2 samples calcined at 400, 550, 700 and 850°C are designated as S1, S2, S3 and S4, respectively. The scheme of synthesis process can be explained by the flow chart which is depicted in Fig.3.1.

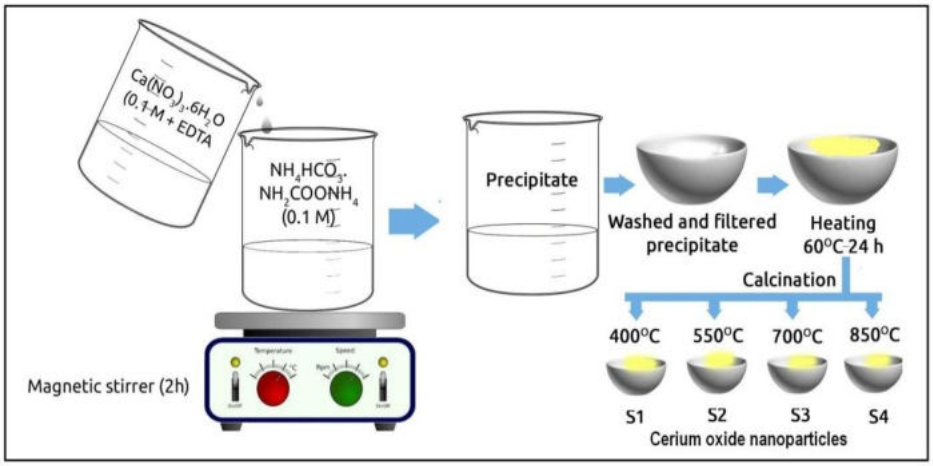

Fig.3.1 Scheme of preparation of cerium oxide nanoparticles

3.3 Results and discussion

3.3.1 Thermal analysis

The choice of suitable calcination temperature depends on the results of TG analysis. Fig.3.2 represents the thermogravimetric and

differential thermal analysis curves of the prepared CeO_2 nanoparticles collected by Perkin Elmer STA 6000. TGA curve shows a continuous weight loss up to 350°C. In this, the weight loss from 40 to 200°C is attributed to the loss of moisture and trapped solvents. The remaining weight loss in the range 200-350°C is due to the combustion of organic residues. The DTG curve shows a strong peak at243°C (weight loss ~4.75 mg/min) correlated to a weight loss confirming the combustion of organic residues due to the crystallization of residual amorphous phase. A strong exothermic peak at 249°C is found in the DTA curve. The thermal analysis shows that the synthesized nanoparticles are thermally stable in the range 200–850°C. As the weight remains constant after 400°C, this temperature was chosen to ensure the complete decomposition of the precursor to form cerium oxide nanoparticles.

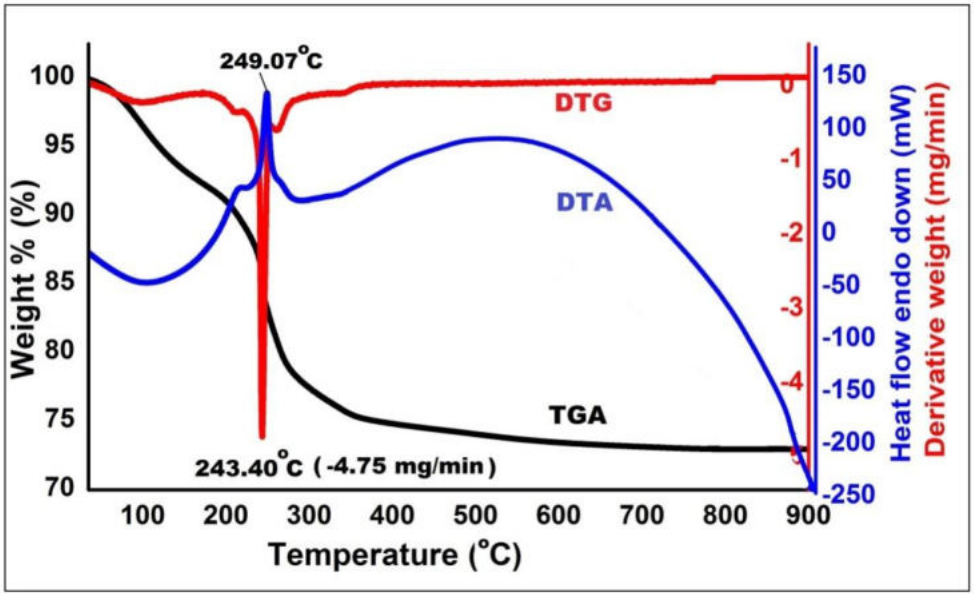

Fig 3.2 TGA/DTA/DTG curves of CeO_2 nanoparticles

3.3.2 Structural characterization

The structural analyses of the synthesized nanoceria samples are carried out by following the procedure described in *Section 2.4.2.*

3.3.2.1 Powder XRD analysis

The crystalline material structure, including atomic arrangement, crystallite size, and imperfections of the samples are examined using XRD. Fig.3.3 shows the XRD patterns of cerium oxide nanoparticles calcined at different temperatures which are collected by reflection mode with Cu-K_α radiation (λ= 1.5406 Å) using Bruker D8 Advance X-ray diffractometer (step size = 0.020^o, step time = 32.8 s and 40 kV, 35mA). The XRD spectra reveal that particles formed are crystalline. All peaks could be indexed to a pure cubic fluorite structure of CeO_2 (space group: *Fm3m*) with lattice constant *a*=5.411 Å, which is in agreement with the JCPDS file No. 75-0076 for CeO_2 .

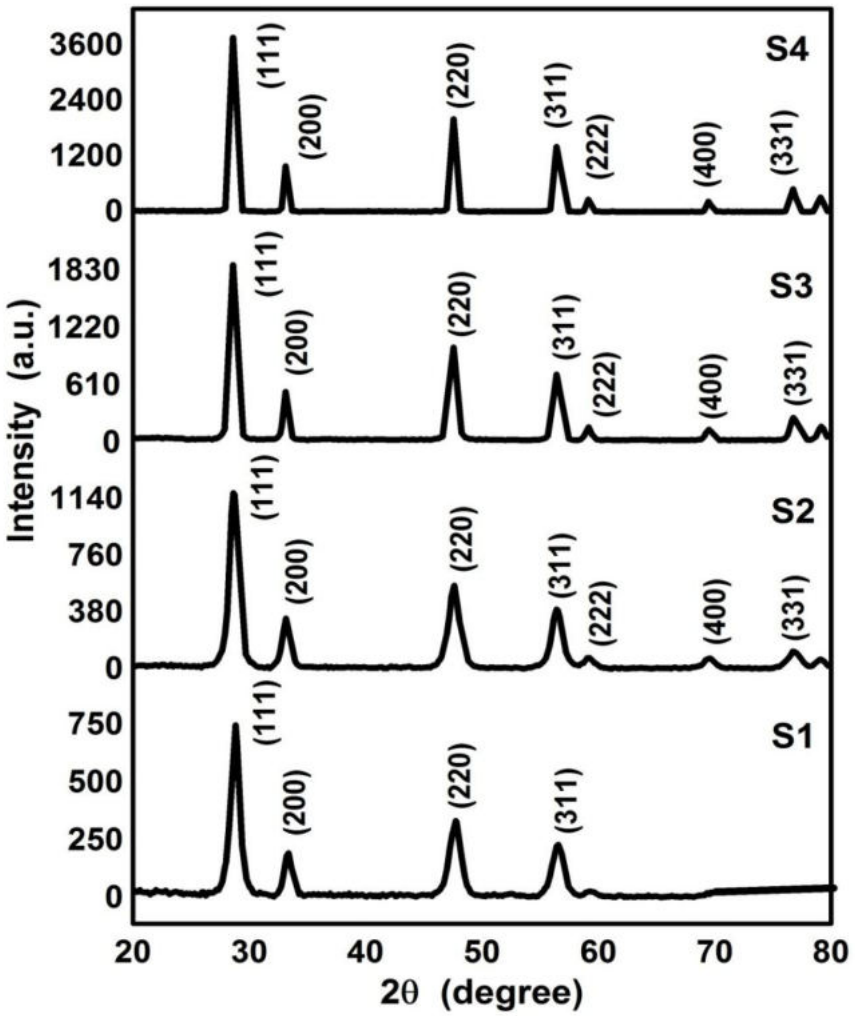

Fig.3.3 XRD patterns of CeO_2 nanoparticles calcined at different temperatures

The CeO_2 sample S1, which is calcined at 400^oC gives XRD peaks at (111), (200), (220) and (311). As the calcination temperature is increased, three more peaks at (222), (400) and (331) are formed, which indicate the increment in crystallization in a face centered cubic structure. The peaks become gradually sharper with increasing calcination temperature and are due to the increase in size of the particles caused by the coarsening of particles [2]. Intensity of diffraction peaks

are greatly modified for the samples due to increase in calcination temperature. Average size of cerium oxide nanoparticle samples are estimated using Scherrer equation [3] and obtained values are 7.3, 13.56, 18.45 and 30.65 nm for S1, S2, S3 and S4, respectively. The structural parameters of the samples S1, S2, S3 and S4 are tabulated in Table 3.1.Fig.3.3 shows that diffraction peaks become intense and their FWHM gradually decreases with increase in calcination temperature. The nanoparticles show larger crystallite size at higher calcinations temperatures, which may be due to the thermally promoted crystallite growth. The effect of calcination temperature on particle size is plotted in Fig.3.4. It is noticed that crystal growth rate gradually increases upto a calcination temperature of 700°C and thereafter becomes more steep. At low calcination temperature, the porosity is quite high and the pores are interconnected to maintain smaller crystal sizes [4]. However at higher calcination temperature, continuous grain boundary networks have been formed due to the bridging of small particles to increase the particle size.

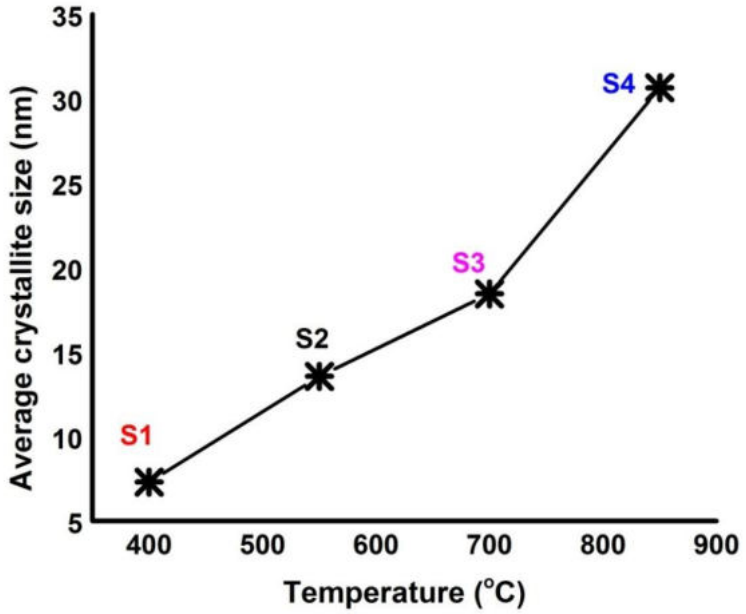

Fig.3.4 Effect of calcination temperature on crystallite size of CeO_2

The average particle sizes are estimated using the W-H method [5] as described in *Section 2.4.2.1*. W-H plots for the cerium oxide samples are presented in Fig 3.5.Table 3.1 presents the changes in geometric parameters of CeO_2 nanoparticles, when the calcination temperature changes from 400 to 850^{o}C. It can be seen that the average crystallite size calculated from Scherrer equation closely agree with the size estimated from Williamson-Hall plot. The lattice constant *a* of CeO_2 nanoparticles can be estimated from the spacing of the lattice planes *(hkl)* using Bragg's law [6]. It can be seen from Table 3.1 that the calcination process results in the increase of crystallite size and lattice contraction. The unit cell volume ($V=a^3$) for the samples S1,S2,S3 and S4 are calculated from XRD data and also presented in Table3.1.

dislocation density (δ) calculated for the sample S1,S2,S3 and S4 is $18.765x10^{-3}$, $5.439x10^{-3}$, $2.938x10^{-3}$ and $1.064x10^{-3}$ nm^{-2}, respectively. It can found that micro-strain and dislocation density values of the samples decreases with increase in calcination temperature, which indicates that defects like dislocations, edges or cuts are removed during calcination process [7].

Table 3.1 Structural parameters of CeO_2 nanoparticles

Sample	Average particle size (nm)		FWHM (111) plane	Lattice constant a (Å)	Lattice spacing $d_{(111)}$ (Å)	Unit cell volume (Å^3)	Micro strain ($x10^{-3}$)	Dislocation density ($x10^{-3}$) (nm^{-2})
	Scherrer method	W-H method						
S1	7.3	8.4	1.197°	5.403	3.1194	157.73	4.54	18.765
S2	13.56	12.56	0.749°	5.4	3.1176	157.46	3	5.439
S3	18.45	19.95	0.433°	5.39	3.1119	156.59	1.18	2.938
S4	30.65	33.44	0.251°	5.383	3.1078	155.98	0.979	1.064

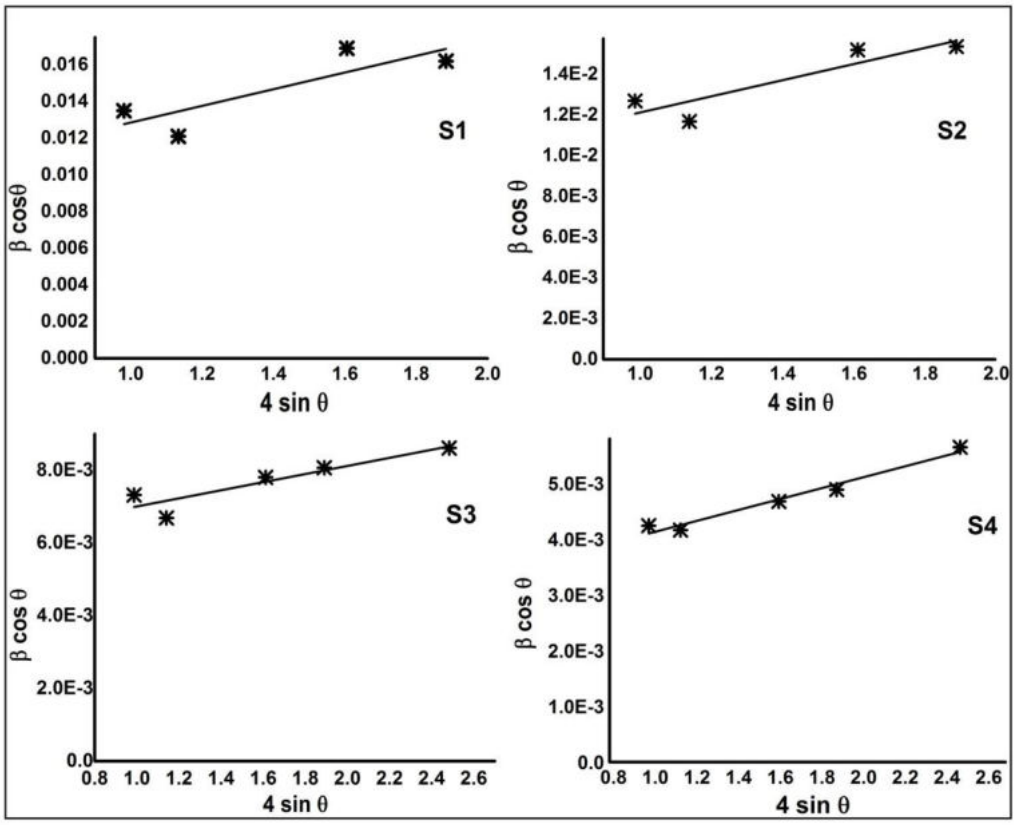

Fig.3.5 W-H plots of nanophaseCeO_2 samples

To summarize, the calcination of nanoceria results in increase in intensity of diffraction peaks, increase in crystallite size, decrease in micro-strain and dislocation density and decrease in lattice constant and unit cell volume. All these structural modifications can affect the physical properties of CeO_2 nanoparticles.

3.3.2.2 TEM analysis

Structural features of nanophase CeO_2 samples are examined by JEOL MODEL JEM-2100 electron microscope operated at 200 kV. Fig. 3.6 shows the TEM images of cerium oxide nanoparticles calcined at different temperatures. The bright field image of (Fig.3.6 (a)) sample S1 reveals that particles are not exactly spherical in shape and are agglomerated. Agglomeration of nanoparticles occurs because the nanoparticles tend to decrease the exposed surface in order to lower the surface energy [8]. However, the BF images of calcined samples clearly demonstrate the crystallite growth. Loose agglomeration of ceria nanoparticles is clearly seen in samples S3 and S4. The average size of the grains obtained from TEM images (S1=8 nm, S2= 14 nm, S3=20 nm and S4=32 nm) show good agreement with the XRD results. Polycrystalline nature of the sample is evident from HRTEM images of Fig.3.6(b). The bright spots in the SAED patterns (Fig.3.6(c)) of the samples confirm that all the samples have crystalline nature [9], as the SAED pattern of crystalline material will be bright spots and each bright spot in the SAED pattern arising from the Bragg reflection from individual crystallite.

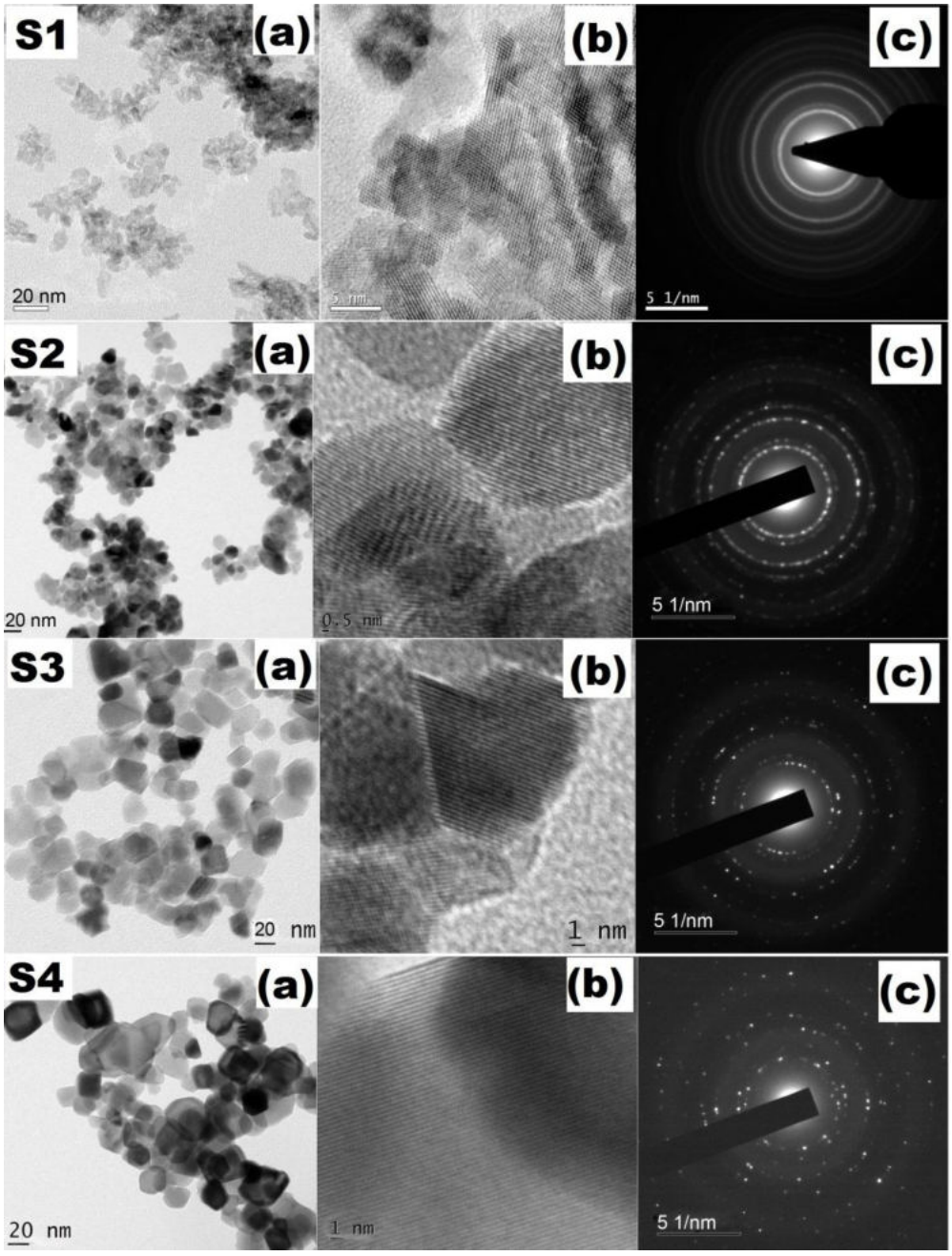

Fig.3.6 TEM images of CeO_2 nanoparticles

(a) Bright filed images (b) HRTEM and (c) SAED Patterns

3.3.2.3 SEM and EDX analysis

The surface morphology of the CeO_2 samples are analyzed with a scanning electron microscope JEOL MODEL JSM-6390LV, operating at 20 kV. Fig.3.7 shows SEM images of CeO_2 nanoparticle samples. It shows that thecalcined samples are not uniform in size and shape. The SEM images of the samples contain heterogeneous nanoparticle clusters. The elemental analysis of the sample calcined at 400^oC is done by energy-dispersive X-ray spectroscopy. The EDX pattern of the sample S1 is displayed in Fig.3.8. The peaks confirm that the product contains Ce and O. Besides, 2 mass % of impurity element C is observed, which is from the lacey Cu grid. The intense signal at 4.8 keV indicates that Ce is the major element. The mass and atom percentages of the sample are presented in Table 3.2.

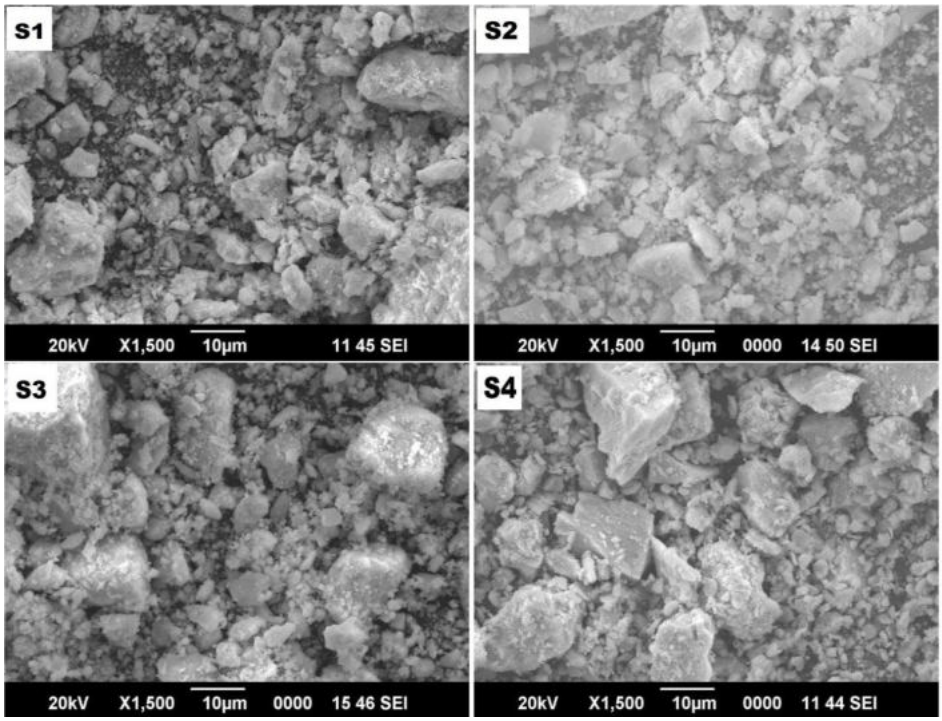

Fig.3.7 SEM images of CeO_2 nanoparticles

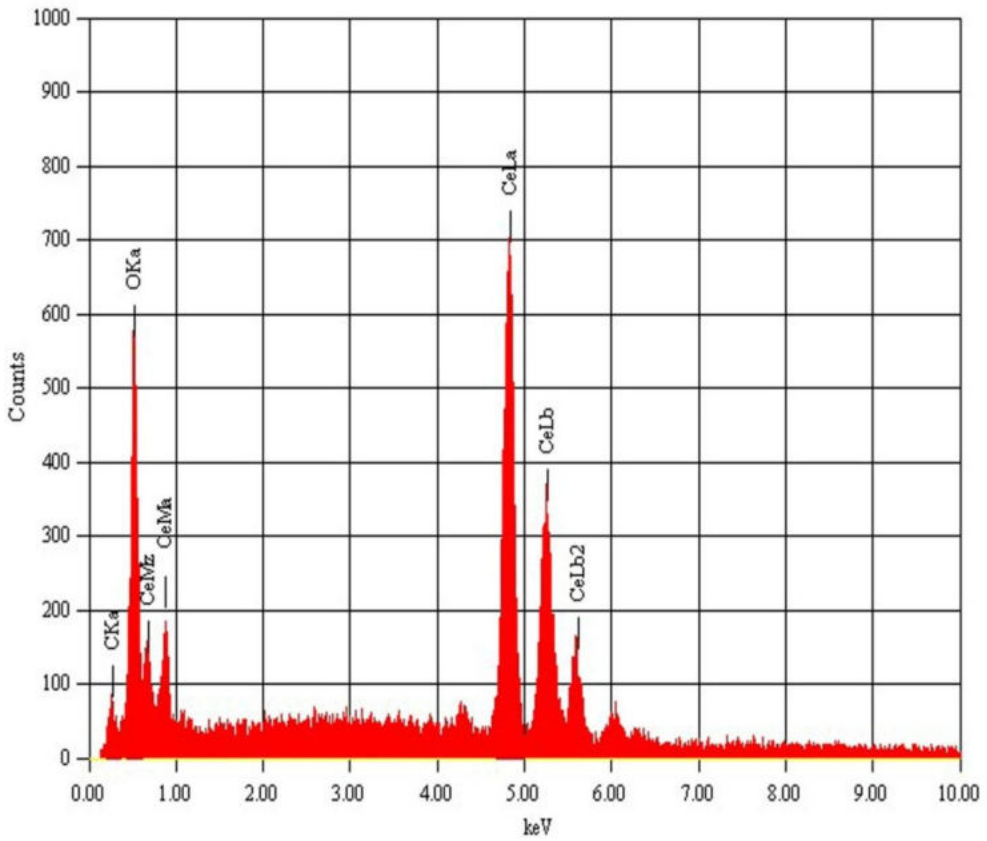

Fig.3.8 EDX pattern of CeO_2 nanoparticles calcinedat 400^{o}C (S1)

Table 3.2 EDX data of CeO_2 nanoparticles

Element	keV	Mass%	Atom%
C K	0.277	2	11.23
O K	0.525	11.11	46.88
Ce L	4.839	86.9	41.89
Total		100	100

3.3.2.4 FTIR analysis

The FTIR spectra in the transmission mode of the cerium oxide samples are recorded by Thermo Nicolet, Avatar 370 and displayed in Fig. 3.9. The FTIR spectra show all principal vibrational modes, which are in good agreement with literature values [10- 14]. The broad absorption peak at 2000-3400 cm^{-1} is assigned to OH stretching vibrations of H_2O in the sample [10]. The absorption bands at 1380 and 1630 cm^{-1} correspond to physically adsorbed water molecules [11]. FTIR illustrated absorption bands at 848 and 521 cm^{-1} are produced by CeO_2, which is the typical peak for the Ce-O stretching vibrations[12-14].Fig.3.9 shows that all absorption peaks are shifted towards higher wavenumber side as calcination temperature is increased, which may be due to particle size variation caused by the heat treatment. It is also observed that all the residual peaks are weak right from 500 cm^{-1} as most organics are burned off, during calcination resulting in the oxidation of cerium [15].

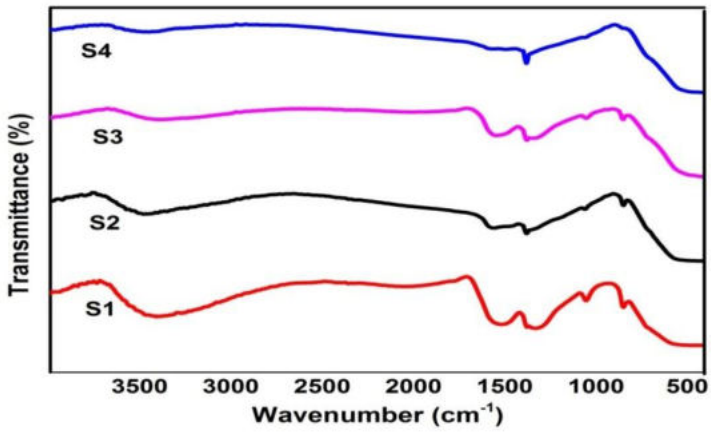

Fig.3.9 FTIR spectra of CeO_2 nanoparticles

3.3.2.5 Raman spectroscopy

Raman studies of the CeO_2 nanoparticles are performed by Raman spectrometer, Bruker RFS-27, using Nd-YAG laser, at room temperature. Cerium oxide has a cubic fluorite type structure and belongs to the (*Fm3m*) space group, as discussed in *Section 3.3.2.1*. This cubic structure has six optical-phonon branches, which yield three zone-centre frequencies. These frequencies are 272, 465 and 595 cm^{-1}, correlating to doubly degenerated TO mode, triply degenerate Raman-active mode and non-degenerate LO mode, respectively [16]. The triply degenerate Raman-active mode frequency can be directly detected by Raman measurements, whereas the TO and LO frequencies are given indirectly by fits to infrared reflectivity [17]. Details of the vibrational modes of CeO_2 are presented in Table 3.3.

Table3.3 Ramanvibrational modes of CeO_2 [18]

Mode	Frequency(cm^{-1})	Degeneracy	Description
IR	272	2	TO mode
Raman	465	3	F_{2g} mode
IR	595	non-degenerate	LO mode

Fig.3.10 shows Raman spectra of cerium oxide nanoparticle samples. The Raman active modes for the samples S1, S2, S3 and S4 are 462.49, 464.81, 465.9 and 465.98 cm^{-1}, respectively. This Raman active mode is attributed to a symmetrical stretching mode of the Ce-O8

vibrational unit, and is sensitive to any disorder in the oxygen sub-lattice resulting from thermal, doping or grain size induced non-stoichometry[18,19].It is observed that the Raman modes are shifted from 462.49 to 465.98 cm^{-1} as calcination temperature increases from 400 to 850°C, due to particle size variation.It can also seen that intensity of Raman peaks are elevated with increase in calcination temperature.This intensity variation might result due to the increase in vibrational amplitudes of the nearest neighbour bonds. [15]. The current results show some variation from the reported values for bulk sample and this variation could be due to the nanoscale size of synthesized ceria samples. The present experimental Raman mode of nanoceria samples are presented in Table 3.4, along with previous reported values for bulk and nano-CeO_2.

Table 3.4 Comparison of Raman modes of nanoceria with literature values

Sample	**Raman mode (F_{2g}) cm^{-1}**
S1	462.49
S2	464.81
S3	465.9
S4	465.98
Literature values	465.5 [21] 458 [22,23]
Bulk CeO_2	465 [20]

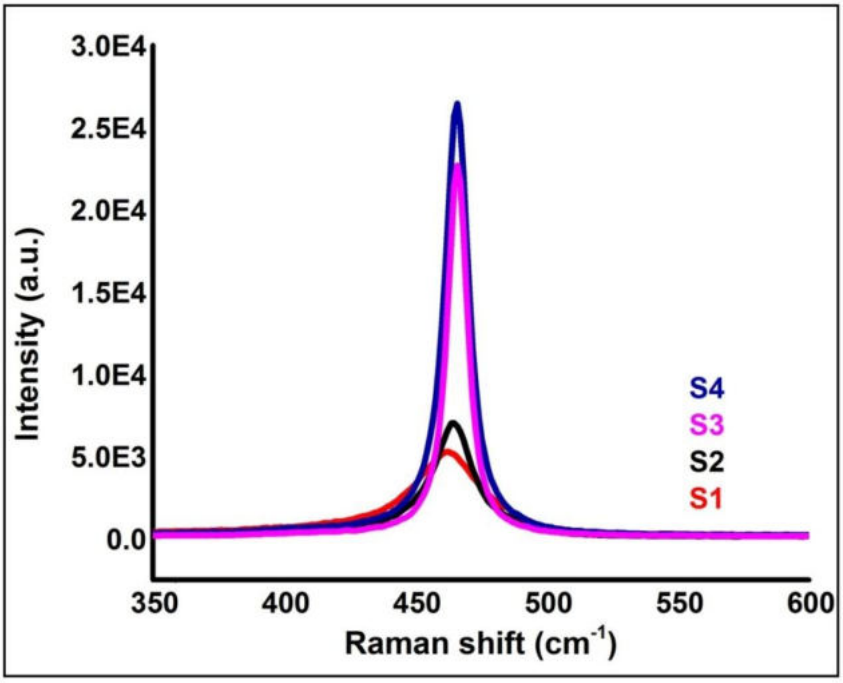

Fig.3.10 Raman spectra of CeO_2 nanoparticle samples

3.3.3 Optical properties

UV-vis absorption and photoluminescence spectra of the cerium oxide nanoparticles are presented here. The analyses are carried out by following the procedure as given in *Section 2.4.3.*

3.3.3.1 UV -visible absorption spectroscopy

Optical properties of the synthesized nanoceria samples are investigated by its absorption and emission spectra using spectroscopic techniques. UV-visible absorption spectra of CeO_2 nanoparticles calcined at different temperatures are collected by Kubelka Monk transformation methods using Shimadzu UV-2600 UV-Visible spectrophotometer. The optical absorption spectra of CeO_2 nanoparticle sample are presented in

Fig.3.11.The figure shows that all the samples show a strong absorption below 400 nm. The broad absorption bands located at 250 and 340 nm in the UV range originates from the charge transfer transition from $O^{2-}(2p)$ to $Ce^{4+}(4f)$ orbitals in CeO_2[24]. These spectral profiles indicate that the charge transfer transition of Ce^{4+} overlaps with the $4f^1$-$5d^1$ transition of Ce^{3+}[25].It can be seen from Fig. 3.11 that the absorption edges of calcined samples are shifted from 440 to 457.7 nm due to particle size variation caused by calcination.

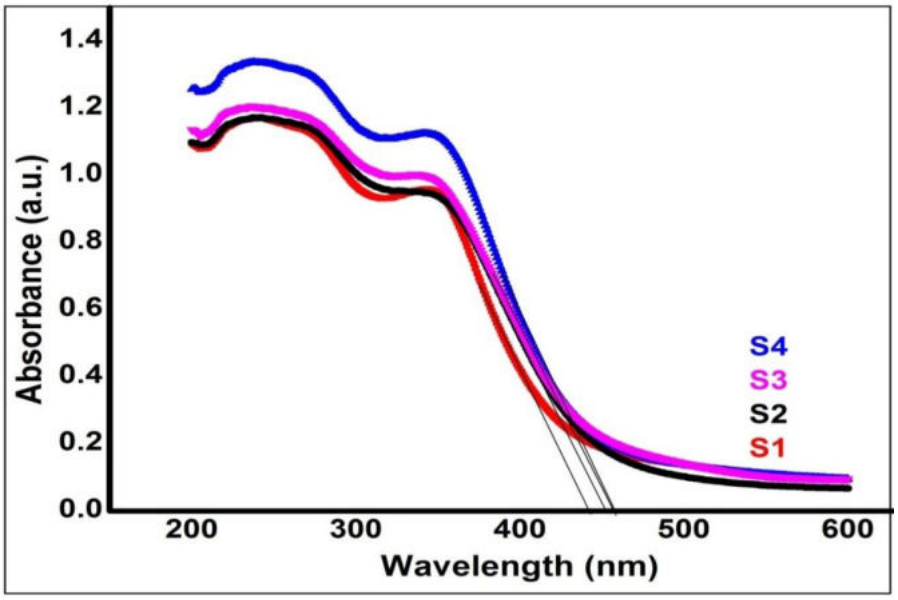

Fig.3.11 Optical absorption spectra of CeO_2 nanoparticle samples

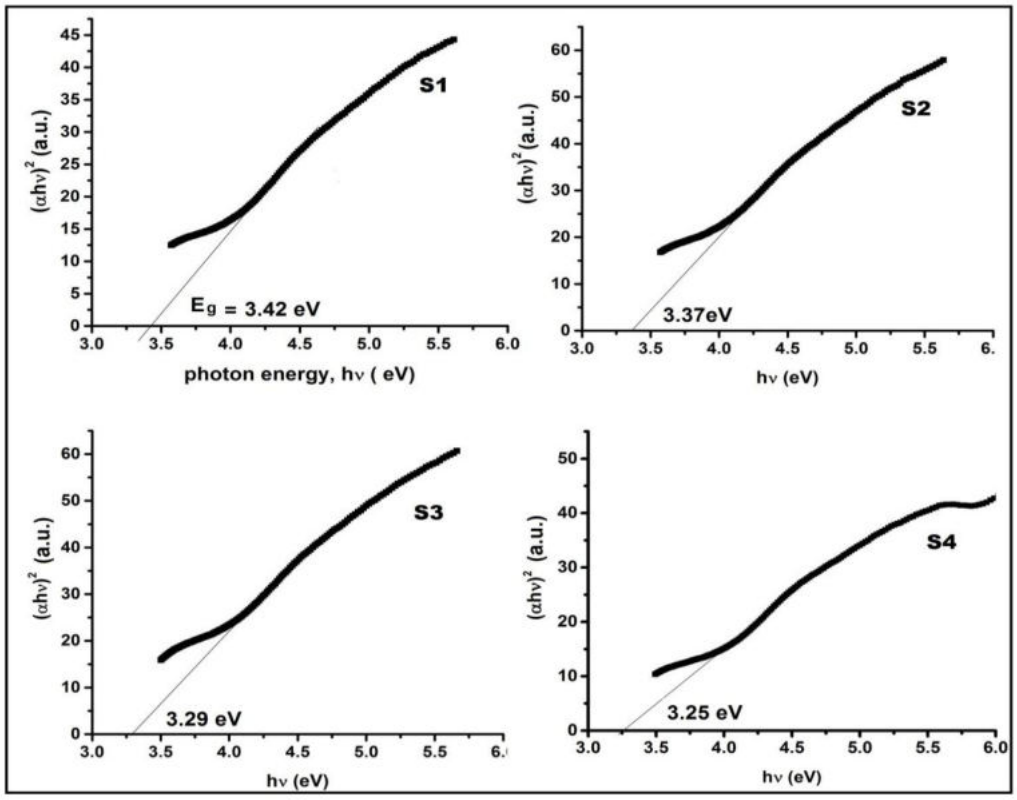

Fig. 3.12 Tauc plots of CeO_2 samples calcined at different temperatures

As ceria is a direct band gap material [26], the value of n in the Tauc are elation is ½. The band gap values obtained are 3.42, 3.37, 3.29 and 3.25 eV, respectively for samples S1, S2, S3 and S4 (Fig.3.12). The calculated $E_g$values of the samples S1,S2,S3 and S4 are tabulated in Table 3.5. The spacing of the electronic levels and the energy band gap are highly dependent on the particle size [27]. The calculations for the quantum size effect establish that there are no significant variations in the chemical composition in the structure of metal oxide as a result of particle size change[28]. The present results show a shift towards lower band gap energies due to an increase in particle size caused by

calcination. At higher calcination temperature, both the energy levels widen, which leads to contraction of the band gap.

In UV rays, ultraviolet A(315-400 nm) and ultraviolet B(280-315 nm) are not absorbed by the ozone layer, and this may cause skin cancer. From the Fig.3.11, it can be seen that most of the UV light in the range from 200–350 nm is absorbed by theCeO_2nanoparticles. Thus, ceria nanoparticles can be used as a UV blocker. In short, CeO_2 nanoparticles are suitable for UVA and UVB filtration, because this nontoxic material has good UV absorption in the range from 200-350 nm. This property of CeO_2 nanoparticles can be used in cosmetic products to protect skin against UVA and UVB rays [29]. Moreover, the present investigation proves that nanoceria is a suitable candidate for the construction of inorganic UV filters.

Table 3.5 Optical band gap of CeO_2 nanoparticle samples

Sample	Optical band gap E_g (eV)	Optical absorption edge (nm)
S1	3.42	440
S2	3.37	452
S3	3.29	456
S4	3.25	457.7

3.3.3.2 Photoluminescence spectroscopy

The room temperature photoluminescence spectra of CeO_2 powder samples are recorded using a Fluoromax-3 spectrophotometer, under the excitation wavelength of 330 nm and are shown in Fig.3.13. Sample S1 shows a good UV emission at 363 nm (3.4 eV), which is due to the hopping from the localized *Ce 4f* state to the *O 2p* valence band. The blue emission bands at 419 nm (2.96 eV) and emissions at 436.3 nm (2.84 eV) and 447.6 nm (2.77 eV) are related to the hopping from different defect levels to the O_2P level [30]. Blue green emission at 481nm (2.58 eV) and 490 nm (2.53 eV) are due to the surface defects in the CeO_2 nanoparticle. A good green emission at 545 nm (2.23 eV) is due to the presence of oxygenvacancies incorporated during the preparation of the CeO_2 sample [31]. All samples show a good strong blue emission at 466 nm(2.66 eV), which is due to the presence of abundant defect states. The present results are consistent with that reported for CeO_2 in the literature [32].

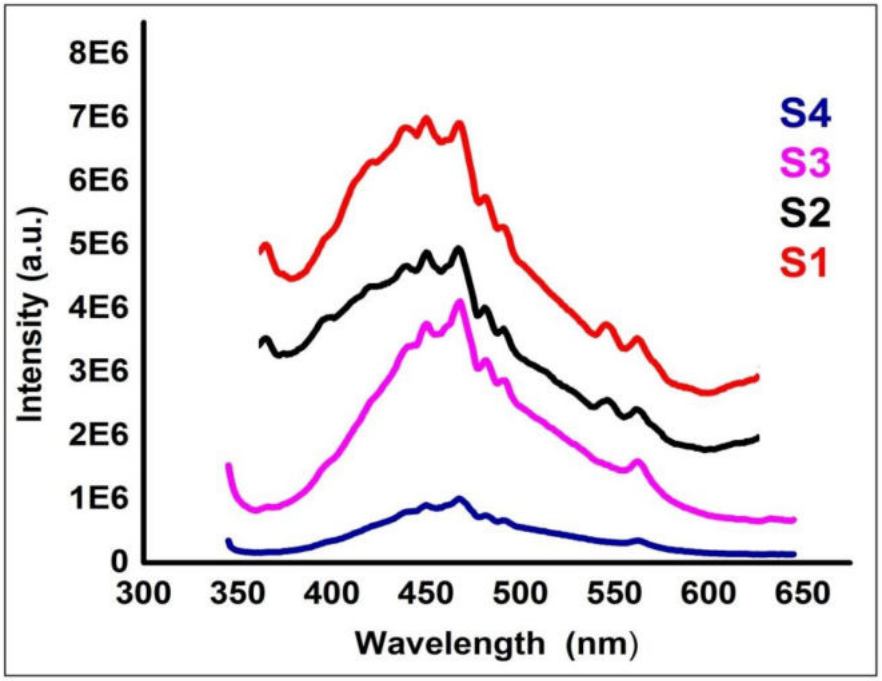

Fig.3.13 Photoluminescence spectra of CeO_2 nanoparticles

It can be seen from Fig.3.13 that the PL emission bands are red shifted as calcination temperature is increased, due to crystallite size variation. Moreover, it can be seen that intensity of PL spectra decreases as calcination temperature increases. It is interesting that PL intensity as well as photocatalytic activity of nanoceria can be modified by choosing suitable calcination temperature [15]. The broad emission band ranging from 350 to 575 nm of all the samples could be the result of defects, including oxygen vacancies in the crystal with electronic energy levels below the *4f* band [33]. As PL of nanoceria shows strong emission at 466 nm (due to defects such as dislocations), it can be used as an excellent oxygen ion conductor. This property of nanoceria can be used for developing efficient solid oxide fuel cells.

Fig.3.14 exhibits the CIE chromaticity diagram of the calcined samples of CeO_2 nanoparticles. The *x*and *y* chromaticity co-ordinates under the excitation of 330 nm are calculated in CIE XYZ colour space and are given in Table 3.6.The greenish-blue emission is obtained with CIE coordinates(0.18846, 0.26176), (0.18419, 0.24967), (0.20661, 0.28346) and (0.20521, 0.28132) for the samples S1,S2,S3 and S4, respectively. This result is also consistent with the PL spectra of the samples. Moreover, CeO_2 nanoparticles can be used to construct near ultraviolet (NUV) light excited LEDs.

Table 3.6 Chromaticity co-ordinates of S1, S2, S3 and S4

Sample	S1	S2	S3	S4
x	0.18846	0.18419	0.20661	0.20521
y	0.26176	0.24967	0.28346	0.28132

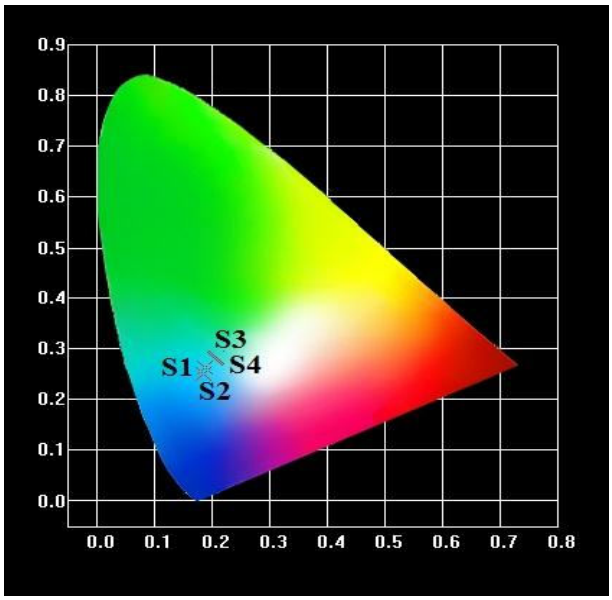

Fig.3.14 CIE chromaticity diagram of CeO_2 nanoparticles

3.3.4 Electrical properties

The electrical studies have been done by following the procedure given in *Section 2.4.4.* The samples S1, S2,S3 and S4 are consolidated in the form of cylindrical pellets of diameter 13 mm and thickness 1.2 mm by applying a pressure of ~ 7GPa using a hydraulic press. Dielectric and AC conductivity measurements are carried out using an impedance analyzer (*Wayne Kerr H-6500B model*).

3.3.4.1 Frequency and temperature dependence of dielectric constant

The variation of dielectric constant with frequency of sample S1 at temperatures from 303 to 423 K is shown in Fig.3.15. The observed dielectric property is frequency dependent, which can be explained on the basis of Maxwell-Wagner model [34].It is noticed that the real part of dielectric constant ε' for all temperatures has high values at lower frequencies, which decreases rapidly as frequency increases and attains a constant value at higher frequencies. For 303 K, the value of ε' is 66 at 100 Hz, which is decreased to 8.7 at 10 MHz. At 393 K, the corresponding values are 68 and 9.9. The corresponding values of dielectric constant at 423 K are 183.1 (100 Hz) and 18.6 (10 MHz), respectively.

The dielectric behaviour of the nanomaterial is due to different types of polarization present in the material. The dielectric structure is composed of a highly conducting grain separated by relatively poor

conducting grain boundaries. This causes localized accumulation of charges under the influence of electric field, which produces interfacial polarization. The effect of grain interfaces is highly observable at lower frequencies where ε' is large. The space charge polarization at the interfaces can also be contributed to the dielectric permittivity at lower frequencies [35]. When the frequency is increased, the dipoles will no longer be able to rotate rapidly. As a result, their oscillations begin to lag behind those of the applied field. As the frequency is further increased, the dipole will be completely unable to follow the field and the orientation stopped. For this reason, ε' decreases at a higher frequency approaching a constant value due to the interfacial polarization [35].

As can be seen from Fig.3.15, the dielectric constant increases with increase in temperature, which is mainly due to the polarization of interfacial dipoles that are strongly dependent on temperature [30]. When temperature increases, the accumulation of charges on the grain boundaries increases and hence, an increase in the interfacial polarization occurs at lower frequencies. Therefore the dielectric polarization increases, resulting in an increase of ε' with temperature at lower frequencies.

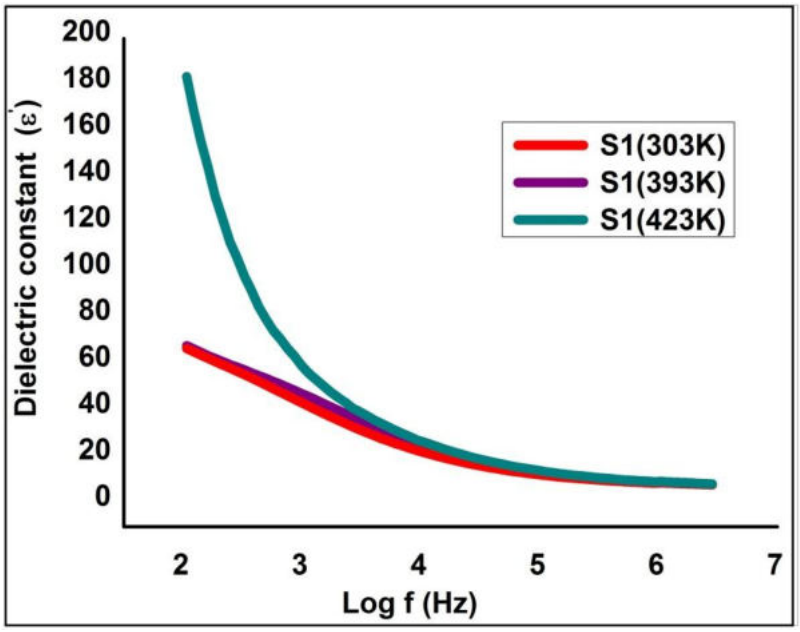

Fig. 3.15 Variation of dielectric constant (ε') with frequency of sample S1 at different temperatures

Fig.3.16 shows a similar variation of dielectric constant with frequency for all the calcined samples at 303 K, but the values are shifted downward with the increase of calcinations temperature. This may be due to high particle size caused by calcination process. As calcinations temperature increases, grain boundary increases and grain density decreases due to lattice expansion. This leads to the reduction in interfacial polarization and dielectric constant. Sample (S1) calcinated at 400°C has a large value of dielectric constant. The value of ε'changes from 57 at 100 Hz to 9at 10 MHz for sample S2, while its value changes from 48 to 1.6 for sample S3, and from 37 to 1.15 for sample S4, respectively.

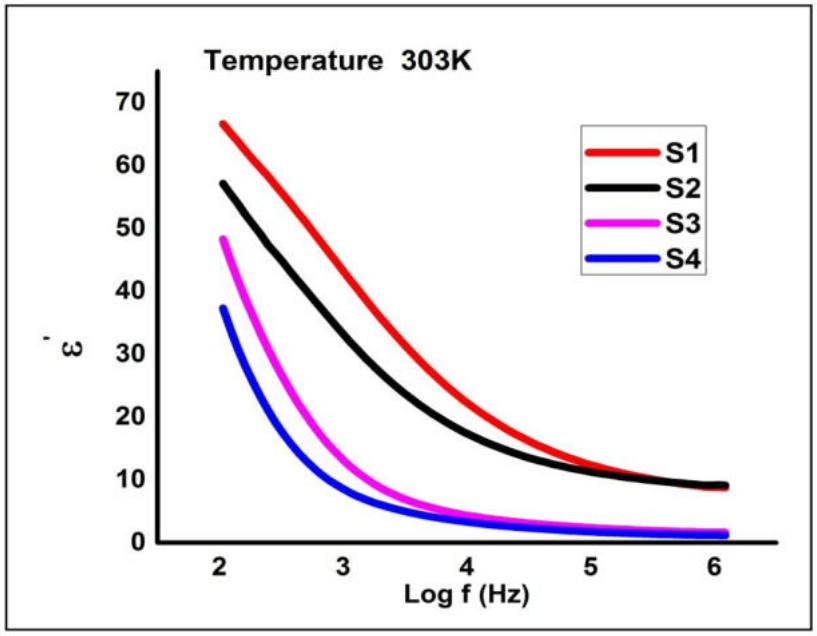

Fig. 3.16 Variation of dielectric constant (ε') with frequency of samples S1, S2, S3 and S4 at 303 K

The dielectric constant ε' for CeO_2 reported in literature is 52 [36], however, the present value is 66 (S1). The enhancement of ε' might occur due to the increase of ion mobility due to the expansion of lattice spacing. The lattice expansion might occur due to the presence of oxygen vacancies and reduction of Ce^{4+} cations to Ce^{3+} cations. CeO_2 nanoparticles with high values of ε' (66 (100 Hz) at room temperature; 183 (100 Hz) at 423 K) at low frequencies are suitable for silicon-based devices such as gate dielectric in complementary metal oxide semiconductor (CMOS) devices. To keep the capacitance of the MOS capacitor above certain limits for the better performance, SiO_2 can be replaced with a high dielectric constant material like CeO_2, which would enable the use of thicker gate layer so that the leakage current through

the device is reduced and thereby improve the gate dielectric reliability [37,38].

3.3.4.2 Frequency and temperature dependence of loss tangent

In nanomaterials, impurities, defects and space charge formation in the interface layers together produce an absorption current causing a dielectric loss [39]. Tangent loss (*Tanδ*) is the loss of electromagnetic energy propagating inside a dielectric material. As the frequency of the applied field increases the absorption current gets reduced and hence, the dielectric tangent loss will be decreased as shown in Fig.3.17. The hopping probability per unit time increases with increase in temperature, as a result the loss tangent also increases [40-42]. The loss in CeO_2 can be explained by the electronic hopping model, which considers the frequency dependence of the localized charge carriers hopping in a random array of centres. This model is applicable for materials in which the polarization responds rapidly to the appearance of an electron on any one site, so that the transaction occurs effectively into the final state [43]. In the high frequency region, *Tanδ* becomes almost constant because the electron exchange interaction (hopping) between the Ce^{3+} and Ce^{4+} cannot follow the alternatives of the applied electric field beyond a critical frequency. At higher frequency end, the loss factor is caused by the conversion of movement of charges into vibration of the lattices(phonons) [44].

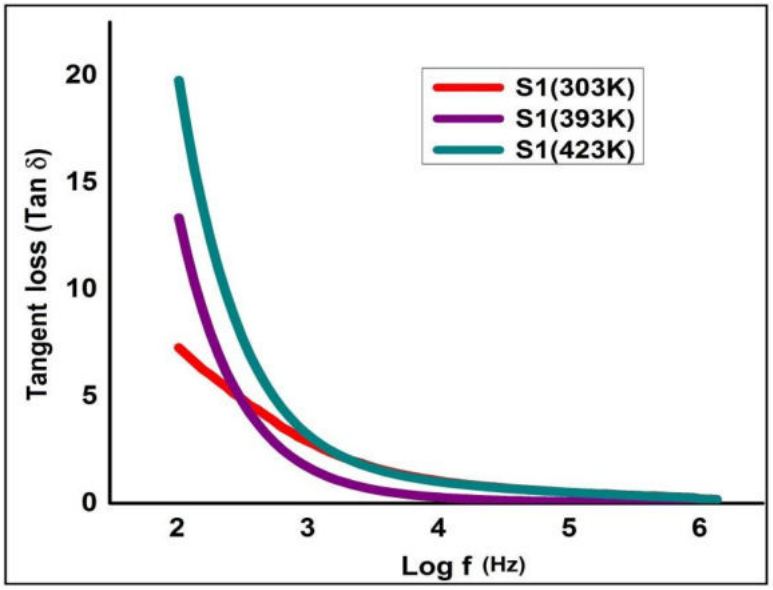

Fig.3.17 Variation of loss tangent (*Tanδ*) with frequency of sample S1 at different temperatures

It is found that the values of *Tanδ* initially decrease rapidly with frequency and then decrease at a slower rate. For sample S1 at 303 K, value of *Tanδ* is7 at 100 Hz which decreases slowly to 0.199 at 10MHz. At 393 K, the corresponding variation is from 13 to 0.15. For 423 K, *Tan δ* has a value of 19.53 at 100 Hz which decreases to 0.75 at 10 MHz. The variation of *Tanδ* with frequency for different samples at room temperature is shown in Fig.3.18. The figure shows that loss tangent decreases with the increase in calcination temperature. It can be seen that the sample S1 calcinated at 400 ^{o}C has a large value for the loss tangent (*Tanδ*) at room temperature. At 100 Hz, the *Tanδ* value are7.2, 6.6, 5.2 and 4.3 for the samples S1,S2, S3 and S4, respectively.

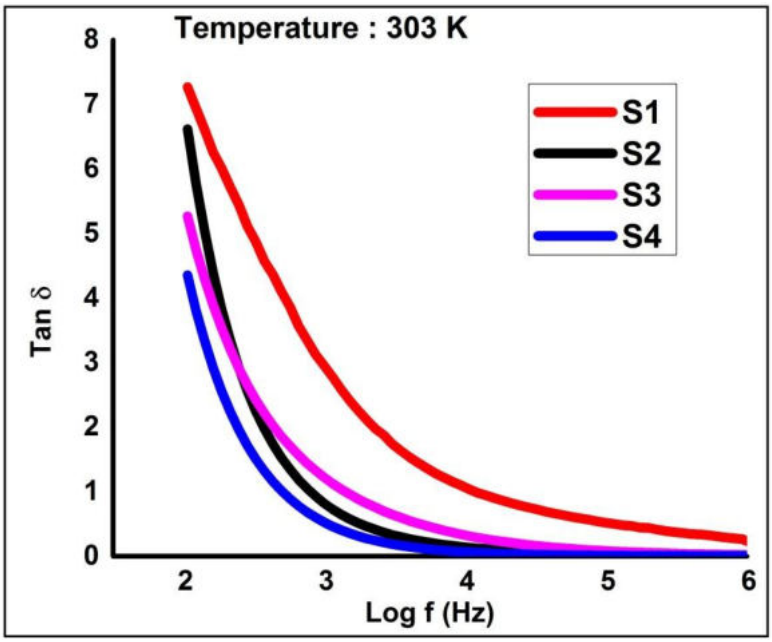

Fig. 3.18 Variation of loss tangent (*Tanδ*) with frequency of samplesS1, S2, S3 and S4 at 303 K

As calcination temperature increases, volume percentage of interface boundaries and amount of defects that cause various kinds of polarizations might decrease [35]. Hence, the values of dielectric loss tangents lower with respect to rise in calcination temperature. Nanoceria with low values of dielectric constant and loss tangent at higher frequencies is important for the fabrication of materials for ferroelectric, photonic and electro-optic devices [39].

3.3.4.3 Frequency and temperature dependence of AC conductivity

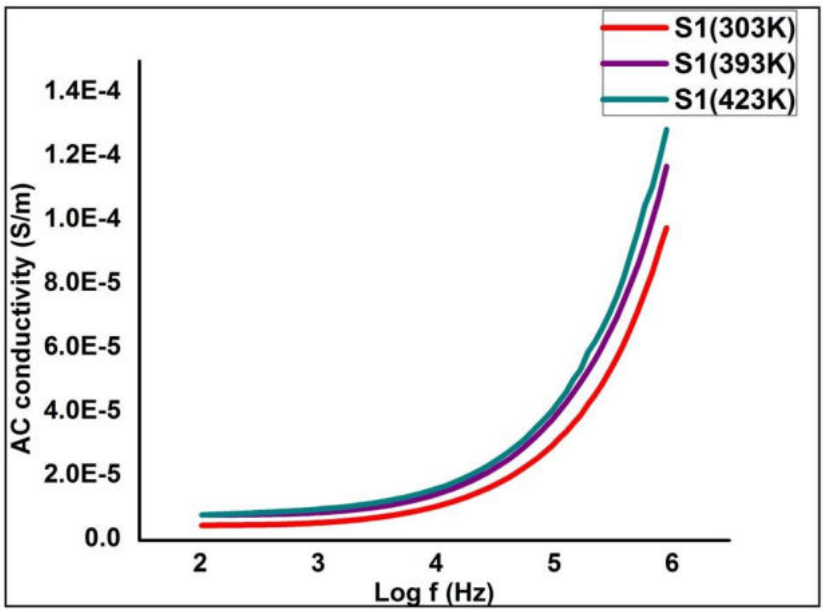

Fig.3.19 The variation of AC conductivity with frequency of sample S1 at different temperatures

The variation of AC electrical conductivity as a function of frequency for sample S1 is shown in Fig. 3.19. At low frequencies, AC conductivity (σ_{ac}) has a small value which increases at higher frequencies. The values are shifted upwards as the temperature is raised. It is clear from the figure that the conductivity increases as frequency is increased. Microstructure of the samples plays a major role in the frequency dependence of the conductivity. Also, CeO_2 shows mainly electronic and ionic conductivity in air [45].

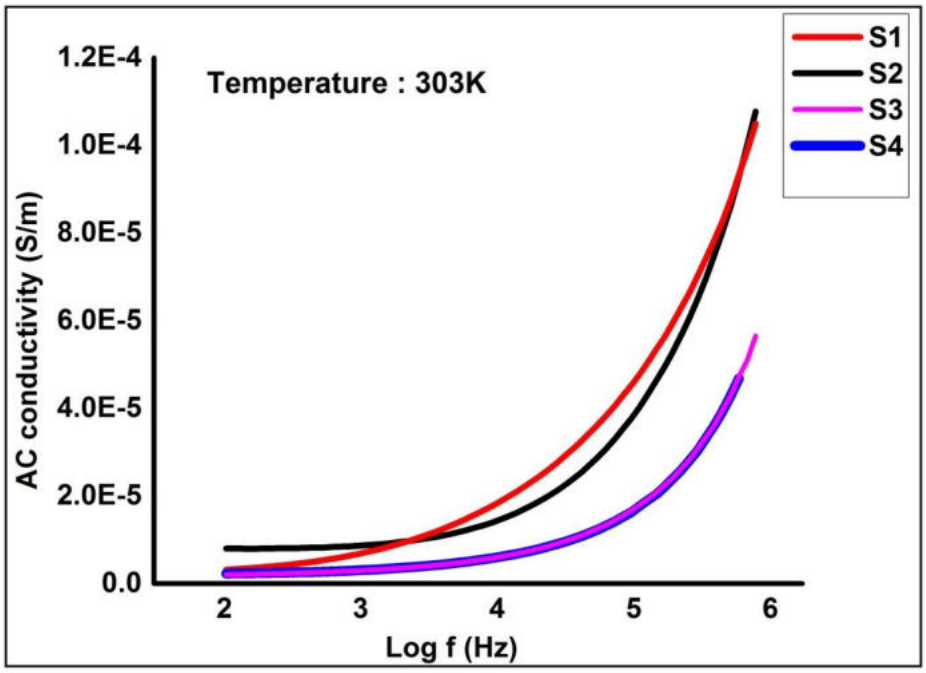

Fig.3.20 Variation of AC conductivity with frequency of samples S1,S2, S3 and S4 at 303 K

When temperature increases, there is easy transition of charge carriers from valence band to conduction band due to small-size of particles in the sample, resulting in increased conductivity [46, 47]. The high temperature electrical conduction occurs due to jumping (hopping) of electrons from Ce^{3+} ion to a neighbouring Ce^{4+} ion [48]. For sample S1, the maximum conductivity at 303K is 1.02×10^{-4} S/m. But at 393 and 423 K, the AC conductivity values are 1.17×10^{-4} S/m and 1.28×10^{-4} S/m respectively. The variation of σ_{ac} for samples S1, S2, S3 and S4 at 303 K is shown in Fig. 3.20. It is found that the AC conductivity decreases with increase in calcination temperature. Higher calcination temperature reduces the grain boundary density as well as the electron density, which in turn reduces conductivity.

According to Elliot's barrier hopping model, the AC conductivity,

$$\sigma_{ac} = n\pi 2NNp\varepsilon'\omega R_{\omega}^{6}/24, \qquad \textbf{(3.1)}$$

where n is the number of polarons involved in the hopping process, NNp is proportional to the square of the concentration of states and R_{ω} is the hopping distance [48, 49]. The hopping distance decreases with increase in calcination temperature, which in turn decreases σ_{ac} as is evident from the *Eq. 3.1*.

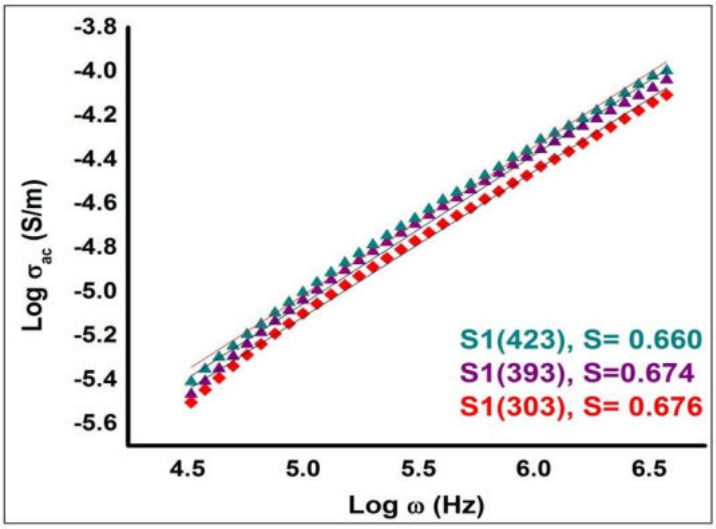

Fig.3.21 *Log(σ_{ac})* versus *log(ω)* plots of the sample S1 at different temperatures

Fig.3.21 shows the variation of *log $\sigma_{ac}(\omega)$* with frequency of the sample S1 at different temperatures. Values of the frequency exponent *S* are calculated from the slope of the straight lines of the data in Fig. 3.21. It is observed that *S* decreases with increase in temperature from 0.676 to 0.660 (Fig. 3.21). All the observed *S* values are less than unity, which is in agreement with the barrior hopping model[50].

3.4 Conclusions

- Nanostructured CeO_2 particles have been successfully synthesized by chemical precipitation technique using cerium nitrate and ammonium carbonate.
- Effect of calcinations temperature on the structural, optical and electrical properties of synthesized samples are studied.
- The structural characterization results confirm the nanocrystalline nature and cubic fluorite structure of CeO_2.
- The calcination of nanoceria samples results in structural modifications such as increase in intensity of diffraction peaks, increase in crystallite size, decrease in micro-strain and dislocation density and decrease in lattice constant and unit cell volume.
- FTIR and Raman spectra studies confirm the successful formation of nanoceria with fundamental modes and the observed shifts in the spectra reveal a significant effect of calcination process.
- Raman bands are red shifted and their intensity is found to increase with increase in calcination temperature. The observed optical band gap is very close to the reported value and is found to decrease with increase in calcinations temperature.
- PL bands are modified and shifted towards blue region with increase in calcination temperature, which is attributed to the surface structural modifications and particle size variation caused by calcinations.

- PL emission for all the samples is found to be in the greenish-blue region showing their potential use for making near UV (NUV) light excited LEDs and solid oxide fuel cells.
- Electrical characterization also exhibits a profound effect of calcination temperature for the synthesized samples.
- The dielectric constant and tangent loss are found to be decreased for all the samples with increase in frequency.
- The room temperature dielectric constant (ε') of CeO_2 nanoparticle sample calcined at $400^oC$is 66 at100 Hz, which constitutes the highest value ever reported.
- The AC conductivity of nanoceria is found to be high for higher frequencies at a given temperature showing small polaron hopping in the samples, which is confirmed using Jonscher's universal power law. Besides, the AC conductivity values are shifted upwards as the temperature is raised.
- The values of dielectric constant, dielectric loss tangent and AC conductivity are decreased as calcination temperature is raised.
- The nanophase CeO_2 can be a promising material for the high dielectric gate in CMOS devices because of its higher dielectric constant, desired structural and compositional properties.
- The desired structural and optical properties of CeO_2 nanoparticles make it as a potential material for cosmetic, photcatalytic and optoelectronic applications.

References

[1] P. S .Anjana, M .T. Sebastian, J. Am.Ceram.Soc., 92(1) (2009) 96-104.

[2] T. Dhannia, S. Jayalekshmi, M. C. Santhosh Kumar, T. Prasada Rao, A. Chandra Bose, J. Phys. J Alloys Compd., Chem. solids 70 (2009) 1443.

[3] B.D. Cullity, S. R. Stock, Elements of X-ray Diffraction, 3rdEdn, Prentice Hall, New Jersey (2001).

[4] T. Lai, Y. Shu, G. Huang, C. Lee and C. Wang, J. Alloys Compd., 450 (2008) 318.

[5] G. K Williamson and W. H Hall, Acta. Metall. 1(1953) 22.

[6] Charles Kittel, Introduction to Solid State Physics, John Wiley and Sons, New York (1997).

[7] V. N Morris, R. A. Farrell, A. M Sexton, M.A Morris, J. Phys. Conf. Ser. 26 (2006) 119.

[8] C. Hu, Z. Zhang, H. Liu, P. Gao, Z. L. Wang, Nanotechnology 17 (2006) 5983.

[9] Y.X. Li, W. F. Chen, X. Z. Zhou, Z.Y.Gu, C.M.Chen, Mater. Lett.59 (2005) 48.

[10] J. Gao, F. Guan, Y. Ma, W. Yang, J. Kang, H. Deng and Y.Qi, Rare Metals, 20 (2001) 217.

[11] C. Ho, J. C. Yu, T. Kwang, A. C. Mark and S. Lai, Chem. Mater.,17(17) (2006) 4514.

[12] S. B. Khan, M. Faisal, M. M. Rahman and A. Jamal,Sci. Tot. Environ, 409 (2011) 2987.

[13] F. Niu, D. Zhang, L. Shi, X. He, H. Li, H. Mai and T.Yan T, Mater. Lett.,63 (2009) 2132.

[14] M. Palard, J. Balencie, A. Maguer and J. F. Hochepied, Mater. Chem. Phys., 20 (2010) 79.

[15] K. K. Babitha, A. Sreedevi, K. P. Priyanka, Boby Sabu and Thomas Varghese, Indian J. Pure Appl. Phys., 53(2015)596-603.

[16] K.K. Babitha, K.P. Priyanka, A. Sreedevi, S. Ganesh and Thomas Varghese, Mater. Charact., 98 (2014) 222–227.

[17] W. H. Weber, K. C. Hass, J. R. McBride, Phys. Rev., B 48 (1) (1993) 178.

[18] I. Kosacki, V. Petrovsky, H. U. Anderson, P. Colomban, J. Am. Ceram. Soc., 85 (2002) 2646.

[19] F. Marabelliand P.Wachter, Phys. Rev., B, 36 (1987) 1238.

[20] M. M. Sinha, P. Ashdhir, H. C. Gupta, B. B. Tripathi, Phys. Status Solidi, B 191 (1) (1995)101.

[21] Santi Maensiri, Chivalrat Masingboon, Paveena Laokul, Wirat Jareonboon, Vinich Promarak, Philip L. Anderson, Supapan Seraphin, Cryst. Growth Des., 7 (5) (2007) 950.

[22] Sher Bahadar Khan, M. Faisal, Mohammed M. Rahman, Kalsoom Akhtar, Abdullah M.Asiri, Anish Khan, Khalid A. Alamry,

Matovic B. Boskovic, M. Zinkevich, F. Aldinger,Int. J. Electrochem. Sci., 8 (2013) 7284.

[23] Jennnifer Strunk, William C. Vining, Alexis T. Bell, J. Phys.Chem.,C 115 (2011) 4114.

[24] Z. Wang, Z .Quan and Lin ,J. Inorg. Chem., 46 (2007) 5237.

[25] L. Yin, Y. Wang, G. Pang, Y. Koltypin and A. Gedanke, J. Coll. Inter. Sci.,246(1) (2002) 78.

[26] H. Gu, M. D. Soucek, Chem. Mater., 19 (2007) 1103–1110.

[27] E. Ziegler, A. Heinrich ,H. Oppermann, G. Stover, Phys. Status Solidi A, 66 (1981) 635.

[28] A. Bensalem, J. C. Mullerand F. Bozon-Verduraz, J. Chem. Soc., Faraday Trans, 88 (1992) 153.

[29] T. Herrling, M. Seifert, K. Jung, SOFW-Journal, Cosmetics, 139 (5) (2013).

[30] P. Patsalas, S. Logothetidis, Phys. Rev. B 68 (2003) 035104.

[31] S. Phoka, P. Laokul, E. Swatsitang, V. Promarak, S. Seraphin, S. Maensiri, Mater. Chem. Phys., 115 (2009) 423.

[32] S. Phokha, S. Pinitsoontorn, P. Chirawatkul, Y. Poo-arporn, S. Maensir, Nanoscale Research Letters., 7 (2012) 425.

[33] A. H. Morshed, M. E. Moussa, S. M. Bedair, R. Leonard, S. X. Liu and N. E. Masry N E, Appl. Phys. Lett., 70 (1997) 1647.

[34] K.W. Wagner, Am.Phys.,40, 317, 1973.

[35] B. Tareev, Physics of dielectric materials, Moscow: Mir Publishers (1979).

[36] D. Matsushita, Y. Nishikawa, N. Satou, M. Yoshiki, T. Schimizu, T. Yamaguchi, H. Satake, N. Fukushima, Jpn. J. Appl. Phys., 43 (2004) 1795.

[37] C. H. Chen, I. Y. Chang, J. Y. Lee, F. Chiu, Appl. Phys. Lett., 92 (2008) 043507.

[38] M. Chakraverty, H. M. Kittur, Adv. Mater. Res., 584 (2012) 428.

[39] K. P. Priyanka, K. K. Babitha, A. Sreedevi, X. Sheena,E. M. Mohammed and Thomas Varghese, J.Electroceram., 32(4) (2014) 361-368.

[40] J. Mathew, S. Kurien, S. Sebastian, K.C. George, Ind. J. Phys., 78 (9) (2004) 947.

[41] V. Murthy, J. Sobhanadri, Phys. Status Solidi, A 36 K (1976) 133.

[42] P. Merchant, C. Elbaum, Solid State Commun., 26 (1978) 73.

[43] E. Kumar, P. Selvarajan, K. Balasubramanian, Rec. Res. Sci. Tech., 2(4) (2010) 37.

[44] J. Hasson, F.M. Yen, M. Hashim, Z. Abbas, Z. A.Wahab, A. Zakaria, Ionics, 13(2007) 219.

[45] Y. M. Chiang, E. B. Lavik, I. Kosacki, H. L. Tuller, J. Y. Ying, J.Electroceram., 1(1997) 7.

[46] M. K. Akhtar, Y. Xiong, S. E. Pratsinis, AIChE, J 37 (1991) 1561.

[47] Z. Ding, X. Hu, G.Q. Lu, P.L. Yue, P.F. Greenfield, Langmuir 16 2000) 6216.

[48] K. I. Naik, T.Y. Tien, J. Phys. Chem. Solids, 38 (1978) 311.

[49] S. R. Elliott, Solid State Commun., 27 (1978) 749.

[50] A. R. Long, Adv. Phys., 31 (1982) 553.

Chapter 4

EFFECT OF 8 MeV ELECTRON BEAM IRRADIATION ON THE THERMAL, STRUCTURAL, OPTICAL AND ELECTRICAL PROPERTIES OF NANOCERIA

4.1 Introduction

Studies on the use of electron beam irradiation for modifying the surface properties of nanoparticles are sparse. Most of these studies prove that electron beam irradiation is an efficient method to improve the optical and electrical performance of nanomaterials. The dose dependent effects of 8 MeV electron beam irradiation on the thermal, structural, optical and electrical properties of cerium oxide nanoparticles are presented in this chapter. Synthesis procedures adopted for the preparation of cerium oxide nanoparticle used in this study are clearly described in *Section 3.2*. The experimental details about the electron beam irradiation are mentioned in *Section 2.5*. CeO_2 nanoparticles calcined at 400^oC are electron irradiated at a dose of 0, 5 and 10 kGy and are designated as $S1_{(0)}$,$S1_{(5)}$ and $S1_{(10)}$ respectively. A comparative study of thermal, structural, optical and electrical properties of bare ($S1_{(0)}$) and EB irradiated samples are also presented in this chapter.

4.2 Results and discussion

4.2.1 Thermal analysis

The thermal studies of of bare and EB irradiated CeO_2 nanoparticle samples are carried out by Perkin Elmer STA 6000. The samples are heated from 40 to 850^oC at a rate of 20^oC/min. TGA/DTA/DTG curve of bare and EB irradiated CeO_2 samples are presented in Fig.4.1. TGA curves for irradiated samples show a continuous weight loss up to 650°C. In this, the weight loss from 40 to 200°C is attributed to the loss of moisture and trapped solvents [1]. But, the weight loss from 200 to 650^oC is mainly due to the combustion/decomposition of the organic residues. The DTG curve of sample $S1_{(0)}$ shows a very strong peak at 243^oC with a weight loss of 4.756 mg/min. However, this peak is found to shift towards the lower temperature side for the EB irradiated samples. For the DTG curve of $S1_{(5),}$ a strong peak is found at 74.77^oC with a weight loss of 0.227 mg/min. Fig.4.1 shows that the DTG curve dependence on the EB irradiation dose. The nature of DTA curve is almost identical in the irradiated samples. A sharp exothermic peak is observed at 249^oC in the DTA curve of cerium oxide bare sample. But, the peak is not observed in DTA curves of the EB irradiated samples.

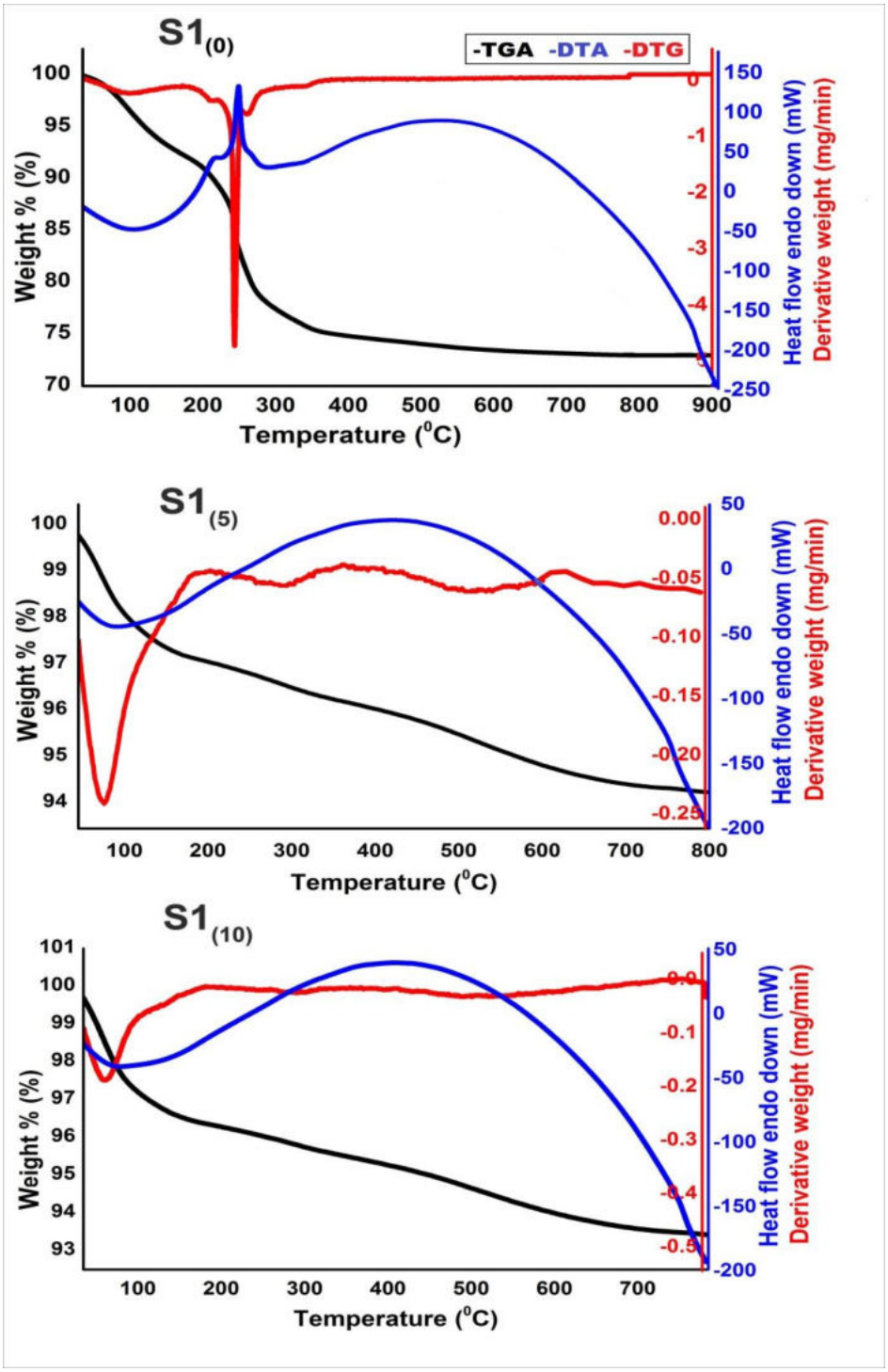

Fig.4.1 TGA/DTA/DTG curves of bare and EB irradiated CeO_2 nanoparticles

4.2.2 Structural characterization

The structural analyses of bare and EB irradiated nanoceria samples are carried out by following the procedure described in *Section 2.4.2.*

4.2.2.1 Powder XRD analysis

The powder X-ray diffraction patterns of the bare and EB irradiated samples are collected by reflection mode with Cu-K_α radiation (λ= 1.5406 Å) using Bruker D8 Advance X-ray diffractometer (step size = 0.020^o, step time = 32.8 s and 40 kV, 35mA). The XRD spectra of bare and EB irradiated samples are given in Fig.4.2. All peaks in the patterns could be indexed on the basis of a face-centered cubic fluorite structure for CeO_2 in the JCPDS No:81–0792, space group *Fm3m (225)* [2]. It is observed that both bare and electron irradiated samples have identical diffraction peaks. The average crystallite sizes calculated using Scherrer equation [3], for samples $S1_{(0)}$, $S1_{(5)}$ and $S1_{(10)}$ are 7.3, 5 and 6.4 nm, respectively. When CeO_2 sample is subjected to an electron dose of 5 kGy, crystallite size decreases from 7.3 to 5 nm. However, when the electron dose is increased to 10 kGy, the crystallite size increases from 5 to 6.4 nm. This increase in size of the of sample ($S1_{(10)}$) is due to electron energy induced coalescence of the grains [4]. These results indicate that the crystallite size of CeO_2 nanoparticles can be tuned by suitable electron dose.

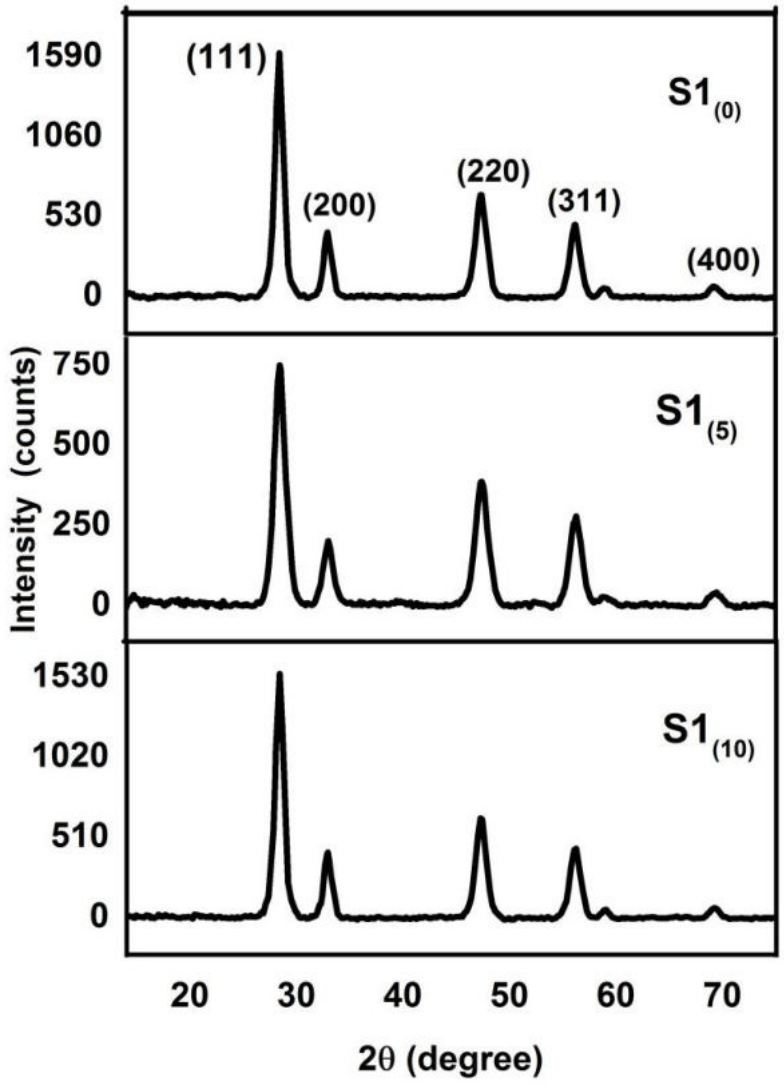

Fig.4.2 XRD patterns of bare and EB irradiated CeO_2 nanoparticles

It can be seen from Fig. 4.2 that the intensity of XRD peaks for electron irradiated samples are decreased. But, FWHM of the electron irradiated samples are found increased. The decrease in intensity of the peak and increase of FWHM indicate the grain size reduction due to EB irradiation [2]. EB irradiated samples also show a slight shift in their peak positions (2θ) towards lower angle side, which in turn results in an

increase of lattice spacing. The increase in lattice spacing is due to the residual stretching strain induced by irradiation. It is reported that due to residual stress, strain is generated in the sample by stretching or compressing the bonds between atoms [5]. The lattice constant *a* and unit cell volume ($V=a^3$) for bare and EB irradiated CeO_2 nanoparticles samples are compared in Table 4.1. W-H plots [6] of EB irradiated nanophase cerium oxide samples are shown in Fig. 4.3. The average particle size and micro-strain are estimated using W-H method as described in *Section 2.4.2.1*. It can be observed that the crystallite size calculated from Scherrer equation agree with that estimated from Williamson–Hall plot. The dislocation density (δ) calculated for the sample $S1_{(0)}$, $S1_{(5)}$ and $S1_{(10)}$ are 0.0188, 0.04 and 0.0244, respectively. Table 4.1 confirms that unit cell volume, lattice spacing, micro-strain and dislocation density values are large in electron beam irradiated samples and are dose dependent. Nanoparticles with a size range of 4-10 nm suffer local distortions on the cubic fluorite structure as a consequence of defects in the oxide lattice [2]. The increase in micro-strain and dislocation density, and broadening of XRD peaks of ceria might occur due to the presenceof O vacancies, structural imperfections and surface effects caused by EB irradiation [2]. In short, electron beam irradiation modifies the structural properties of cerium oxide nanoparticles by changing their crystallite size, lattice spacing, unit cell volume, micro-strain and dislocation density.

Table 4.1 Structural parameters of bare and EB irradiated CeO_2 nanoparticles

Sample	Average crystallite size (nm)		Lattice constant (*a*) Å	d spacing (d_{111}) Å	Volume of unit cell (Å^3)	Micro strain (x10^{-3})	Dislocation density (nm^{-2})
	Scherrer method	W-H method					
S1$_{(0)}$	7.3	8.4	5.403	3.1194	157.73	4.54	0.0188
S1 $_{(5)}$	5	5.7	5.447	3.1453	161.6	6.24	0.04
S1 $_{(10)}$	6.4	7	5.439	3.1406	160.9	5.12	0.0244

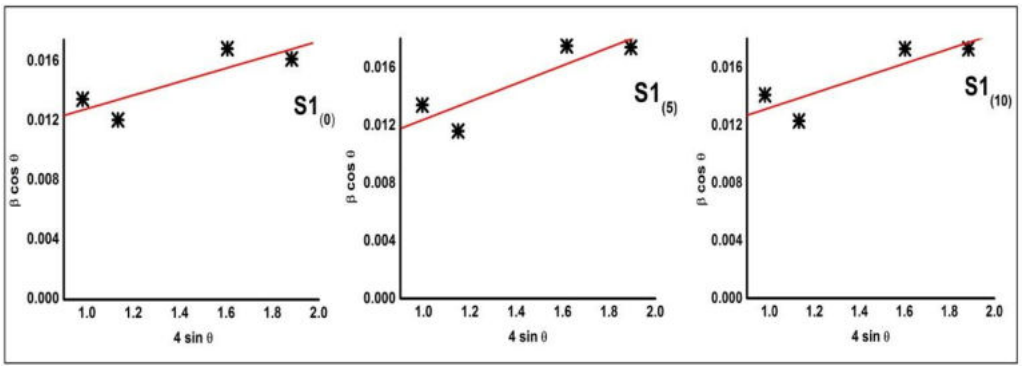

Fig.4.3 W-H plots of bare and EB irradiated CeO_2 nanoparticle

4.2.2.2 TEM analysis

Structural features of bare and EB irradiated nanocrystalline CeO_2 samples are examined by JEOL MODEL JEM-2100 electron microscope operated at 200 kV and the TEM images are displayed in Fig. 4.4. Fig.4.4(a) of all samples shows that particles are not exactly spherical in shape and are agglomerated. From the TEM bright field images (Fig.4.4(a)), it is observed that there is a slight change in morphology of CeO_2 nanoparticles due to electron beam irradiation. Polycrystalline nature of the sample is evident from HRTEM images (Fig.4.4(b)). The SAED patterns of the samples are presented in Fig. 4.4 (c). In the electron irradiated samples, more bright spots are seen, and each spot is formed due to Bragg refection from individual crystallite. The average particle size estimated from TEM images is around 9, 6.5 and 7.2 nm for samples $S1_{(0)}$, $S1_{(5)}$ and $S1_{(10)}$ respectively, which agree with the XRD results. The average size of the CeO_2 particles is found to increase from 6.5 nm for the sample $S1_{(5)}$ to 7.2 nm for the sample $S1_{(10)}$.

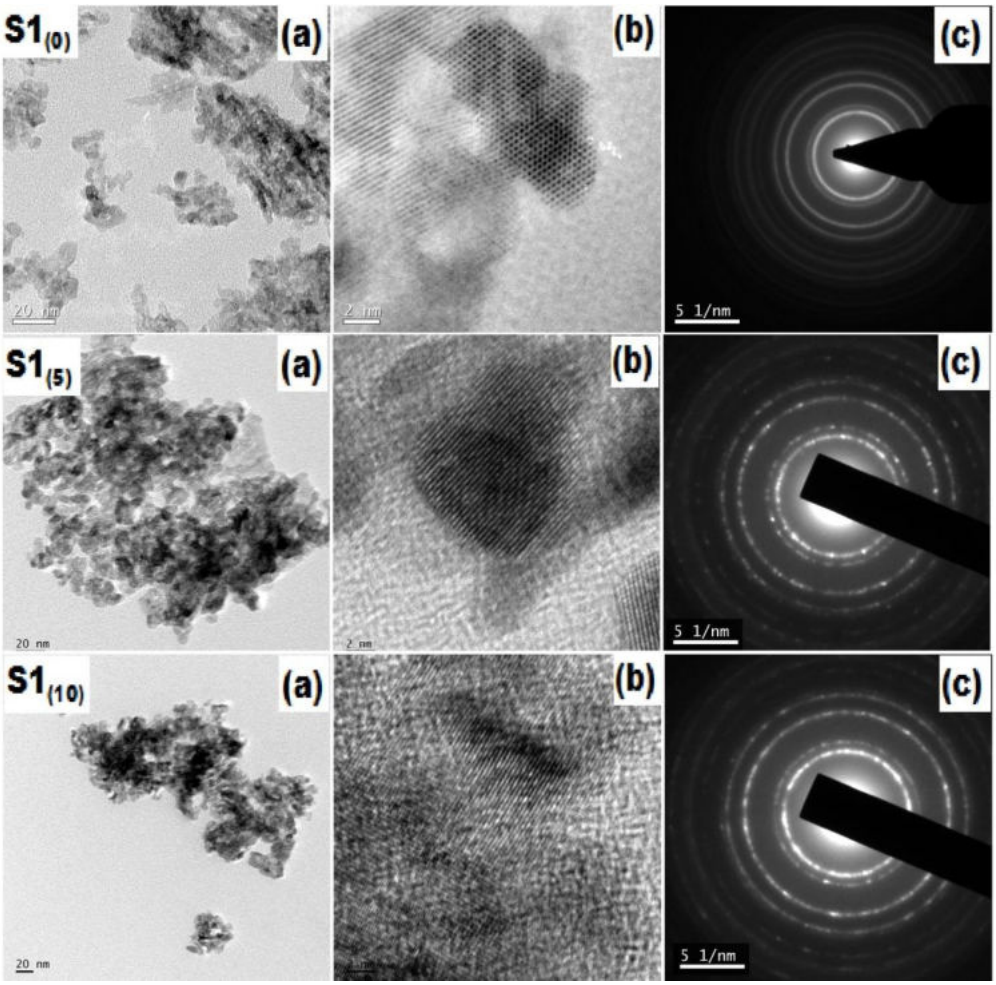

Fig.4.4 TEM images of bare and electron beam irradiated CeO_2 nanoparticles (a) bright field images (b) HRTEM and (c) SAED patterns

4.2.2.3 SEM analysis

The surface morphology of samples are analyzed by a scanning electron microscope JEOL MODEL JSM-6390LV, operating at 20 kV. SEM images of cerium oxide nanoparticle samples $S1_{(0)}$, $S1_{(5)}$ and $S1_{(10)}$ are presented in Fig.4.5. Effect of electron beam irradiation on the morphology of CeO_2 nanoparticle is clearly seen in the figure. It is noticed that, nanostructures are not in uniform size and shape. From

Fig.4.5, it is observed that most of the clusters are broken into small fragments upon electron irradiation.

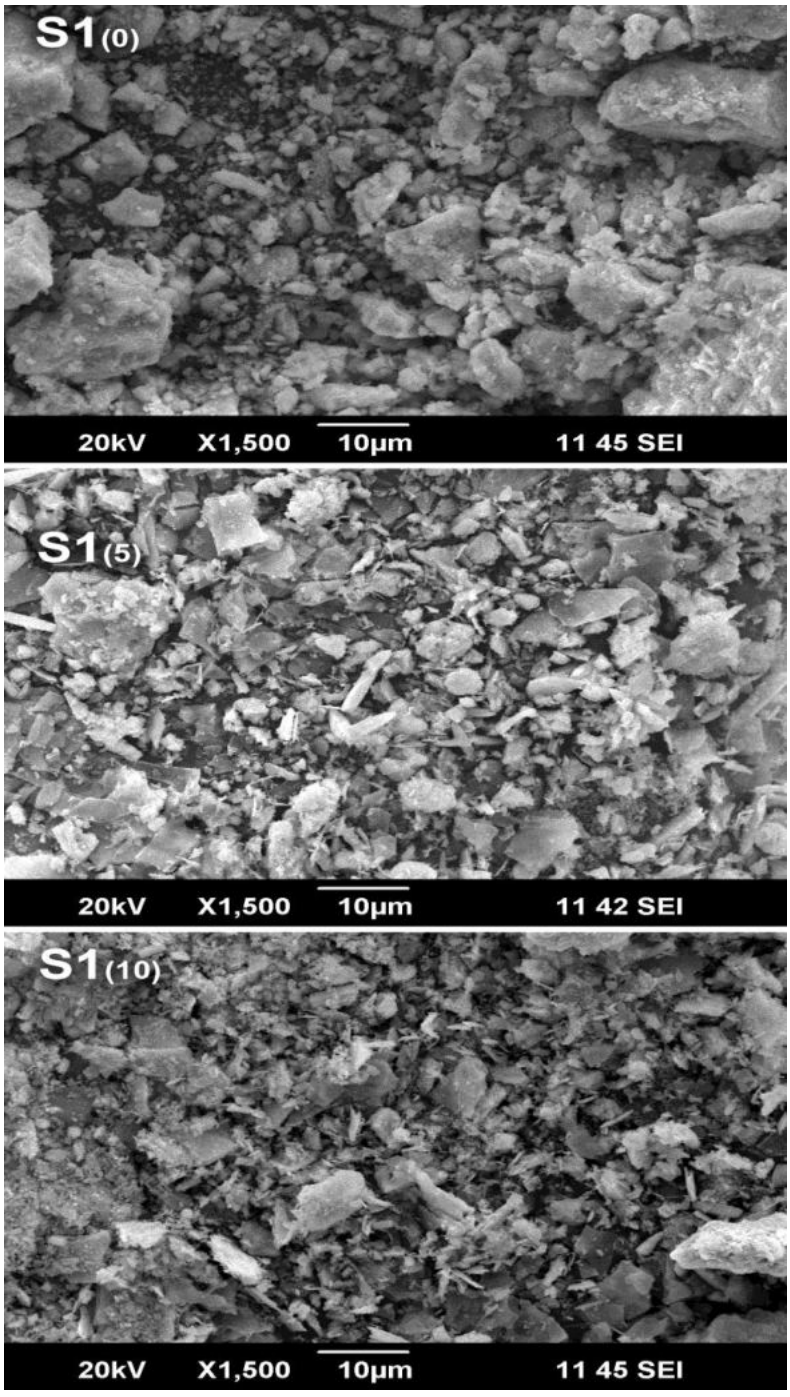

Fig.4.5 SEM images of bare and EB irradiated CeO_2 samples

4.2.2.4 FTIR analysis

FTIR spectra of the sample materials are recorded by FTIR spectrophotometer (Thermo Nicolet, Avatar 370) in the range 4000 to 500 cm^{-1}. The FTIR spectra of the samples $S1_{(0)}$, $S1_{(5)}$ and $S1_{(10)}$ in the transmission mode are presented in Fig.4.6.The spectra show all principal vibrational modes, which are in good agreement with literature [7-11]. The absorption band near 848 cm^{-1} is the typical peak for the Ce-O stretching vibrations [10, 11]. From Figure 4.6, a slight change in the peak position of the irradiated samples is observed, which is due to particle size variation caused by EB irradiation.

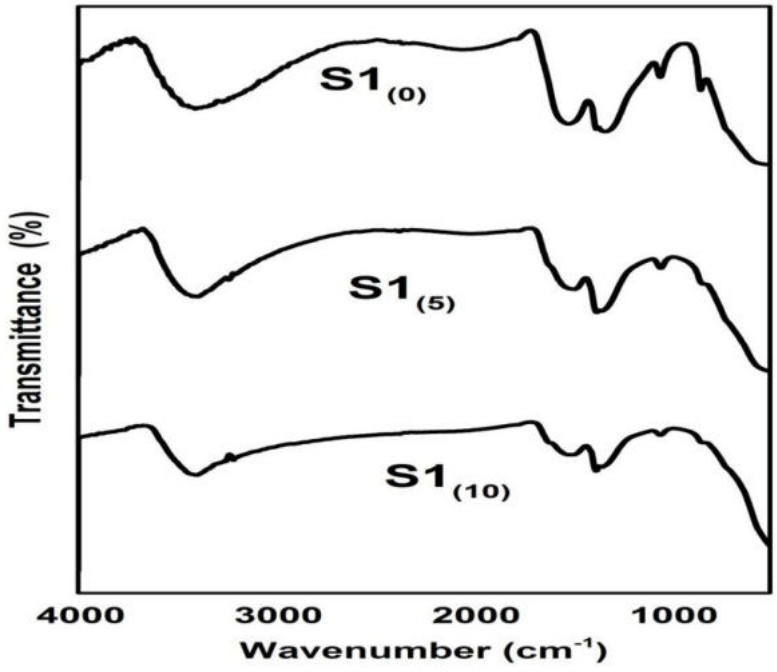

Fig.4.6 FTIR spectra of bare and EB irradiated CeO_2 nanoparticles

4.2.2.5 Raman spectroscopy

Raman spectroscopic studies are capable of detecting small changes in crystal structure and extensively used in the analysis of the irradiation damage [12]. The cubic structure of cerium oxide nanoparticle samples are further confirmed by Raman spectra studies, which are collected at room temperature using Bruker FRA/106/S Raman spectrometer. The spectra are recorded from 50-700 cm^{-1}. Fig.4.7 shows the Raman vibrational modes of bare and EB irradiated CeO_2 samples. Raman active modes of CeO_2 samples $S1_{(0)}$, $S1_{(5)}$ and $S1_{(10)}$ are 462.49, 461 and 461.99 cm-1 respectively, as shown in Table 4.2. This mode is attributed to the fluorite structure, which is due to symmetrical stretching mode O atoms around each cerium ions, and is sensitive to any disorder in the oxygen sub-lattice resulting from thermal, doping or grain size induced non-stoichiometry [13,14]. Fig.4.7 shows that the Raman bands for the EB irradiated samples $S1_{(5)}$ and $S1_{(10)}$ are slightly modified and shifted towards the small wave number side. In addition to this, a decrease in Raman intensity for the irradiated samples is observed. These variations could be due to the decrease in vibrational amplitudes of the nearest neighbor bonds due to particle size variation induced by electron beam irradiation [2]. This evolution of the Raman band can also be attributed to the combined effect of phonon confinement and inhomogeneous strain [15, 16].

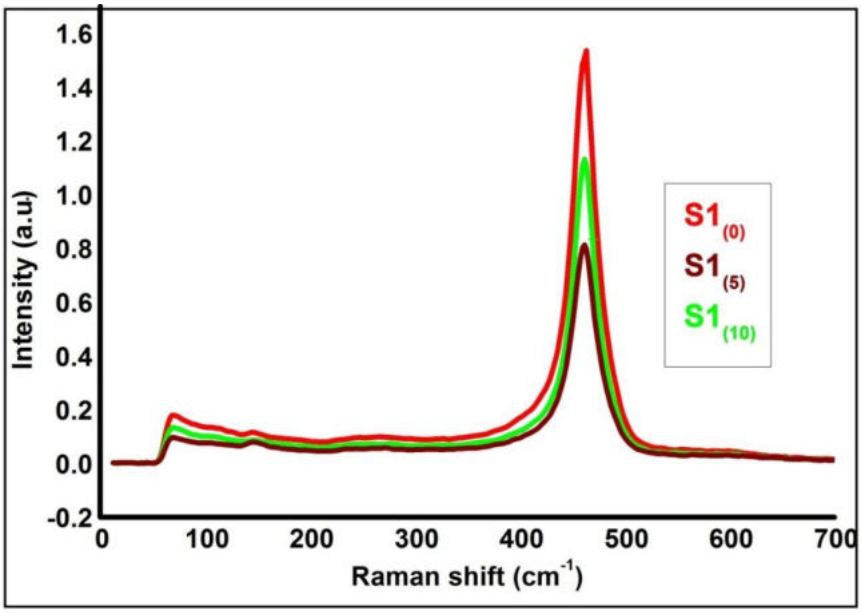

Fig.4.7 Raman spectra of bare and EB irradiated CeO_2 nanoparticles

Table 4.2 Raman modes of bare and EB irradiated CeO_2 nanoparticles

Sample	Raman mode (F_{2g}) cm^{-1}
$S1_{(0)}$	462.49
$S1_{(5)}$	461
$S1_{(10)}$	461.99

4.2.3 Optical properties

UV-Vis absorption and photoluminescence spectra of the bare and EB irradiated CeO_2 nanoparticles are presented in this section. The analysis are carried out by following the procedure as given in *Section 2.4.3.*

4.2.3.1 UV-visible absorption spectroscopy

Absorption spectra of bare and EB irradiated CeO_2 nanoparticles are collected by a double beam UV-Visible spectrophotometer (Shimadzu UV-2600 model). Kubelka Monk transformation is used for measuring absorbance, which is recorded as a function of wavelength as seen in Fig.4.8. All the samples show good absorption below 400 nm, and a broad absorption peak is observed around 243 nm. The absorption of CeO_2 in the UV region originates from the charge-transfer transition between the *O 2p* and *Ce 4f* states in O^{2-} and Ce^{4+} [1]. This absorption is much stronger than the $4f^1–5d^1$ transition from the Ce^{3+} species in the mixed valence CeO_2 system [17]. It can be observed a slight rise in the intensity of absorbance spectra for the electron irradiated samples, which may be due to Ce nucleation and electronic as well as structural defects created during EB irradiation [18].

Direct band gap (E_g) of the samples are determined from Tauc plot by fitting absorption data to direct transition equation [19]. Tauc plot for the samples irradiated with a dose of 0, 5 and 10 kGy are displayed in Fig.4.9. Optical band gap energy values obtained for CeO_2 samples $S1_{(0)}$, $S1_{(5)}$ and $S1_{(10)}$ are 3.42, 3.59 and 3.45 eV respectively. The band gap modification indicates particle size variation due to EB irradiation. The spacing of the electronic levels and the energy band gap is highly dependent on the particle size [20]. Besides, improvement in the intensity of the absorption peak suggests that the irradiation produces sufficient defects [6, 21, 22]. In brief, EB irradiation modifies optical properties of

CeO_2 nanoparticles as a result of changes in their structural parameters due to electron irradiation [23].

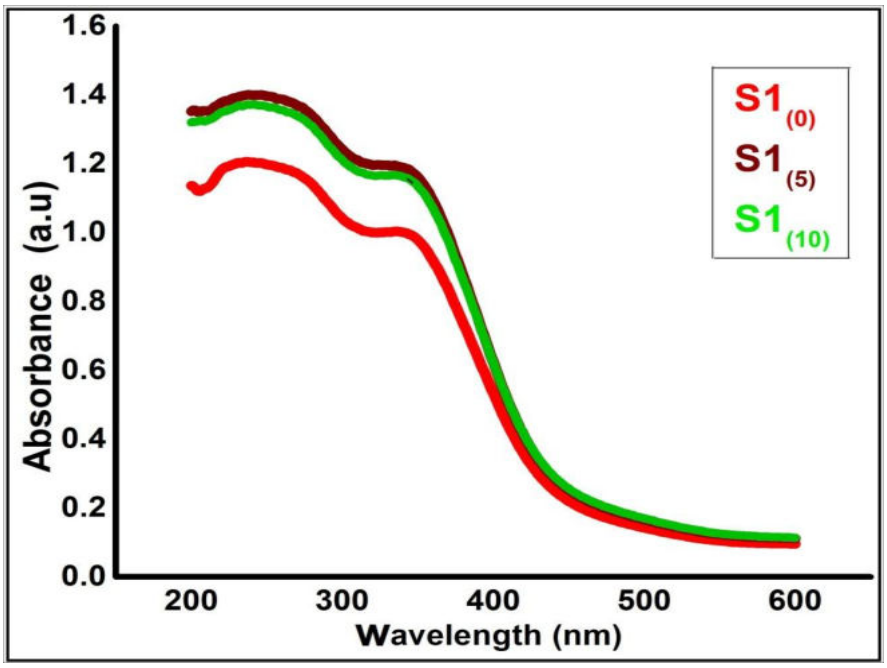

Fig.4.8 Optical absorption spectra of bare and EB irradiated CeO_2 samples

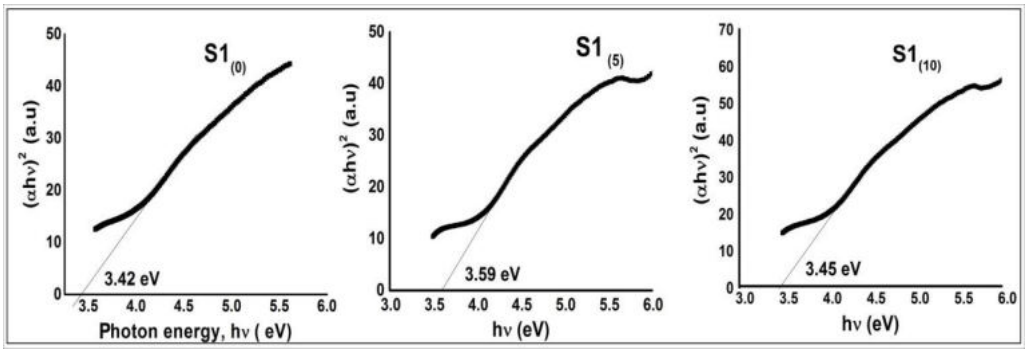

Fig.4.9 Tauc plot of bare and EB irradiated CeO_2 samples

4.2.3.2 Photoluminescence spectroscopy

PL emission spectra of bare and EB irradiated CeO_2 nanoparticle samples are recorded at room temperature using a Fluoromax-3 spectrophotometer. The emission spectra are recorded in the range 350–

600 nm at an excitation wavelength of 330 nm using a slit width of 5 nm. The PL spectra of EB irradiated samples are presented in Fig.4.10. The nature of emission spectra for all the samples is almost the same. Both the pure and irradiated samples of CeO_2 exhibit sharp blue emission band at 448 nm (2.77 eV) and 466 nm (2.66eV). It is also observed a blue green emission at 470 nm (2.64 eV) and 489 nm (2.54 eV). The blue emission is due to the charge transition from *Ce 4f* band to *O 2p* band (valence band) of CeO_2 nanoparticles [24]. The strong emission at 466 nm (2.66 eV) is related to the defects such as dislocations, which is helpful for fast oxygen transportation. The irradiated samples show much larger luminescence intensities relative to pure sample, which may be due to high defect concentration and particle size variation [2]. The increase in PL intensity for the irradiated samples is attributed to the recombination of self-trapped excitons, which is a combined effect of defect centres generated by oxygen vacancies, small particle size and increased absorption over the UV and visible range [22].

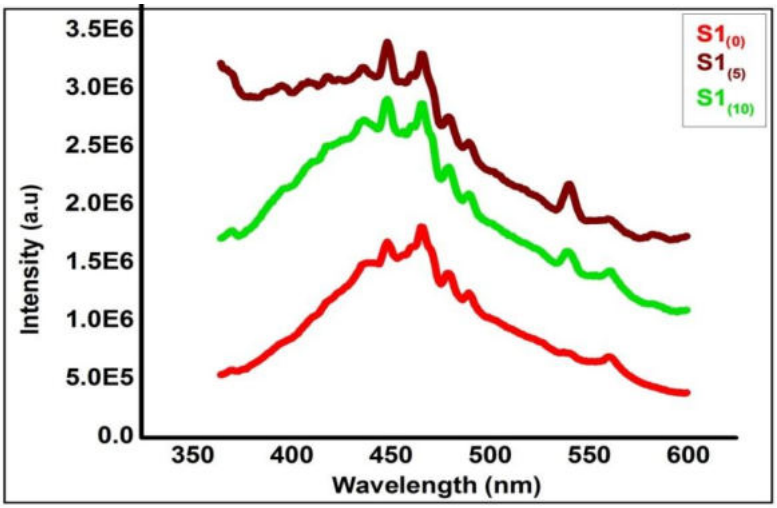

Fig.4.10 PL spectra of bare and EB irradiated CeO_2 samples

It is interesting that crystallite size greatly reduced when the sample is exposed to 5 kGy dose. But, when the electron irradiation dose is increased to 10 kGy, the crystallite size is found to be slightly increased. Hence, number of fluorophores get reduced, which lead to a slight decrease in the PL intensity of $S1_{(10)}$ sample. EB irradiated samples show an additional shoulder peaks at 540 nm (2.29 eV) due to defect generation. The sample irradiated with a dose of 5 kGy shows additional bands at 396, 409 and 418 nm. Peaks at these wavelengths are originated from defect states existing extensively between the Ce 4f state and O 2p valence band [25]. Briefly, the method of electron beam irradiation is an efficient method for creating structural changes which in turn produce stable and high luminescent CeO_2 for various optoelectronic applications [2].

Fig.4.11 exhibits the CIE chromaticity diagram of the bare and EB irradiated samples of CeO_2 nanoparticles. The *x* and *y* chromaticity co-ordinates under the excitation of 330 nm are calculated in CIE XYZ colour space and are given in the Table 4.3. The greenish-blue emission is obtained with CIE coordinates (0.18846, 0.26176) and (0.14563, 0.22959) for the samples $S1_{(0)}$ and $S1_{(5),}$ respectively. The sample $S1_{(10)}$ shows blue-green emission. This result is also consistent with PL spectra of the samples. The results confirm that CeO_2 nanoparticles can be used to construct near ultraviolet (NUV) light excited LEDs.

Table 4.3 Chromaticity co-ordinates of $S1_{(0)}$, $S1_{(5)}$ and $S1_{(10)}$

Sample	$S1_{(0)}$	$S1_{(5)}$	$S1_{(10)}$
x	0.18846	0.14563	0.16053
y	0.26176	0.22959	0.30065

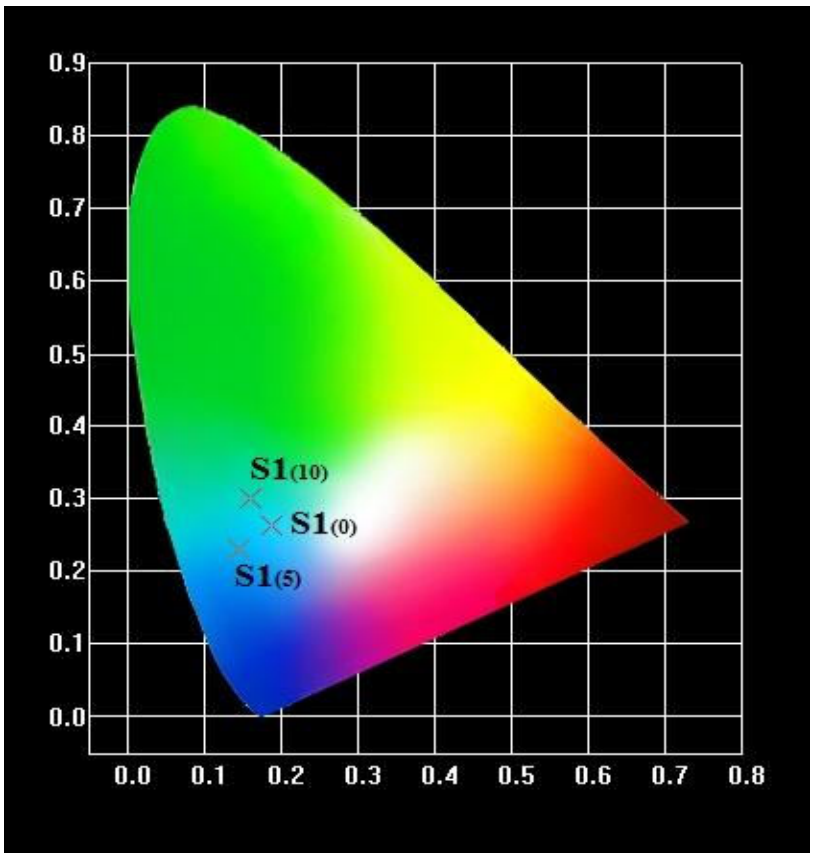

Fig.4.11 Chromaticity diagram of bare and EB irradiated CeO_2 nanoparticle samples

4.2.4 Electrical properties

In order to understand the effect of electron beam irradiation on the electrical properties of CeO_2 samples, beam irradiated powder

samples are consolidated in the form of cylindrical pellets of diameter 13 mm and thickness 1.4 mm. Both the faces of the pellets are coated with air drying silver paste for good electrical contact. Dielectric measurements as a function of frequency in the range of 100 Hz−10 MHz are measured at room temperature (303 K) using Wayne Kerr H-6500B model impedance analyzer.

4.2.4.1 Frequency dependence of dielectric constant

The variation of dielectric constant with frequency at room temperatures for samples $S1_{(0)}$, $S1_{(5)}$ and $S1_{(10)}$ are shown in Fig.4.12. It can be seen that the EB irradiated samples show high dielectric constant at low frequencies, which decreases rapidly as frequency increases and attain a constant value at higher frequencies. The dielectric behavior of cerium oxide nanoparticle as a function of frequency is explained in the *Section 3.3.4.1*. The dielectric constant ε' of sample $S1_{(0)}$ is 66 at 100 Hz, which is changed to 1750 when it is irradiated with a dose of 5 kGy electron beam. But when the dose level is increased to 10 kGy, ε' changes to 481. The modification in ε' indicates grain size variation due to beam irradiation. Upon irradiation, the increase in grain boundary creates more number of defects, which results in the formation of a large number of dipoles that governs its dielectric properties by increasing interfacial polarization [26]. Besides, EB irradiation of suitable dose can create high concentration of defects, free radicals and unsaturated bonds that promote high dielectric constant for the irradiated samples.

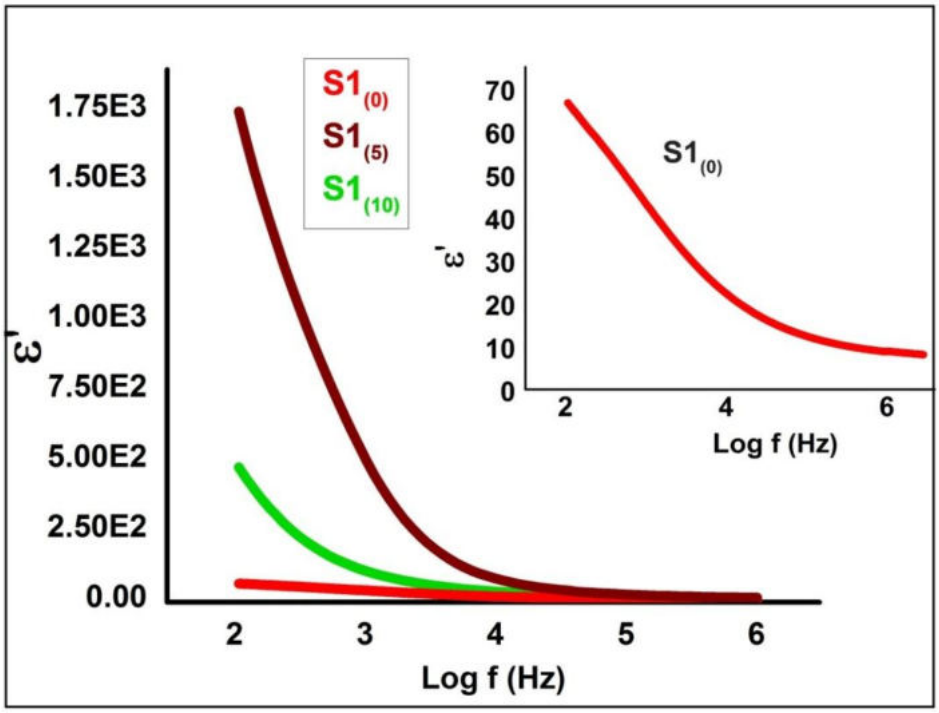

Fig.4.12 Variation of dielectric constant with frequency at room temperature for bare and EB irradiated CeO_2 nanoparticles

\

4.2.4.2 Frequency dependence of loss tangent

The variation of dielectric loss with frequency at room temperature for sample $S1_{(0)}$, $S1_{(5)}$ and $S1_{(10)}$ are presented in Fig.4.1 The electron irradiated samples show high dielectric loss than the bare sample. The room temperature loss tangent value of cerium oxide nanoparticle is 7 at 100 Hz. The value is elevated to 64 when the sample is exposed to 5kGy dose. When the EB dose is increased to 10 KGy, the dielectric loss is decreased to 16. In dielectric materials, generally dielectric loss occurs due to absorption current. In many cases, EB irradiation causes amorphization, which produce disorder in the nanomaterial. As a result, defects and space charge formation in the inter

phase layers of the material increases. This will produce more absorption current and hence, large dielectric loss.

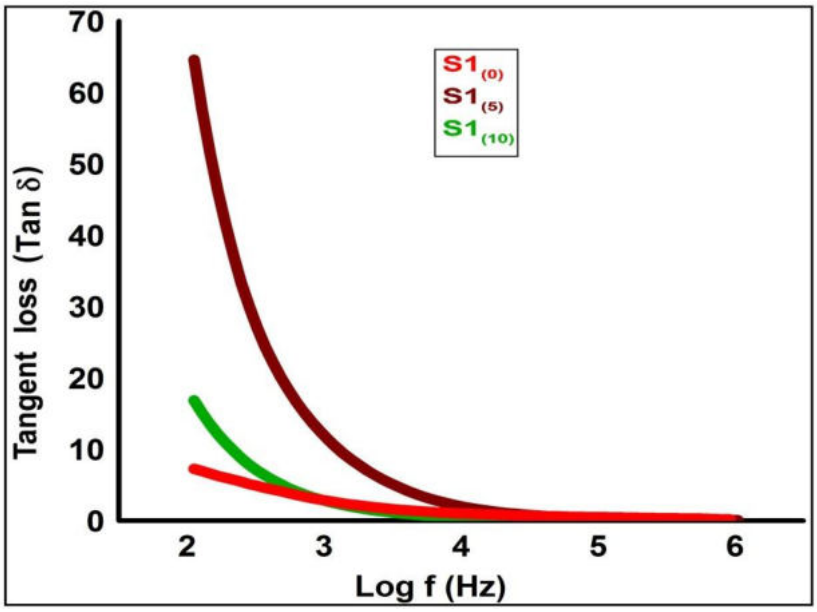

Fig.4.13 Variation of tangent loss with frequency at room temperature for bare and EB irradiated CeO_2 nanoparticles

4.2.4.3 Frequency dependence of AC conductivity

Fig.4.14 shows the frequency dependent AC conductivity of bare and electron irradiated CeO_2 nanoparticles. It can be seen that EB irradiated samples have more AC conductivity than non irradiated sample due to grain size reduction. EB irradiation leads to faster ionic transport in the material, which results in high conductivity. It is observed that AC conductivity of $S1_{(0)}$ at 303 K is changed from 1.02×10^{-4} S/m to 3.5×10^{-4}S/m when it is irradiated with EB of 5 kGy dose. The increase in AC conductivity with frequency (Fig. 4.14) reveals that more free charges are involved in the hopping process through the defective sites [26].

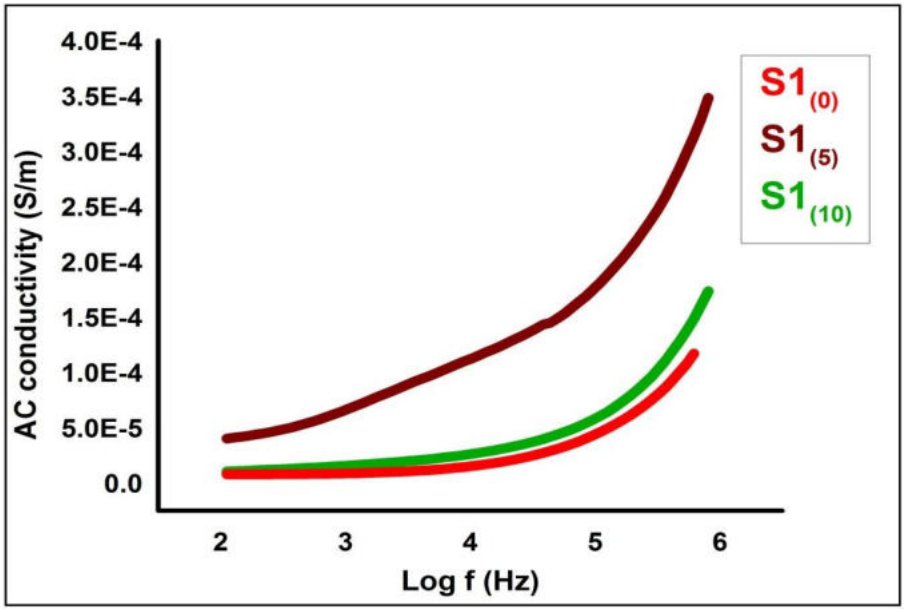

Fig.4.14 Variation of AC conductivity with frequency at room temperature for bare and EB irradiated CeO_2 nanoparticles

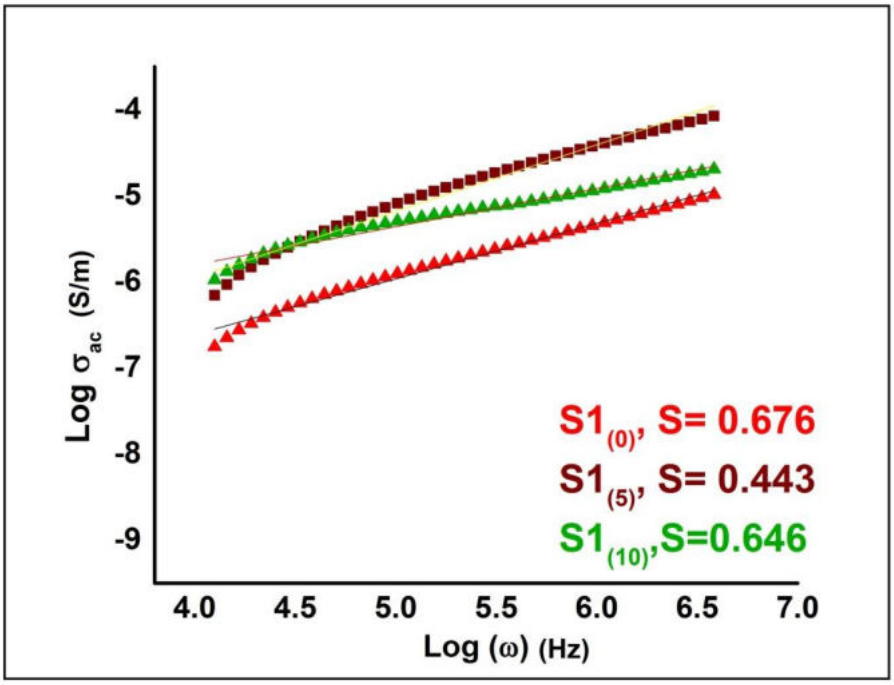

Fig.4.15 *Log(σ_{ac})* versus *log(ω)* plots of bare and EB irradiated CeO_2 samples

Fig.4.15 shows the $log(\sigma_{ac})$ versus $log(\omega)$ plots of bare and EB irradiated CeO_2 nanoparticles. The frequency exponent *S* is determined from the slope of $log(\sigma_{ac})$ versus $log(\omega)$ plot . The obtained S values are 0.676, 0.443 and 0.646 for the samples $S1_{(0)}$, $S1_{(5)}$ and $S1_{(10)}$ respectively. The value of *S* that lies between 0 and 1, which indicates that the AC conduction follows frequency dependent hopping mechanism [27,28].

4.3 Conclusions

- The effect of 8 MeV electron beam irradiation on the properties of cerium oxide nanoparticles are investigated.
- A comparative study of thermal, structural, optical and electrical properties of bare and EB irradiated (5kGy and 10kGy) samples is conducted.
- The EB irradiation of CeO_2 nanoparticles confirms changes in physical properties such as, structural modifications, improvements in optical and PL spectra and advances in dielectric properties.
- XRD results show that the electron beam irradiated samples exhibit a decrease in crystallite size and the effect is more prominent in 5 kGy dose. It affects the structural properties of cerium oxide nanoparticles by introducing defects.
- Electron beam irradiation modifies the structural properties of cerium oxide nanoparticles by changing their crystallite size, lattice spacing, unit cell volume, and micro-strain and dislocation density.
- FTIR and Raman bands are modified upon electron beam irradiation.

- The optical band gap energy values obtained for CeO_2 samples $S1_{(0)}$, $S1_{(5)}$ and $S1_{(10)}$ are 3.42, 3.59 and 3.45 eV, respectively. The band gap modification attributes particle size variation due to EB irradiation. Improvement in the intensity of the absorption peak suggests that irradiation produces sufficient defects. In short, EB irradiation significantly affects particle size and hence the absorption properties.
- EB irradiated samples exhibit large PL intensities due to particle size variation and large concentration of defects.
- EB irradiation produces high dielectric constant, dielectric loss and AC conductivity for cerium oxide nanoparticles. The dielectric constant of nanoceria is changed from 66 to 1750 at 100 Hz, when it is irradiated with a dose of 5 kGy electron beam. EB irradiation results large absorption current, which produce increase in dielectric loss. Besides, EB irradiation leads to faster ionic transport in the material, that results in high AC conductivity.
- The present investigation confirms particle size reduction and structural modifications of CeO_2 nanocrystals, which are evidenced by XRD, TEM, SEM, FTIR, Raman, UV-visible absorption, PL and electrical studies.
- Based on the systematic observations, it is concluded that electron beam irradiation is efficient method for modifying the physical properties of cerium oxide nanoparticles for potential applications.

References

[1] K. K. Babitha, A. Sreedevi, K. P. Priyanka, Boby Sabu and Thomas Varghese , Indian J. Pure Appl. Phys., 53(2015) 596-603.

[2] K. K. Babitha, K. P. Priyanka, A. Sreedevi, S. Ganesh and Thomas Varghese, Mater. Charact., 98 (2014) 222–227.

[3] B. D. Cullity, Elements of X-Ray Diffraction, Addison-Wesley, MA (1967).

[4] N. Choudhury, F. Singh and B. K. Sarma, Indian J. Pure Appl. Phys., 50 (2012) 325-328.

[5] S. Kumar, K. Asokan, R. K. Singh, S. Chatterjee, D. Kanjilal, and A. K. Ghosh, J Appl. Phys., 114 (16)(2013)164321.

[6] G. K. Williamson and W. H. Hall, Acta. Metall., 1(1953) 22..

[7] J. Gao, F. Guan, Y. Ma, W. Yang, J. Kang, H. Deng and Y. Qi, Rare Metals, 20 (2001) 217

[8] C. Ho, J. C. Yu, T. Kwang, A. C. Mark and S. Lai, Chem. Mater.,17(17) (2006) 4514.

[9] S. B. Khan, M. Faisal, M. M. Rahman and A. Jamal, Sci. Tot. Environ., 409 (2011) 2987.

[10] F. Niu, D. Zhang, L. Shi, X. He, H. Li, H. Mai and T. Yan T, Mater. Lett., 63 (2009) 2132.

[11] M. Palard, J. Balencie, A. Maguer and J. F. Hochepied, Mater. Chem. Phys., 20 (2010) 79.

[12] R. Brunetto, G. A. Baratta, G. Strazzulla, J. Appl. Phys. 96 (2004)380.

[13] I. Kosacki, V. Petrovsky, H.U. Anderson, P. Colomban, J. Am. Ceram. Soc., 85 (2002) 2646.

[14] F. Marabelli and P. Wachter, Phys. Rev. *B,* 36 (1987) 1238.

[15] J. E. Spanier, R. D. Robinson, F. Zhang, S.W. Chan, I. P. Herman, Phys. Rev., B 64 (2001) 245407.

[16] Z. Dohcevic-Mitrovic, M. Grujic-Brojcin, M. Scepanovic, Z.V. Popovic, Solid State Commun., 137 (2006) 387.

[17] S. Phoka, P. Laokul, E. Swatsitang, V. Promarak, S. Seraphin, S. Maensiri, Mater. Chem.Phys., 115 (1) (2009) 423.

[18] J. Andres, L. Gracia, P. Gonzalez- Navarrete, V. M. Longo, W. A. Jr, D. P. Volanti, M. M. Ferrer, P. S. Lemos, F. A. L. Porta, A. C. Hernandes, E. Longo, Sci.Rep.,5 (2014)5391.

[19] J. Tauc, Amorphous and Liquid Semiconductors, 1 ed. Plenum Press, New York (1974).

[20] E. Ziegler, A. Heinrich, A. Oppermann, G. Stover, Phys. Status Solidi, A 66 (1981) 635.

[21] Yeming Xua, Liang Shi, Xitian Zhanga, KawaiWong, Quan Li, Micron 42 (2011) 290.

[22] M. A. P. Almeida, L. S. Cavalcante, M. S. Li, J. A. Varela, E. Longo, J. Inorg. Organomet. Polym. Mater., 22 (1) (2012) 264.

[23] N. Aloysius Sabu, K. P. Priyanka, Sanjeev Ganesh and Thomas Varghese, Radiat. Phys. Chem., 123(2016)1–5.

[24] Sumalin Phokha, Supree Pinitsoontron, Prae Chirawatkul, Yingyot Poo-arporn, M.Santi, Nanoscale Res. Lett., 7 (2012) 425.

[25] A. H. Morhed, M. E. Moussa, S. M. Bedair, R. Leonard, S.X. Liu, N. A. El-Masry, Appl.Phys. Lett., 75 (1997) 2389.

[26] S. Raghu, K. Archana, C. Sharanappa, S. Ganesh, H. Deven drappa, J.Radiat. Res. Appl. Sci., 9 (2016)117-124.

[27] B. M. Greenhoe, M. K. Hassan, J. S. Wiggins, K. A. Mauritz, J. Polym. Scie. Part B: Polymer Physics, (2016); doi: 10.1002/polb.24121.

[28] S. R. Elliott, Adv. Phys., 36 (1987)135.

..... ☙❋❧ .....

Chapter 5

STUDIES ON THE THERMAL, STRUCTURAL, OPTICAL AND ELECTRICAL PROPERTIES OF CeO_2/CoPc NANOCOMPOSITE

5.1 Introduction

Metal Phthalocyanines (M-Pc) are important functional materials in many fields due to their efficient electron transfer abilities. The combination of M-Pc, an organic semiconducting material, with cerium oxide, an inorganic semiconducting material can offer novel properties for potential applications because of the potential of combining distinct physical properties. The organic materials exhibit high thermal properties, distinctive chemical properties, nontoxicity, semi conductivity and interesting optical properties [1]. Inorganic metal oxide nanoparticles provide the potential for high carrier mobility, band gap tunability, thermal and mechanical stability and a range of magnetic and dielectric properties [2]. This chapter deals with the synthesis of cerium oxide/cobalt phthalocyanine nanocomposite. To date, no studies have been reported on the structural, optical and electrical properties of CeO_2/CoPc nanocomposite. Impact of the presence of cobalt

phthalocyanine on the properties of nanoceria is also discussed in this chapter.

5.2 Synthesis of CeO_2/CoPc nanocomposite

The CeO_2/CoPc composite is synthesized by solvent evaporation method. 1 wt% of CoPc (wt% is the mass ratio of CoPc to CeO_2) is dissolved in a solvent mixture containing 50% dimethyl sulphoxide, 30% dimethyl formamide and 20% ethanol at 60°C. Required amount of the synthesized CeO_2 (S_1) [3] is slowly added to this mixture solution under constant stirring and heating, resulting in a suspension with homogeneous appearance. After complete solvent evaporation, the composite is dried at 100°C in a hot air oven for 15–20 h to get the sample in powder form. The synthesized CeO_2 nanoparticles and CeO_2/CoPc nanocomposite samples are denoted as S1 and C1, respectively. Fig.5.1 represents the scheme of preparation of CeO_2/CoPc nanocomposite.

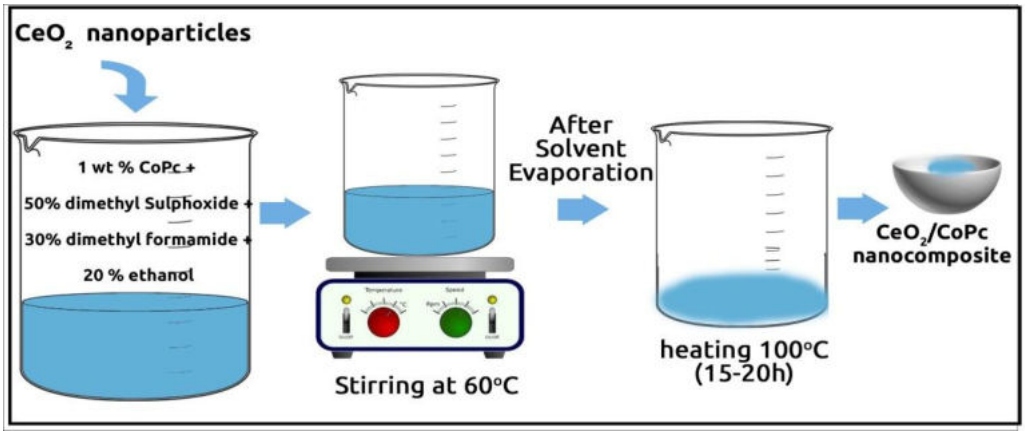

Fig.5.1 Scheme of preparation of CeO_2/CoPc nanocomposite

5.3 Results and discussion

5.3.1 Thermal analysis

Thermogravimetric and differential thermal analysis of the bare and composite samples are carried out using Perkin Elmer STA 6000. TGA/DTA/DTG curves of CeO_2 nanoparticles and CeO_2/CoPc nanocomposite samples are displayed in Fig.5.2. Thermal analysis of the bare CeO_2 sample has been described in *Section 3.3.1*. TGA curves for samples C1 shows a small weight loss from room temperature to 700^{o}C. Weight loss from room temperature to 400^{o}C is due to residual water evaporation. The decomposition of CoPc pyrolyzed between 500 and 1000^{o}C [4]. However, from 400 to 600^{o}C, the weight loss is due to partial decomposition of macrocyclic structure, where low weight atoms (H and part of N) are eliminated from CeO_2/CoPc [5]. The DTG curve of sample C1 shows a strong peak at 68^{o}C. The weight loss at this region is 0.024 mg/min, which is due to the combustion of organic residues produced during the crystallization of residual amorphous phase. A small increase in weight after 600^{o}C is representing pure phase formation. The sharp exothermic peak at 249^{o}C (DTA) of cerium oxide bare sample is not observed in nanocomposite sample. Moreover, the TGA/DTA/DTG studies show that S1 and C1 are thermally stable in the range 100–700^{o}C.

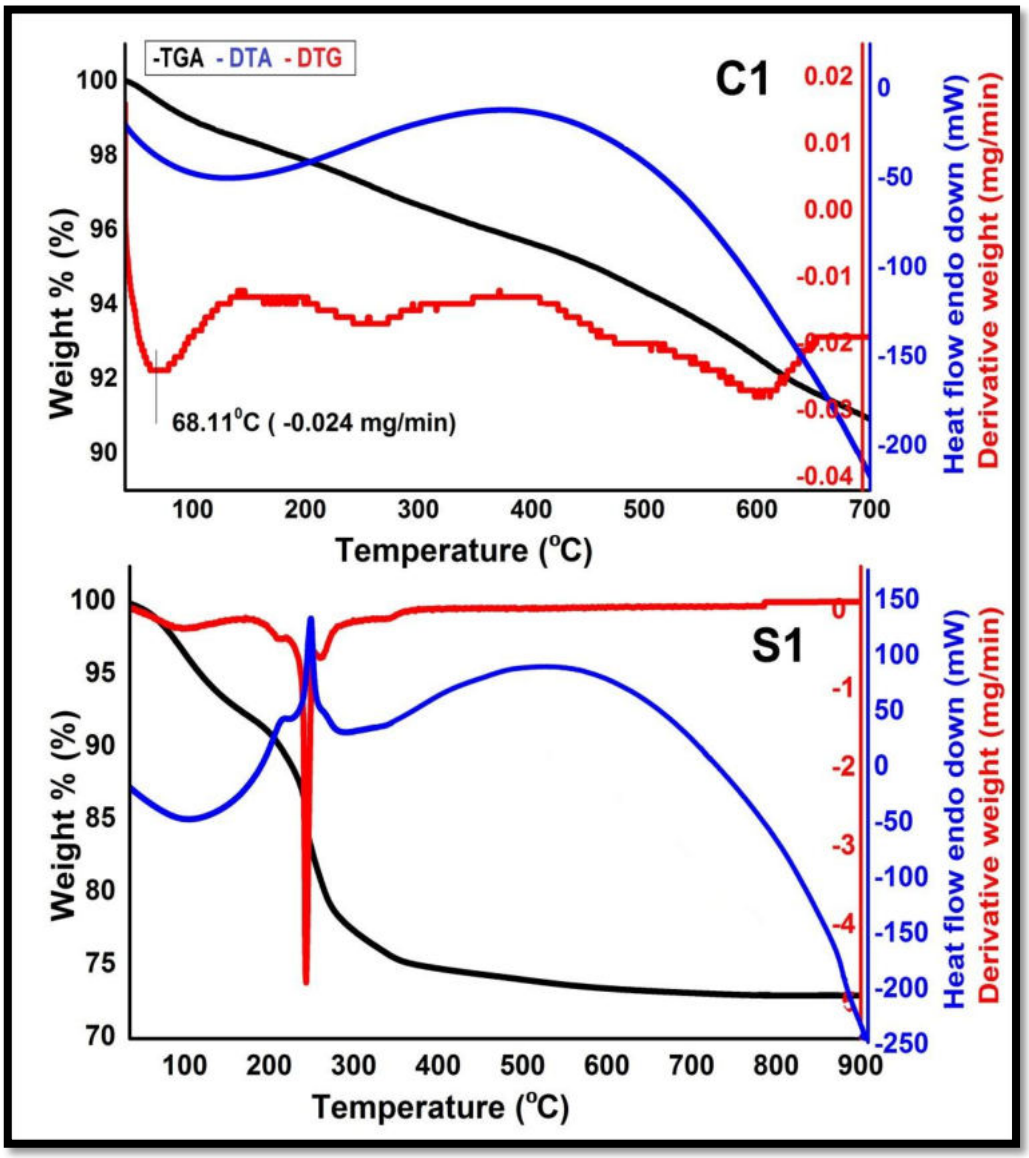

Fig.5.2 TGA/DTA/DTG curves of CeO_2 nanoparticle and CeO_2/CoPc nanocomposite

5.3.2 Structural characterization

The structural characterization of the synthesized nanocomposite sample is carried out by following the procedure described in *Section 2.4.2.*

5.3.2.1 Powder XRD analysis

The structural properties of the synthesized nanocomposite is studied by XRD using Bruker D8 advance X-ray diffractometer in reflection mode (λ= 1.5406 Å, step size = 0.020°, dwell time 65.6 s, 40 kV, and 35 mA) with Cu-Kα radiation in 2θ range from 10 to 80°. Fig. 5.3 shows the XRD spectrum of CeO_2 nanoparticles (S1) and CeO_2/CoPc nanocomposite samples (C1). The diffractogram of C1 reveals that the materials formed are nanocrystalline and shows good crystallinity. All peaks present in the diffraction pattern of C1 represents the pure cubic fluorite structure of CeO_2 (space group: *Fm3m*) with lattice constant a = 5.411 Å, which is in agreement with the JCPDS file No. 75-0076 for CeO_2. It is noticed that there is no change in the diffraction pattern of nanophase CeO_2 with the addition of CoPc. This may be due to the lower loading of CoPc [6]. However, the intensity of peaks are relatively higher in the nanocomposite sample. Average crystallite size estimated by Scherrer equation for the samples S1 and C1 are 7.3 and 7.72 nm respectively [7]. W-H plots of CeO_2 nanoparticles and nanocomposite samples S1 and C1 are shown in Fig. 5.4. Table 5.1 compares the structural parameters of CeO_2/CoPc nanocomposite and CeO_2 nanoparticles. Average particle size calculated from W–H analysis are 8.4 and 9 nm respectively for CeO_2 nanoparticles and CeO_2/CoPc nanocomposite [8]. These values are almost consistent with those obtained from Scherrer equation. It can be seen from Table 5.1 that the

crystallite size, *d* spacing and unit cell volume for the CeO_2 are slightly modified with the addition of phthalocyanine. However, the micro-strain and dislocation density values are slightly reduced in the nanocomposite, which indicates the successful incorporation of CoPc in CeO_2.

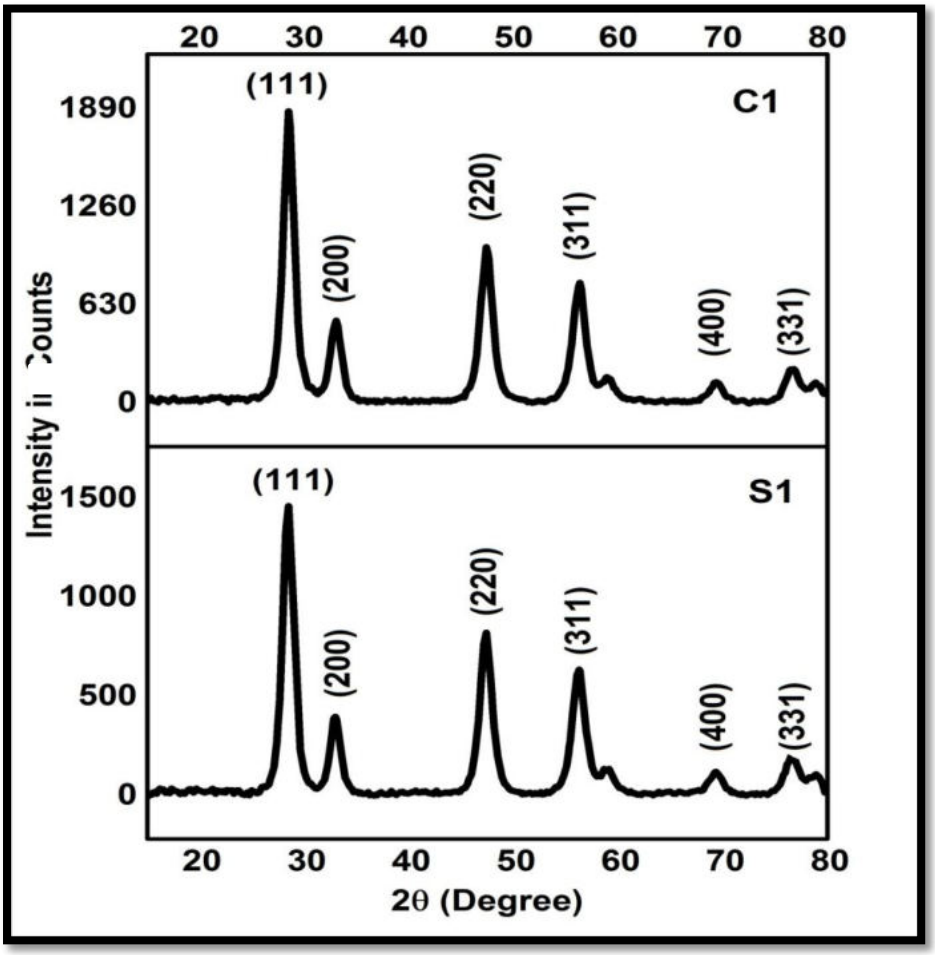

Fig. 5.3 XRD patterns of CeO_2 (S1) and CeO_2/CoPc (C1)

Table 5.1 Structural parameters of CeO_2 and CeO_2/CoPc

Sample	Average particle size (nm)		Lattice constant (*a*) Å	*d* spacing (d_{111}) (Å)	Volume of unit cell ($Å^3$)	Micro strain ($x10^{-3}$)	Dislocation density (nm^{-2})
	Scherrer method	W-H method					
S1	7.3	8.4	5.403	3.1194	157.73	4.54	0.0188
C1	7.72	9	5.410	3.124	158	4	0.0168

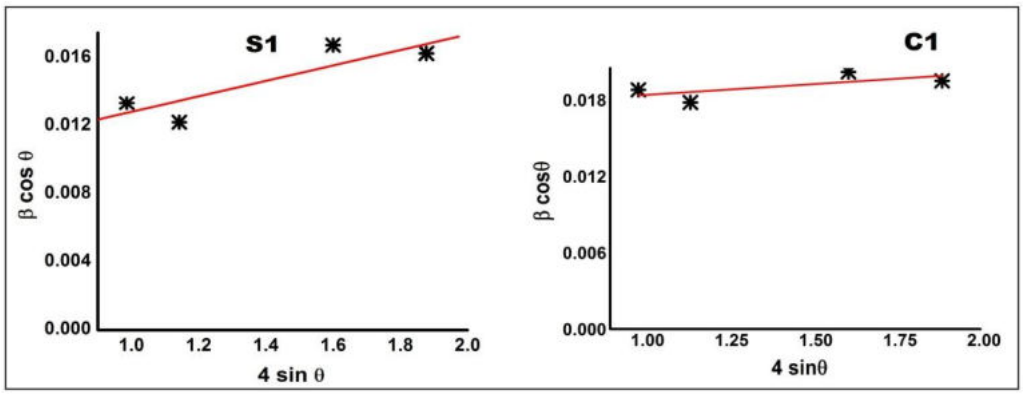

Fig.5.4 W-H plots of CeO_2 nanoparticles and CeO_2/CoPc nanocomposite

5.3.2.2 TEM analysis

TEM images of nanocrystalline CeO_2/CoPc samples are taken from a JEOL/JEM 2100 (Source: LaB6 and voltage: 200 kV) and are shown in Fig. 5.5. The TEM images of CeO_2 nanoparticle (S1) has been discussed in *Section 3.3.2.2.* The bright field images demonstrate (Fig.5.5(a)) that the particles are almost spherical in shape. The particle size of C1 obtained from TEM images ranges from 6 to 9 nm which are in agreement with the XRD results. HRTEM image indicates the polycrystalline nature of C1. The appearance of strong diffraction spots (SAED) rather than diffraction rings confirms the crystalline nature of the nanocomposite.

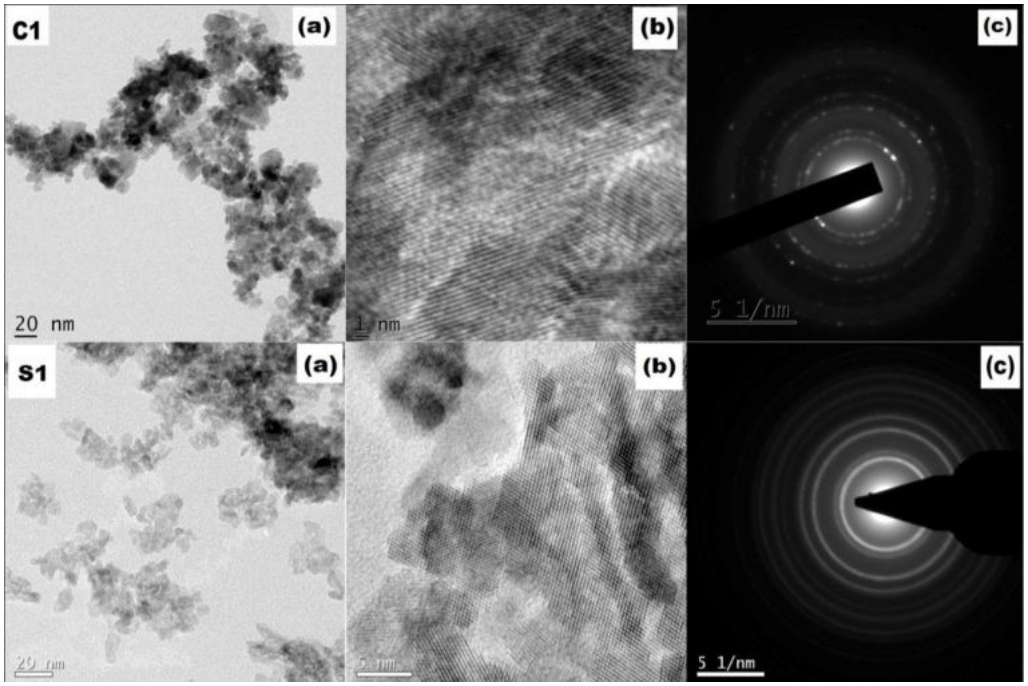

Fig.5.5 TEM images of CeO_2 nanoparticles and CeO_2/CoPc nano composite: (a) Bright field images, (b) HRTEM and (c) SAED patterns

5.3.2.3 SEM and EDX analysis

The surface morphology of samples are analyzed by a scanning electron microscope JEOL MODEL JSM-6390LV, operating at 20 kV. SEM photographs of CeO_2 nanoparticle and CeO_2/CoPc nanocomposite samples are presented in Fig.5.6. It can be seen that particles are agglomerated and are not in uniform size and shape. The photograph of the sample contains irregular crystallized nanoparticle clusters.

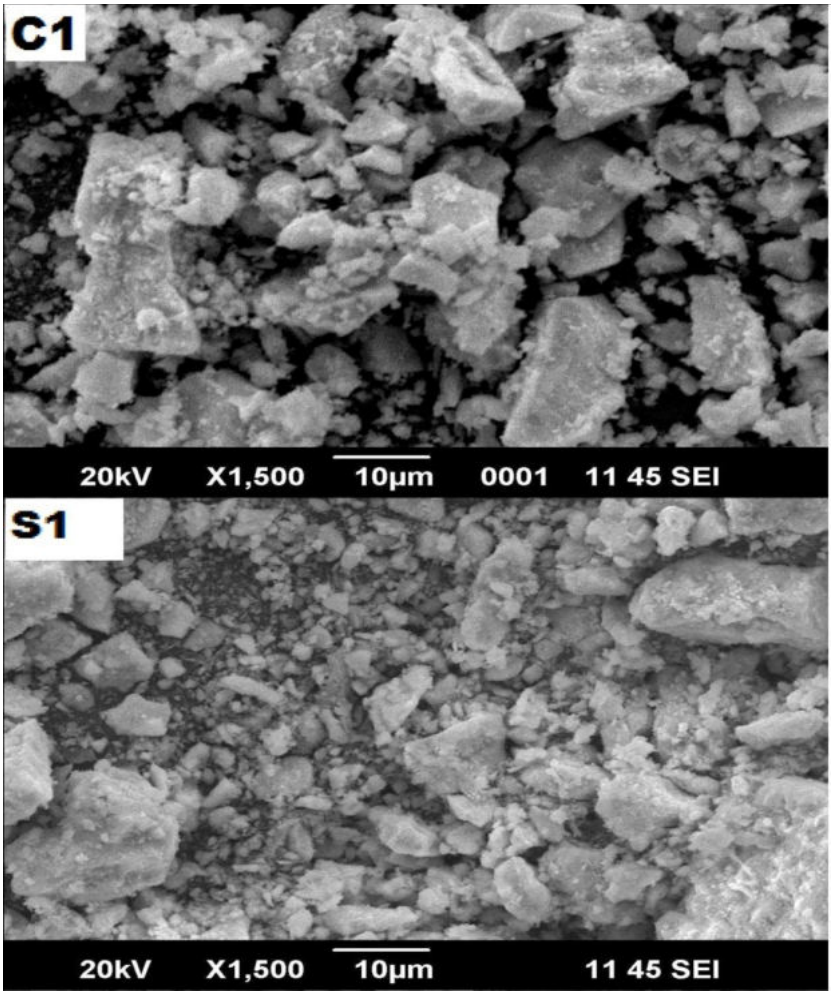

Fig.5.6 SEM images of CeO_2 nanoparticles and CeO_2/CoPc nanocomposite

For recording the EDX pattern, JEOL model JED-2300 with Bruker X flash 6/10 EDS detectors are used. Fig.5.7 shows the EDX analysis results of the composite C1. It shows that the prepared nanocomposite contains Ce, Co, O, C and N. Thus, the EDX study confirms the formation of CeO_2/CoPc nanocomposite. The mass and atom percentages of the sample are also presented in table 5.2.

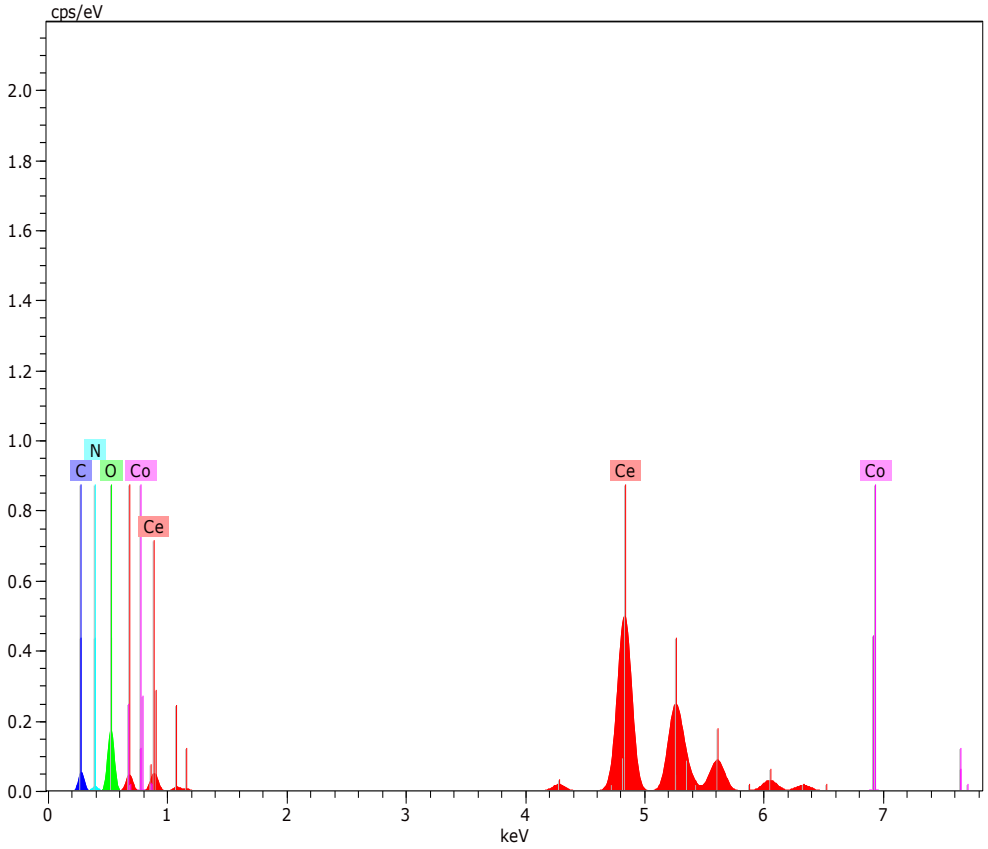

Fig.5.7 EDX pattern of CeO_2/CoPc nanocomposite

Table 5.2 EDX data of CeO_2/CoPc nanocomposite

Element	AN	Series	Nor. Wt.%	Atom wt.%
Ce	58	L	60.05	13.31
O	8	K	21.04	40.86
C	6	K	11.09	28.67
Co	27	K	7.71	17.09
N	7	K	0.12	0.06
		Total	100	100

5.3.2.4 FTIR analysis

The FTIR spectra of CeO_2 and CeO_2/CoPc nanocomposite samples are recorded by Thermo Nicolet, Avatar 370 and presented in Fig. 5.8. The spectra have several significant absorption bands recorded in the range of 4000–500 cm^{-1}. The absorption band at 848 cm^{-1} is observed in both S1 and C1, which is due to metal-O bond. This band produced by CeO_2, indicates the Ce-O stretching vibration [9, 10]. The commonly used bands for orientation studies in phthalocyanines are 733 cm^{-1} (C–H out-of plane deformation) and 1334 cm^{-1} (C=C in-plane stretching) [11,12]. The appearance of a band at 724 cm^{-1} indicates the presence of CoPc-α phase. This study confirms the successful attachment of CoPc to CeO_2. FTIR bands for CeO_2/CoPc nanocomposite sample is listed in Table 5.3, along with literature values of CoPc.

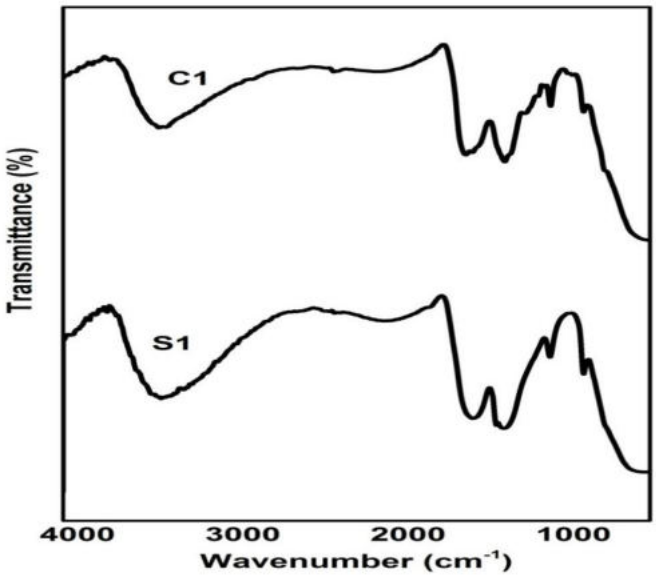

Fig. 5.8 FTIR spectra of CeO_2 nanoparticles and CeO_2/CoPc nanocomposite

Table 5.3 FTIR band assignments of CeO_2/CoPc nanocomposite

Sample C1	CoPc [10]	Band assignment
522	-	Ce-O stretching
724	721	C-H out-of-plane deformation
851	-	metal-O bond
918	911	Metal ligand vibration
1051	-	C-H in plane deformation
1090	1087	C-H in plane deformation
1127	1117	C-H in plane bending
1329	1334	C= C in- plane stretching

5.3.2.5 Raman spectroscopy

Raman studies of the CeO_2 and CeO_2/CoPc nanocomposite are performed by Raman spectrometer, Bruker RFS-27, using Nd-YAG laser, at room temperature. The Raman scattering spectra of CeO_2/CoPc nanocomposites are recorded in the spectral range of 500–3500 cm^{-1}, as displayed in Fig.5.9. The frequency region 550–1650 cm^{-1} corresponds to heavy atom-nitrogen (Co-nitrogen) in-plane stretching and bending vibrations as well as displacements on the C-N-C bridge bond of the phthalocyanine molecule [6]. The structural studies of CeO_2 on the basis of Raman spectroscopy is discussed in *Section 3.3.2.5*. The Raman-active band at 460 cm^{-1} in the sample C1 is attributed to the fluorite structure, which is due to the symmetrical stretching vibration mode of *Ce-O8* [3].The vibrations of the CoPc planar molecule having 57 atoms and possessing *D4h* point group symmetry can be classified into following irreducible representation (taking into account only internal vibrations) [13]

$$\Gamma vib = 14A_{1g} + 13A_{2g} + 14B_{1g} + 14B_{2g} + 13_{Eg} + 6A_{1u} + 8A_{2u} + 7B_{1u} + 7B_{2u} + 28E_u;$$

where A1g, B1g, B2g, and Eg are Raman-active modes. The non-degenerate A1g, B1g, and B2g modes are in-plane vibrations, and double-degenerate Eg mode are out-of-plane vibration. It can be noticed from Fig.5.9 that Raman active modes of the symmetry A1g at 567

cm^{-1}, 848 cm^{-1}, B1g at 689 cm^{-1}, 1541 cm^{-1}, and B2g at 1451cm^{-1} for CoPc are present in sample C1. All these Raman bands are associated with vibrations of C–N–C bridge bonds and vibrations of central atom of phthalocyanine molecule (Co) connected with nitrogen atoms [6]. In brief, Raman studies also confirm the formation of CeO_2/CoPc nanocomposite.

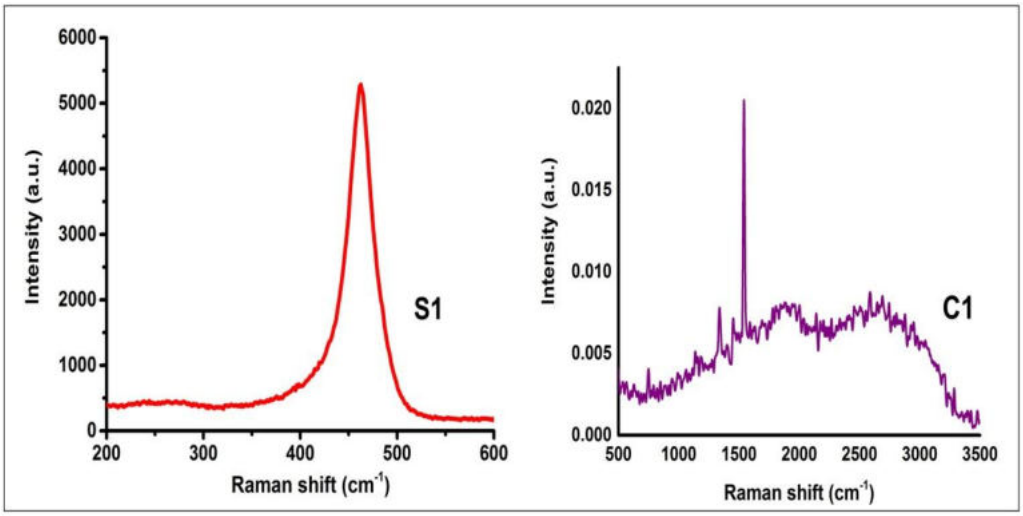

Fig.5.9 Raman spectra of CeO_2 nanoparticles and CeO_2/CoPc nanocomposite

5.3.3 Optical properties

UV-Visible absorption and photoluminescence spectra of the prepared nanocomposites are carried out by following the procedure as given in *Section 2.4.3.*

5.3.3.1 UV-visible absorption spectroscopy

Optical properties of the CeO_2/CoPc nanocomposite in terms of its absorption spectra are collected by Shimadzu UV-2600 UV-Visible

spectrophotometer. Kubelka Monk transformation is used for measuring absorbance, which is recorded as a function of wavelength in the range 200-900 nm as seen in Fig.5.10.

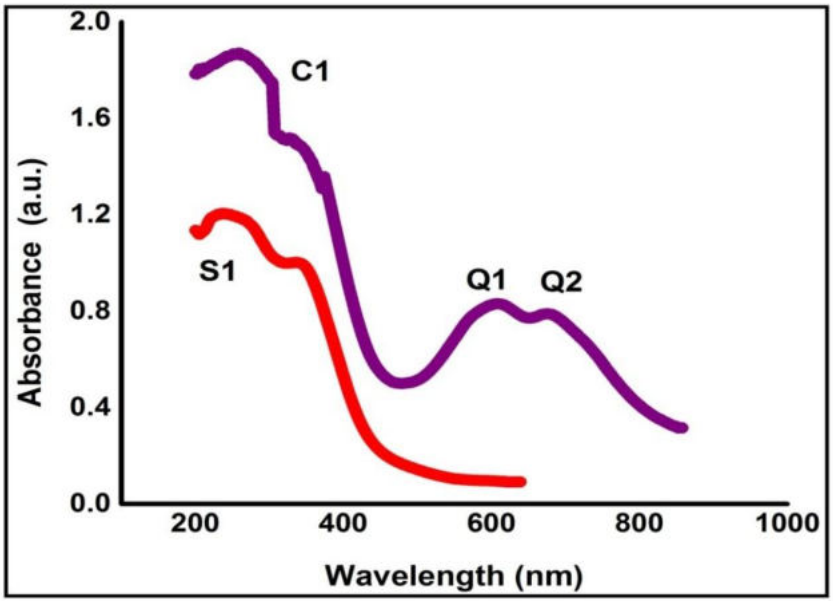

Fig.5.10 Optical absorption spectra of CeO_2 nanoparticles and CeO_2/CoPc nanocomposite

Samples S1 and C1 show very good absorption in the regions 200–300 nm, centered on 240 nm. The absorption of CeO_2 in the UV region originates from the charge-transfer transition between the O 2p and Ce 4f states [14, 15]. In C1, the intense bands in the regions 300–400 nm (Soret band) and 650–700 nm (Q band) correspond to absorption peaks of metal phthalocyanines [6]. The peaks at higher-energy and low-energy regions result from B (Soret band) band and Q bands respectively, which arise from π-π* transitions [16]. The absorption bands from 400–800 nm region are caused by the π-π* transitions of the

conjugated macrocycle of 18 π- electrons [6]. The intensity of higher energy peak, Q1 is larger than the Q2, which represents CoPc α-phase. The absorption maxima at the Q band with wavelengths of 607 and 675 nm correspond to α-phase of CoPc and these peaks are separated by 68 nm. From Fig. 5.10, it is observed that the absorption edges of composite samples show a bathochromic shift with an increased absorption intensity revealing the perturbance in the electronic states of CeO_2/CoPc nanostructures [17]. The Tauc plots for CeO_2 and CeO_2/CoPc sample are shown in Fig.5.11[18]. Optical band gap energy of the samples S1 and C1 are tabulated in Table 5.4.

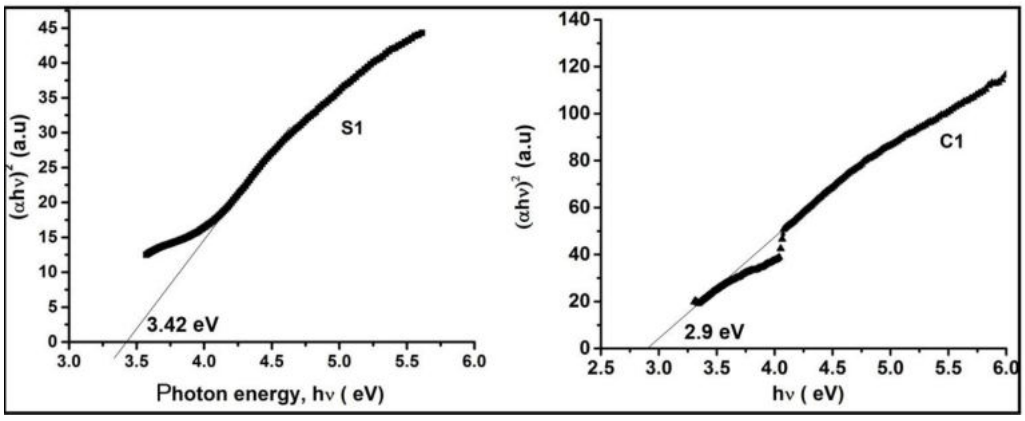

Fig.5.11 Tauc plot of CeO_2 nanoparticles and CeO_2/CoPc nanocomposite

Table 5.4 Optical band gap energy of CeO_2 and CeO_2/CoPc

Sample	Optical band gap energy (eV)	Absorption edge (nm)
S1	3.42	440
C1	2.9	475

The optical band-gap energies are 3.42 and 2.9 eV for the samples S1 and C1, respectively. The lowering of band-gap value for the nanocomposite sample relative to nanoceria is due to the presence of cobalt in the CoPc [19]. The cobalt ions present in the CoPc create oxygen vacancies and favor the formation of Ce^{3+} from Ce^{4+}. This increases the amount of Ce^{3+} states, resulting in the formation of localized energy states that are closer to the conduction band, and thereby decreasing the band gap [6]. In addition to this, the average particle size of CeO_2/CoPc nanocomposites is larger than that of CeO_2 nanoparticles. This will broaden the highest occupied molecular orbit (HOMO) in the valence band and the lowest unoccupied molecular orbit (LOMO) in the conduction band energy levels, which leads to narrowing of the band gap. In brief, optical absorption results show that CeO_2/CoPc nanocomposite can help us to extend the optical absorption spectra of CeO_2 from the UV region to the entire span of visible light. Moreover, lowering of band gap values and enhanced absorption intensity of the composite sample confirm that inclusion of CoPc in CeO_2 improve the optical properties. This can find applications in the field of electro-photographic systems, diodes, laser printers, photovoltaic cells and photo-electrochemical devices [20, 21].

5.3.3.2 Photoluminescence spectroscopy

Optical properties of CeO_2/CoPc nanocomposite sample in terms of its emission spectra are recorded at room temperature using a Fluoromax-3 spectrophotometer. The emission spectra of CeO_2 nanoparticle and composite samples are recorded in the range 350–600 nm at an excitation wavelength of 330 nm using an excitation slit width of 5 nm, and are presented in Fig.5.12. It has been reported in the literature that CoPc does not show fluorescence because of its strong spin orbit interaction [22]. However, a weak emission peak is observed at the 394 nm in the PL spectrum of C1, which is in the soret band region. The PL emission for CeO_2/CoPc nanocomposites can be assumed to be the transition from *4f* band of cerium to the *2p* band of O. The broad emission band ranging from 350 to 575 nm of the samples S1 and C1 is the result of defects, including oxygen vacancies in the crystal with electronic energy levels below the 4f band [23]. Intense blue bands are observed at 435 nm (2.85 eV) and 448 nm (2.77 eV), respectively, for samples S1 and C1. A strong blue emission at 465 nm (2.66 eV), blue green emission at 481 nm (2.58 eV) and 490 nm (2.53 eV), and a good green emission at 540 nm (2.29 eV) are also observed for both the samples. The PL emission at 465 nm (2.67 eV) is related to the defects such as dislocations, which is helpful for fast oxygen transportation.

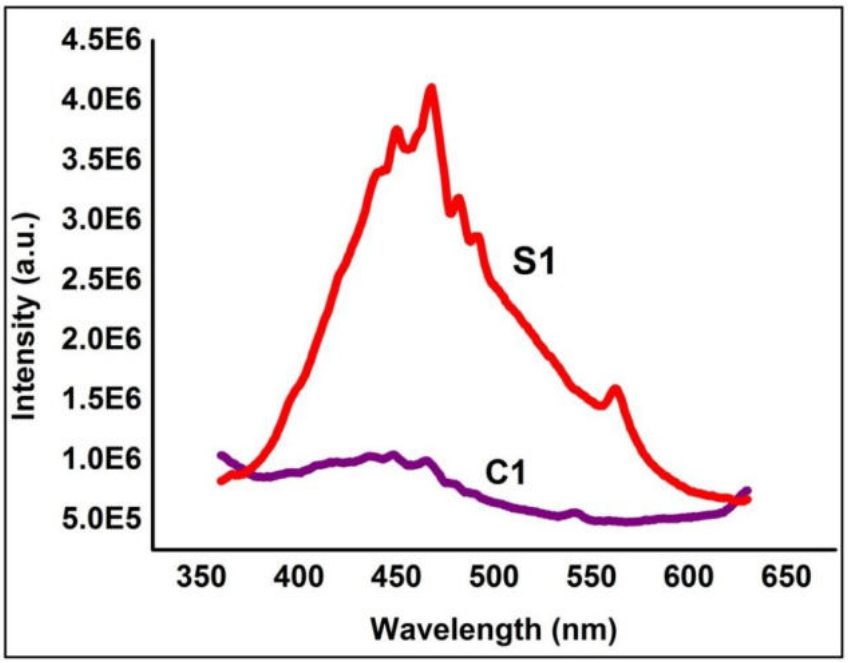

Fig.5.12 PL spectra of CeO_2 nanoparticles and CeO_2/CoPc nanocomposite

It is interesting that the PL intensity for CeO_2/CoPc nanocomposite sample is smaller than that of CeO_2 sample. Co in CoPc can improve the life time of excitations by proper transferring and trapping of photo-excited charges through synergistic effect of optimum concentration of the CoPc and associated crystal defects [6,19]. Hence, the intensity of PL spectra is lower for CeO_2/CoPc nanocomposite samples. This indicates that CoPc of appropriate concentration helps to enhance photo-efficiency and photo-activity of CeO_2 nanoparticles for potential applications in solar cells and photocatalysis.

The colour of emission are measured and presented by the resultant chromaticity coordinates (*x*, *y*). CIE-XYZ colour space is the standard reference. Fig.5.13 exhibits the CIE chromaticity diagram for the synthesized CeO_2 nanoparticles (S1) and CeO_2/CoPc nanocomposite sample (C1). The *x* and *y* chromaticity coordinates under the excitation of 330 nm are calculated in CIE XYZ colour space. Table 5.5 shows the chromaticity coordinates of the sample S1 and C1. A unique greenish-blue colour emission is obtained for both S1 and C1, when excited with 330 nm which is in the near-UV region. In brief, the synthesized nanocomposite with suitable concentration of CoPc can be used to construct CeO_2 phosphors for near-ultraviolet (NUV) light-excited greenish blue light-emitting diodes (LEDs) and optoelectronic devices [24].

Table 5.5 Chromaticity coordinates of CeO_2 nanoparticles and CeO_2/CoPc nanocomposite

Sample	*x*	*y*
S1	0.18846	0.26176
C1	0.176	0.262

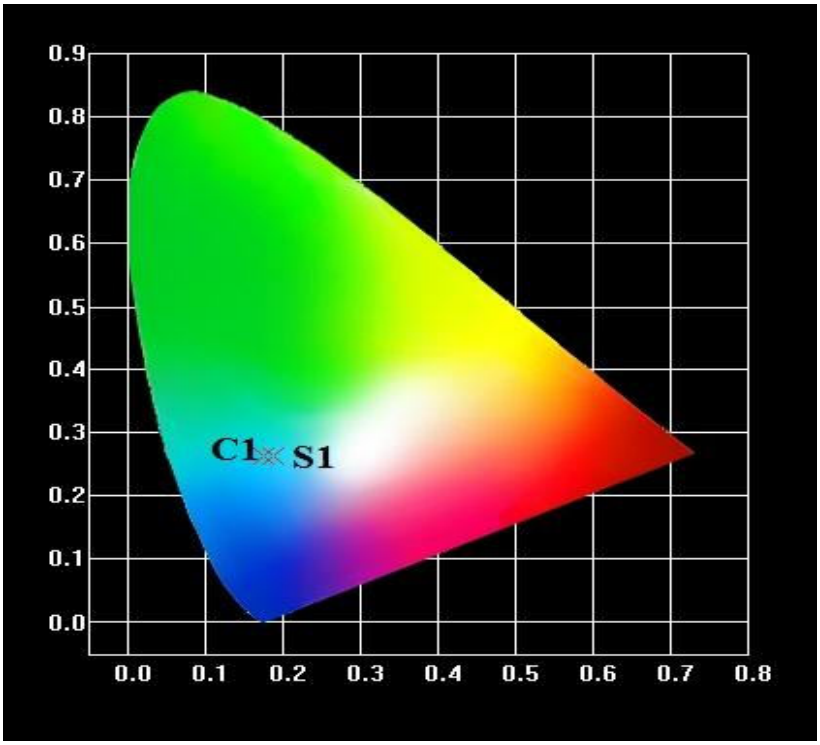

Fig.5.13 Chromaticity diagram of CeO_2 nanoparticles and CeO_2/CoPc nanocomposite

5.3.4 Electrical properties

The electrical studies are carried out by following the procedure given in *Section 2.4.4*. In order to study the conduction mechanism and dielectric properties of CeO_2/CoPc nanocomposite, powder samples are consolidated in the form of cylindrical pellet of diameter 13 mm and thickness 1.2 mm. Both the faces of the pellets are covered with air drying silver paste for good electrical contact. Dielectric measurements as a function of frequency in the range of 100 Hz−10 MHz are measured at various temperatures (303, 393 and 423 K) using Wayne Kerr H-6500B model impedance analyzer.

5.3.4.1 Frequency and temperature dependence of dielectric constant

Variation of dielectric constant (ε') of CeO_2/CoPc nanocomposite with frequency at 303, 393 and 423K are displayed in Fig.5.14. At low frequency region, electrical measurements are influenced by polarization due to the displacement of the charge carriers and at high frequencies the contribution from the lattice is considered [25]. It is observed that dielectric constant is frequency dependent with the highest response occurring at the lower frequencies of the applied electric field and it could be explained by Maxwell-Wagner model [26]. At room temperature the value of ε' is 39 at 100 Hz, which decreased to 7 at 10 MHz. The corresponding values at 423 K are 50 and 10, respectively. As explained in *Section 3.3.4.1*, dielectric behavior of the nanostructured materials is determined by various types of polarization such as space charge and rotational polarization [27-30]. Beyond a particular frequency of the applied electric field, the electron exchange does not follow the alternating field [31]. Hence, the polarization decreases, which in turn causes a decrease in dielectric constant ε'. At very high frequency region the charge carriers would have started to move before the field reversal occurs and ε' falls to a small value [30]. The delocalized π electrons associated with CoPc play a major role in their conductive property. As the applied field is increased, the probability of tunneling of electrons will increase that leads to high dielectric permittivity [32]. From Fig.5.14, it is observed that the dielectric constant increases with temperature, but it decreases with frequency. The ε' changes from 39 to

50, when temperature changes from 303 to 423 K. This may be due to the linear dependence of dielectric polarization with temperature [30].

Fig.5.15 compares the dielectric behavior of CeO_2/CoPc with CeO_2 nanoparticle at 303K. It is observed that dielectric constant is low for the nanocomposite sample as compared to CeO_2 sample. The addition of CoPc into CeO_2 reduces the value of the dielectric constant from 66 to 39 (100 Hz) at room temperature [25]. The decrease in dielectric constant for the nanocomposite is due to changes in the space charge distribution caused by the addition of CoPc [26]. The considerably low values of permittivity is probably due to the sub - microscopic inhomogeneities, presence of other impurities such as oxygen in the samples and the low packing density of the synthesized materials [33].

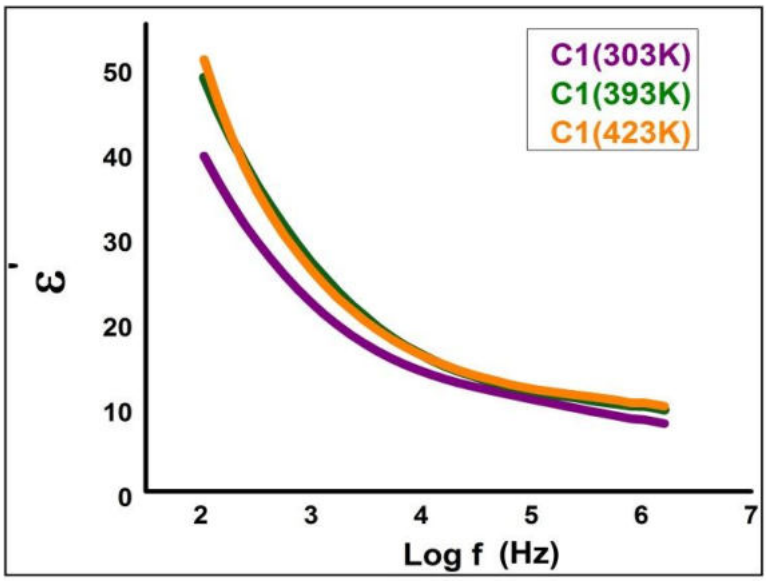

Fig.5.14 Variation of dielectric constant with frequency of CeO_2/CoPc at different tem- peratures

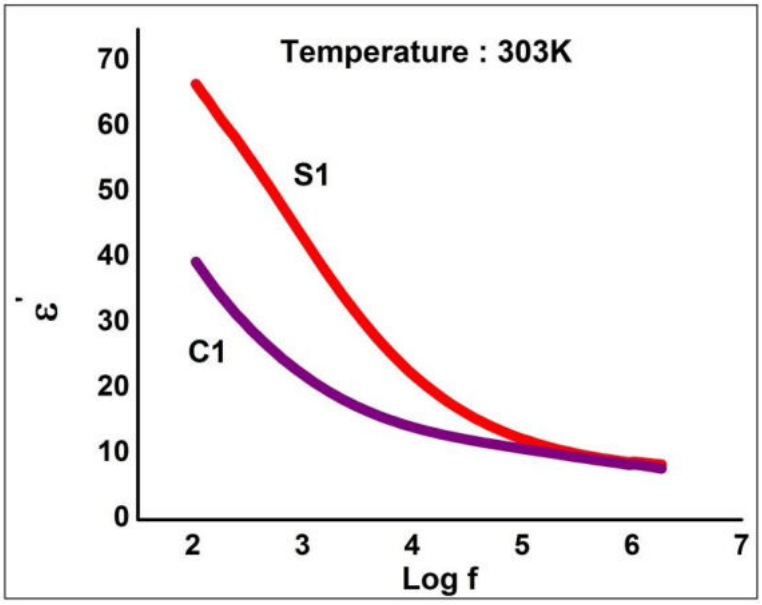

Fig.5.15 Variation of dielectric constant with frequency of CeO_2 (S1) and CeO_2/CoPc (C1) at 303K

The high value of ε' is important for making high k gate dielectrics for field-effect transistors (FET) [34]. Both the samples S1 and C1 have high values of dielectric constant compared with silicon dioxide (SiO_2), which has been used as a gate oxide material for decades. It is possible to increase the gate capacitance and device performance by reducing the thickness of the gate dielectric to a few nanometers (~2 nm) [25]. But as the thickness is reduced to a few nanometers, leakage current of SiO_2 increases significantly due to tunneling, which may result in large power consumption and reduced device reliability [35, 36]. By replacing the silicon dioxide gate dielectric with a high k material, an increased gate capacitance is obtained without the associated leakage effects [25].

5.3.4.2 Frequency and temperature dependence of tangent loss

The dielectric tangent loss is a measure of energy loss in the dielectric during AC operation, which is a material property and does not depend on the geometry of capacitor. Fig.5.16 shows the variation of tangent loss of CeO_2/CoPc with frequency at different temperatures. In nanomaterials, at low frequency region, the interfacial loss and the loss from electrical conductivity are dominant. In the low frequency region, which corresponds to high resistivity of grain boundaries, more energy is required for electron hopping and as a result the loss is high. However, in the high frequency region, which corresponds to the high conductivity of grain, energy required for hopping of electrons is less and hence, tanδ is low [37, 38]. From Fig.5.17, it is noticed that dielectric loss is low for the nanocomposite sample as compared to CeO_2 at room temperature. A low dielectric loss material is preferred, in order to reduce the energy dissipation and signal losses, in high frequency applications [25]. The absence of dielectric loss peaks in the frequency versus dielectric loss curves of the present samples show the wide distribution of relaxation times [39]. CeO_2/CoPc nanocomposite with modified values of dielectric constant and low loss tangent at higher frequencies is important for the fabrication of materials for photonic, microelectronics such as substrate applications and electro-optic devices [34].

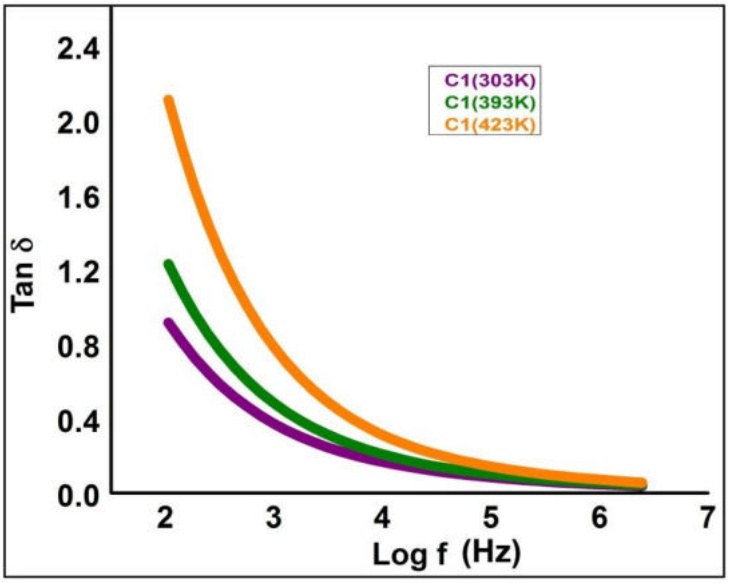

Fig.5.16 Variation of tangent loss with frequency of CeO_2/CoPc at different temperatures

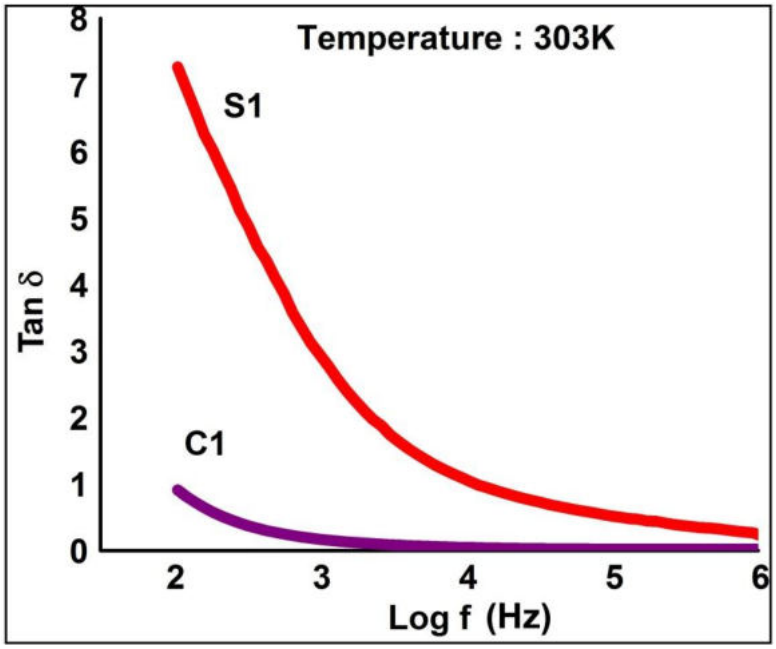

Fig.5.17 Variation of tangent loss with frequency of CeO_2 and CeO_2/CoPc at 303K

5.3.4.3 Frequency and temperature dependence of AC conductivity

The variation of AC conductivity as a function of frequency for temperatures from 303 to 423 K of the composite sample C1 is shown in fig.5.18. At 303 K, σ_{ac} has a value of 7.28×10^{-7} S/m at 100 Hz which is increased to 9.8×10^{-5} S/m at 10 MHz. At 393 and 423 K, the maximum values of AC conductivity at 10 MHz are 1.04×10^{-4} S/m and 1.1×10^{-4} S/m, respectively. It can be seen from Fig. 5.18 that the variation of σ_{ac} with frequency is small when the temperature varies from 303 K to 423 K. As the frequency is increased, the conductivity shows a fast increase and attains maximum value at higher frequencies. Similar variation is observed at all the temperatures. This behaviour can be attributed due to the polaron transport or hopping of holes which enable the conductivity to increase monotonically with increase in frequency of the applied field [32, 40]. As the temperature increases, AC conductivity slightly increases with frequency. This is due to the increase in mobility of charge carriers with increase in temperature [32].

Fig.5.19 compares the AC conductivity of the CeO_2/CoPc nanocomposite and CeO_2 nanoparticles at room temperature. The figure shows a decrease in AC conductivity of CeO_2 when CoPc is added. This may occur due to trapping of charge carrier (holes) between the localized sites [25]. The conductivity of CoPc can be due to both hopping of holes and charge transport through excited states. The p-type semiconductivity is affected by the adsorption and desorption of gases such as oxygen, impurities and the crystal structure of the samples [41, 42].

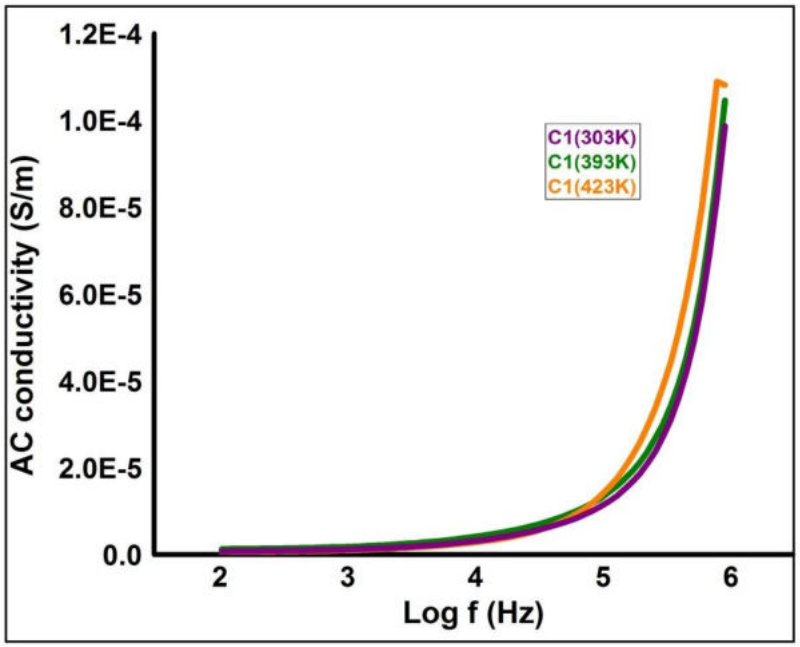

Fig.5.18 Variation of AC conductivity with frequency of CeO_2/CoPc at different temperatures

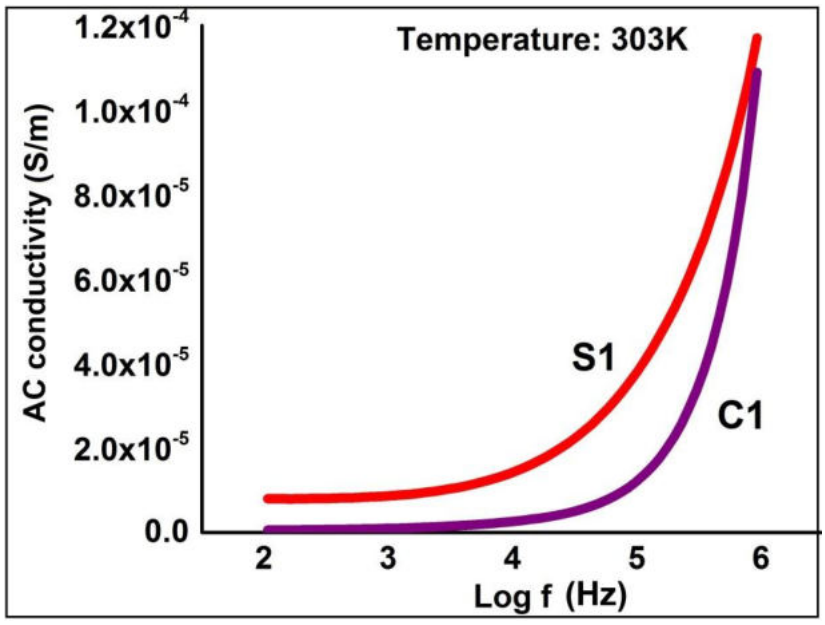

Fig.5.19 Variation of AC conductivity with frequency of CeO_2 and CeO_2/CoPc at 303K

Fig.5.20 shows the $log(\sigma_{ac})$ versus $log(\omega)$ plots of CeO_2/CoPc nanocomposite at different temperature. Values of the frequency exponent *S* are calculated from the slope of the straight lines of the data presented in Fig.5.20. It is found that the value of *S* decreases (0.89 to 0.76) with increase in temperature from 303 to 423 K for the CeO_2/CoPc nanocomposite. All the observed *S* values are less than unity, indicating that hopping is the main conduction mechanism thereby proving the Jonscher's universal power law for the samples [43].

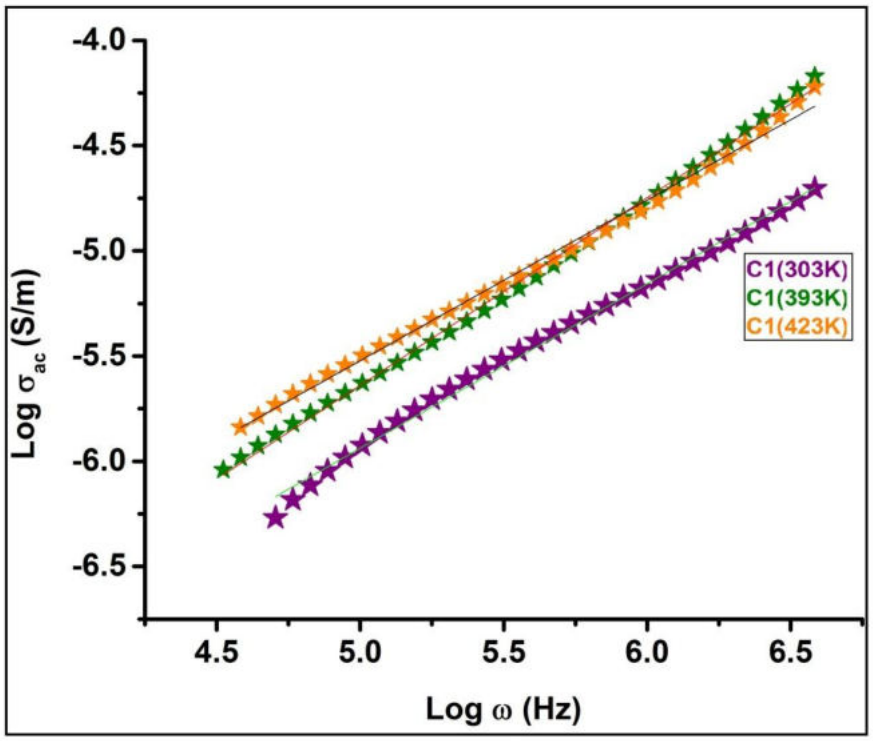

Fig.5.20 Log(σ_{ac}) versus log(ω) plots of CeO_2/CoPc nanocomposite

5.4 Conclusions

- CeO_2/CoPc nanocomposite sample is successfully synthesised by solvent evaporation method.
- The TGA/DTA/DTG studies confirm that the composite is thermally stable in the range 120–700°C.
- The structural properties of the nanocomposite sample is characterized by XRD, TEM, FTIR and Raman studies and their results confirm the formation of CeO_2/CoPc in the sample.
- Compositional analysis using EDX detects the presence of cerium, cobalt, carbon, oxygen and nitrogen in the synthesized nanocomposite.
- FTIR and Raman spectroscopic studies confirm the successfull attachment of CoPc in CeO_2.
- Optical absorption results show that CeO_2/CoPc nanocomposites can help us to extend the optical absorption spectra of CeO_2 from the UV region to the entire span of visible light. A decrease in band-gap energy together with an improved absorption intensity of the nanocomposite is observed.
- PL spectra and CIE diagram show the existence of wide emission peaks in the blue-green region, when excited with near-ultraviolet light. This makes CeO_2/CoPc is a promising material in photocatalytic, solar cells, NUV light-excited LEDs, and optoelectronics applications.

- Dielectric constant, tangent loss and electrical conductivity of CeO_2/CoPc nanocomposite is found to depend on both temperature and frequency.
- At lower frequencies, dielectric constant and tangent loss have higher values, while at higher frequencies, the dielectric response reaches steady lower values. The nature of the curves remained the same when the temperature is raised, but the values are shifted upwards.
- The AC conductivity increases as the frequency is increased, due to polaron hopping.
- It is observed that the dielectric constant, the loss factor and the AC conductivity for the CeO_2/CoPc nanocomposite are lower than those of nanoceria.
- The modified structural, optical and electrical properties of the CeO_2/CoPc nanocomposite can be used for the fabrication of materials for photonic,microelectronic and electro-optic devices.

References

[1] N. Kobayashi, Bull. Chem. Soc. Jpn., 75 (2002) 1-19.

[2] A. A. Ansari, M. A. M. Khan, M. N. Khan, S. A. Alrokayan, M. Alhoshan, M. S. Alsalhi, J. Semicond., 32, 4 (2011) 043001-043006.

[3] K. K. Babitha, A. Sreedevi, K. P. Priyanka, Boby Sabu and Thomas Varghese , Indian J. Pure Appl. Phys., 53 (2015) 596-603.

[4] B. N. Achar, K. S. Lokesh, G. M. Fohlen and T. M. Mohan Kumar, React.Funct. Polym., 63(2005) 63–69.

[5] F. V. Burgos, Fuel, 99 (2012) 106–117.

[6] K. K. Babitha, K. P. Priyanka, A. Sreedevi, O. P. Jaseentha and Thomas Varghese. Int. J. Appl. Ceram. Technol., (2016) 1–8.

[7] B. D. Cullity, Elements of X-Ray Diffraction, Addison-Wesley, MA (1967).

[8] G. K. Williamson and W. H. Hall, Acta. Metall., 1(1953) 22.

[9] S. B. Khan, M. Faisal, M. M. Rahman, and A. Jamal, Sci. Tot. Environ., 409 (2011) 2987–2992.

[10] F. Niu, Mater. Lett., 63(2009) 2132–2135.

[11] R. Aroca and A. Thedchanamoorthy, Chem. Mater., 7 (1995) 69–74.

[12] D. Li, D. Peng, L. Deng, Y. Shen, and Y. Zhao, Vibrat. Spectrosc., 39 (2005) 191–199.

[13] B. A. Kolesov and T. V. Basova, Thin Solid Films, 304 (1997) 166–169.

[14] Z. Wang, Z. Quan and Lin, J. Inorg. Chem., 46 (2007) 5237.

[15] S. Phoka, P. Laokul, E. Swatsitang, V. Promarak, S. Seraphin, and S. Maensiri, Mater. Chem. Phys., 115 (2009) 423–428.

[16] K. R. Rajesh and C. S. Menon, Indian J. Pure Appl. Phys., 43(2005) 964–971.

[17] V. Mani, R. Devasenathipathy, Shen-Ming Chen, Jiun-An Gu, Sheng-Tung Huang, Renewable Energy, 74 (2015) 867-874.

[18] J. Tauc, Amorphous and Liquid Semiconductors, 1 Ed. Plenum Press, New York, (1974).

[19] S. Jayapalan, S. R. Kugalur, S. Padmanaban, M. Devanesan, and T. R.Ramasamy, Mater. Sci. Semicond. Process., 26(2014) 218–224.

[20] S. Grammatica, J. Mort, Appl. Phys. Lett., 38 (1981) 445.

[21] R. O. Loutfy, L. F. Mclntyne, Energy Mater., 6 (1982) 467.

[22] W. Bala, J. Optoelectro. Adv. Mater., 11(2009) 264–269.

[23] A. H. Morshed, M. E. Moussa, S. M. Bedair, R. Leonard, S. X. Liu, and N.E. Masry, Appl. Phys. Lett., 70 (1997) 1647–1649.

[24] F. Hussain, M. Hojjati, M. Okamoto, and R. E. Gorga, J. Compos. Mater., 40(17) (2006) 1511–1575.

[25] K. K. Babitha, K. P. Priyanka, H. Hitha, S. Rintu Mary, E.M. Mohammed, S. Sankararaman and Thomas Varghese. J Electron. Mater. (2017) ; doi: 10.1007/s11664-017-5653-z.

[26] K.W. Wagner, Am. Phys., 40 (1973) 317.

[27] M. Mei, Z. Lide, and W. Guozhong, Nanostruct. Mater., 6(1995) 823.

[28] K.P. Priyanka, J. Sunny, T. Smitha, E.M. Mohammed, and T. Varghese, J. Basic Appl. Phys., 2 (2010) 105.

[29] S. Kim, P. Jain, H.J. Avila-Paredes, A. Thron, K. Benthem,and S. Sen, J. Mater. Chem., 20 (2010) 3855.

[30] A.N. Patil, M.G. Paul, K.K. Patankar, V.I. Mathe, R.P.Mahajan, and S.A. Patil, Bull. Mater. Sci., 23(2000) 447.

[31] D. Ravinder and K. Vijayakumar, Bull. Mater. Sci., 24 (2001) 505

[32] S. Saravanan, C. Joseph Mathai, M. R. Anantharaman, S. Venkatachalam, P. V. Prabhakaran, J. Appl. Polymer Sci., 91 (2004) 2529-2535.

[33] A. M. Saleh, S. M. Hraibat, R. M. L. Kitaneh, M. M. Abu-Samreh, S. M. Musameh, J. Semicond., 33(8) (2012).

[34] K. P. Priyanka, K. K. Babitha, A. Sreedevi, X. Sheena, E. M. Mohammed, and T. Varghese, J. Electroceram., 32(4) (2014) 361-368.

[35] R. Singh and R.K. Ulrich, Electrochem. Soc. Interface, 8 (1999) 26.

[36] C. H. Chen, I. Y. Chang, J. Y. Lee, and F. Chiu, Appl. Phys. Lett., 92 (2008) 043507.

[37] K. M. Batoo, S. Kumar, and C. G. Lee, Curr. Appl. Phys., 9 (2009) 826.

[38] N. Singh, A. Agarwal, and S. Sanghi, Curr. Appl. Phys., 11(2011)783.

[39] W. D. Kingery, Introduction to ceramics, New York: John Wiley (1976).

[40] P. S. Vijayakumar, H. Pohl, J. Polym. Sci. Polym. Phys., 22 (1984) 1439.

[41] A. Wilson, R. A. Collins, Sens. Actuat., 12 (1987) 389.

[42] R. A. Collins, K. A. Muhammed, Thin Solid Films, 145 (1986) 133.

[43] B. M. Greenhoe, M. K. Hassan, J. S. Wiggins, K. A. Mauritz, J. Polym. Scie. Part B: Polymer Physics, (2016); DOI: 10.1002/ polb.24121.

....

Chapter 6

SYNTHESIS AND CHARACTERIZATION OF CeO_2/SnPc NANOCOMPOSITE

6.1 Introduction

Metal–Phthalocyanines (M-Pc) are highly stable p-type organic semiconductors characterized by conjugate bonding, having various applications in the fields of conductive polymers, as chemical sensors and electrochromism [1]. As discussed in *Chapter 1*, CeO_2, the inorganic metal nanoparticles have the potential for high carrier mobilities, band gap tunability, a range of magnetic and dielectric properties, and thermal and mechanical stability [2]. Hence, the combination of CeO_2 with M-Pc will create an organic-inorganic nanocomposite system, which will act as a high performance material exhibiting unusual property combinations and unique design possibilities [3]. In this chapter, the synthesis and characterization of cerium oxide/tin phthalocyanine nanocomposites is discussed. To date, no studies have been reported on the electrical properties of cerium oxide /tin phthalocyanine nanocomposite. The main objectives of this study are to compare the optical properties electrical conductivity and

structural properties of cerium oxide/tin phthalocyanine nanocomposite and cerium oxide nanoparticles.

6.2 Synthesis of CeO_2/SnPc nanocomposite

CeO_2/SnPc nanocomposite is prepared using a standard method by adding CeO_2 nanoparticles calcined at 400°C to tin phthalocyanine (1 wt.%). The mixture is dissolved in a solvent mixture containing 50% dimethyl sulphoxide, 30% dimethyl formamide and 20% ethanol, under constant stirring and heating at 60°C using a magnetic stirrer [1]. After complete solvent evaporation, the obtained composite is dried at 100°C in a hot air oven for 15-20 h to get CeO_2/SnPc nanocomposite in powder form. Room temperature precipitation method for the synthesis of CeO_2 nanoparticles is described in *Section 3.2*. The synthesized CeO_2 nanoparticles calcined at 400°C and CeO_2/SnPc nanocomposite samples are denoted as S1 and C2, respectively. The flow chart showing the scheme of preparation of CeO_2/SnPc nanocomposite is presented in Fig.6.1.

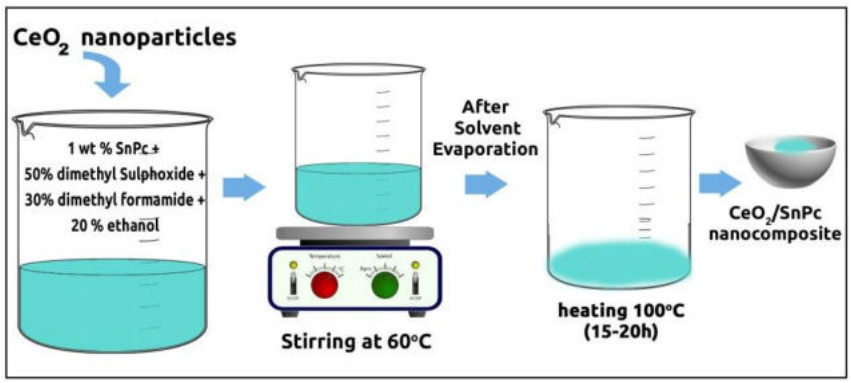

Fig.6.1 Scheme of preparation of CeO_2/SnPc nanocomposite

6.3 Results and discussion

6.3.1 Thermal analysis

Thermogravimetric and differential thermal analysis of the nanoceria and nanocomposite samples are carried out using Perkin Elmer STA 6000. Fig.6.2 depicts the TGA/DTA/DTG curves of CeO_2 nanoparticle (S1) and CeO_2/SnPc nanocomposite (C2) samples. The TGA curve of C2 shows that the weight loss of the precursor occurs from 50 to 300^{o}C. This indicates that the precursor decomposed completely at 300^{o}C to become CeO_2/SnPc nanocomposite [1]. A well structured weight loss is noticed in the TG curve of C2, accompanied by three peaks of weight loss rate in the DTG curve. The first two peaks are located at 63 and 120^{o}C with a weight loss of 0.245 mg/min and 0.182 mg/min, respectively. This weight loss is attributed to the combustion of organic residues due to the crystallization of residual amorphous phase. The DTG curve (C2) demonstrates that the precursor decomposed almost around 120^{o}C to become CeO_2/SnPc nanocomposites. Detailed discussion of thermal studies of CeO_2 nanoparticles is presented in *Section 3.3.1.* The sharp exothermic peak at 249^{o}C in the DTA curve of cerium oxide sample (S1) is not seen in the nanocomposite sample. Moreover, the thermal analysis shows that the synthesized nanocomposite sample is thermally stable in the range of 300-700^{o}C.

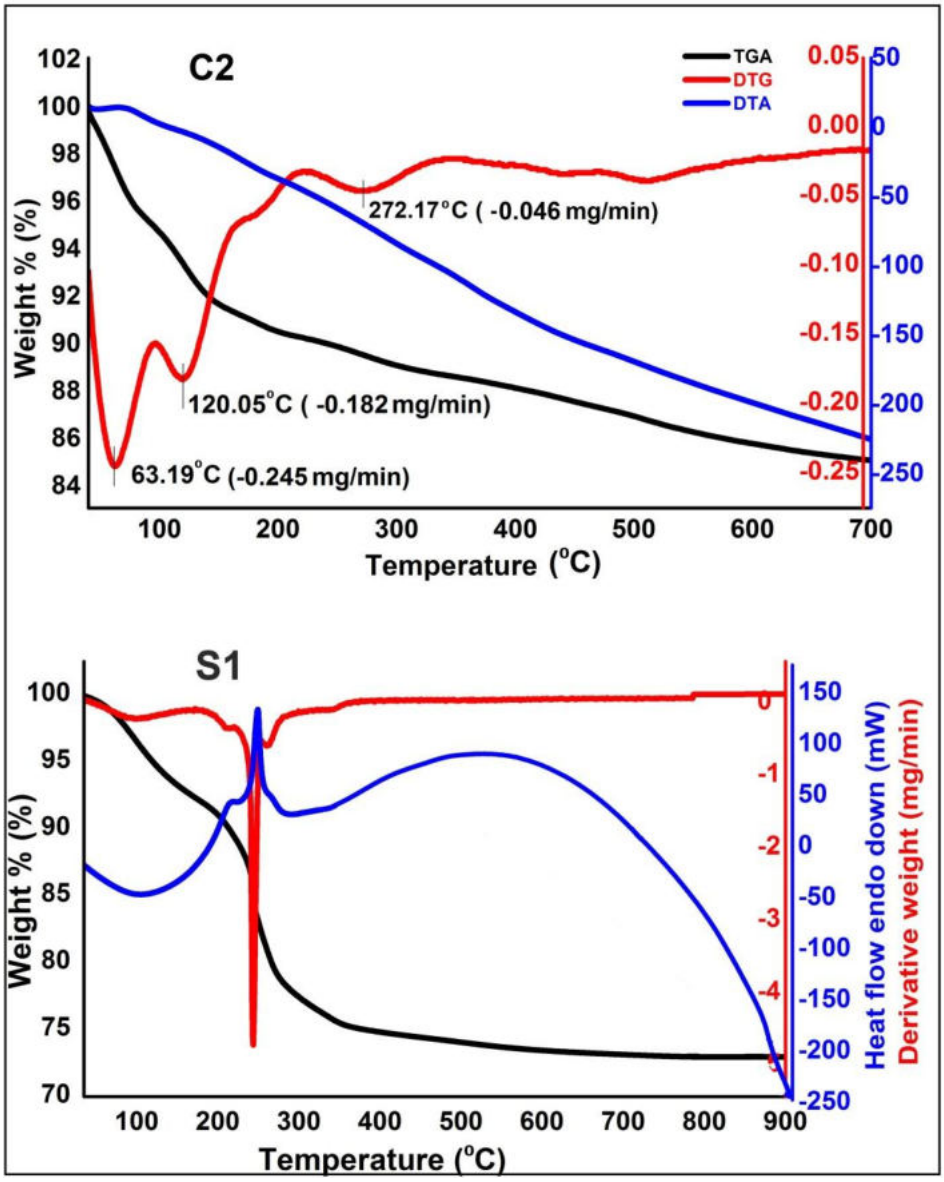

Fig. 6.2 TGA/DTA/DTG curves of CeO_2 nanoparticles (S1) and CeO_2/SnPc nanocomposite (C2)

6.3.2 Structural characterization

The structural analysis of synthesized nanocomposite sample is carried out by following the procedure described in *Section 2.4.2.*

6.3.2.1 Powder XRD analysis

The structural properties of the synthesised nanocomposite are studied by X-ray diffraction method, using Bruker D8 Advance X-ray diffractometer with Cu-Kα radiation (λ = 1.5406Å, X-ray tube voltage = 40 kV and current = 35 mA). The scan is taken in the 2θ range from 0 to 80^o at increments of 0.02^o with a step time of 29.1 s. The X-ray diffraction spectra of CeO_2 and CeO_2/SnPc nanocomposite samples are presented in Fig. 6.3. All the peaks present in the diffractogram of CeO_2/SnPc nanocomposite represent the pure cubic fluorite structure of CeO_2 (space group: *Fm3m*) with lattice constant a = 5.411Å, which is in agreement with the JCPDS file No. 75–0076 for CeO_2. The peaks at 2θ values 28.38^o, 32.87^o, 47.29^o, 56.12^o and 69.29^{o}correspond to planes (111), (200), (220), (311) and (400) respectively, for CeO_2. There is no change in the diffraction pattern of CeO_2 with the addition of SnPc, which is due to the lower loading of SnPc [1]. The peaks in the diffractogram are sharp and intense indicating good degree of crystallinity of the nanocomosite sample .

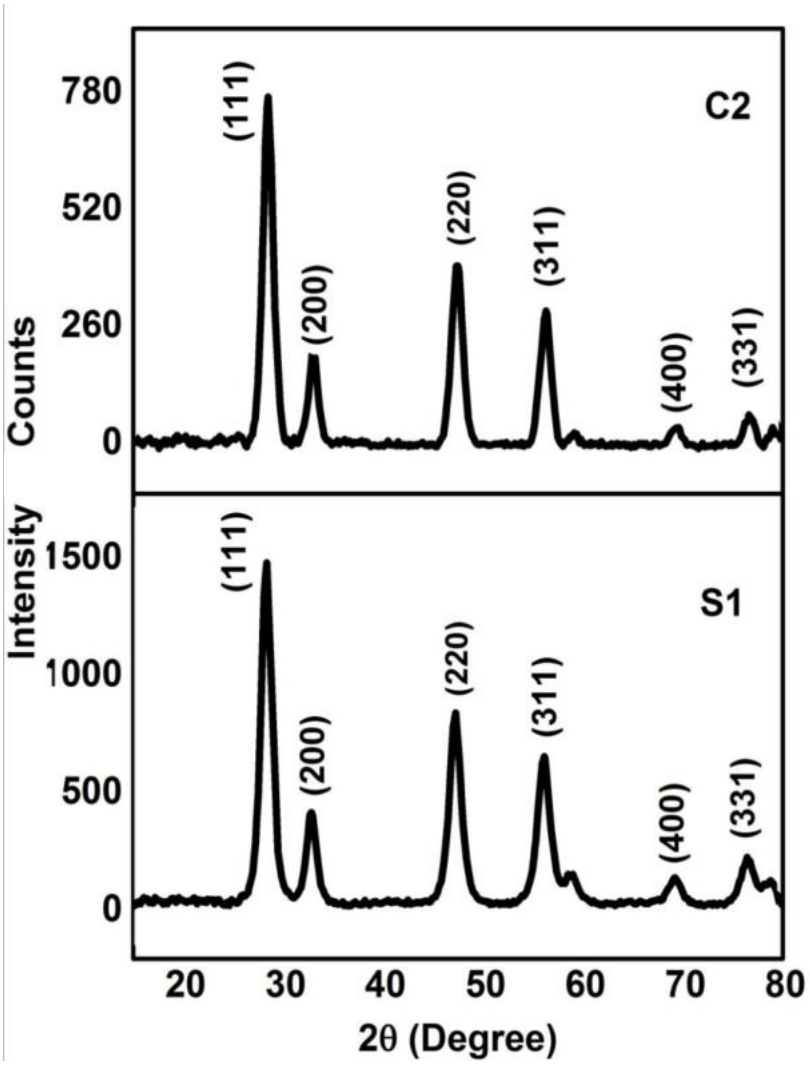

Fig.6.3 XRD patterns of CeO_2 nanoparticles and CeO_2/SnPc nanocomposite

Average crystallite size of the samples are calculated by Scherrer equation [4] and it is 7.3 and 7.5 nm for the sample S1 and C2, respectively. W-H plots of CeO_2 nanoparticles and nanocomposite samples are shown in Fig. 6.4. Average crystallite size and micro-strain value are estimated from the W-H plots [5].

In Table 6.1, structural parameters of CeO_2/SnPc nanocomposite is presented along with results of CeO_2 nanoparticles. It is noticed from Table 6.1 that the crystallite size, *d*– spacing and unit cell volume for the nanocomposite are slightly modified with the addition of tin phthalocyanine. However, the micro-strain and dislocation density values are slightly reduced in the nanocomposite, which indicates the successful incorporation of SnPc in CeO_2.

Table 6.1 Structural parameters of CeO_2 and CeO_2/SnPc

Sample	Average particle size (nm)		Lattice constant *a* (Å)	d spacing (d_{111}) (Å)	Volume of unit cell (Å^3)	Micro strain (x10^{-3})	Dislocation density (nm^{-2})
	Scherrer method	W-H method					
S1	7.3	8.4	5.403	3.1194	157.73	4.54	0.0188
C1	7.5	9	5.44	3.1424	160.99	2.29	0.0178

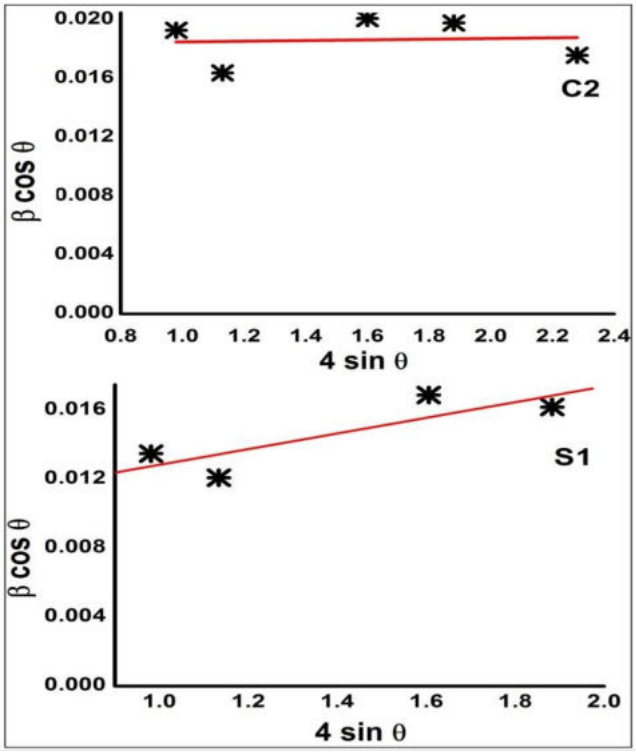

Fig.6.4 W-H plots for CeO_2 nanoparticles and CeO_2/SnPc nanocomposite

6.3.2.2 TEM analysis

TEM images of nanophase cerium oxide and nanocomposite samples are taken on a JEOL MODEL JEM-2100 electron microscope operated at 200 kV. TEM bright field, HRTEM image and selected area electron diffraction pattern of the nanocomposite sample along with cerium oxide are shown in Fig 6.5. The TEM images of nanoceria sample (S1) has been discussed in *Section 3.3.2.2*. It can be observed from the bright field image (Fig.6.5(a)) that particles are almost spherical in shape. The particle size obtained from TEM image ranges from 7 to 8 nm, which is in agreement with the XRD result. HRTEM image indicates the polycrystalline nature of the sample. The SAED

pattern (Fig.6.5(c)) contains bright spots for the composite sample and each spot arising from Bragg reflection from individual crystallite [1].

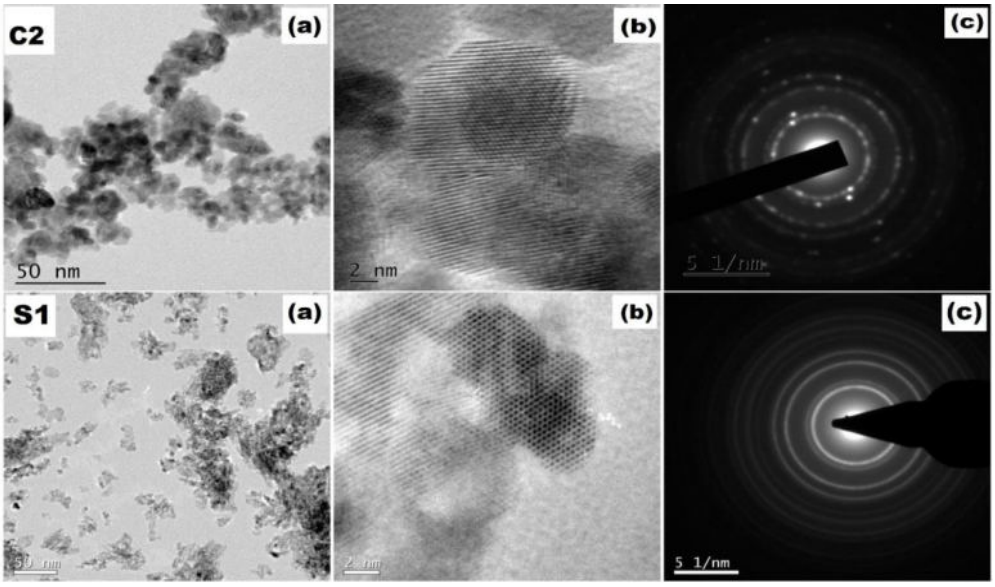

Fig.6.5 TEM images of CeO_2 and CeO_2/SnPc : (a) bright field images, (b) HRTEM images and (c) SAED patterns

6.3.2.3 SEM and EDX analysis

The surface morphology of the nanocomposite sample is analyzed with a scanning electron microscope JEOL MODEL JSM-6390LV, operating at 20 kV. SEM photographs of cerium oxide nanoparticle samples and CeO_2/SnPc nanocomposites are presented in Fig.6.6. It is observed that grains are not in uniform size and shape. The photographs of the samples contains irregular crystallized nanoparticle clusters.

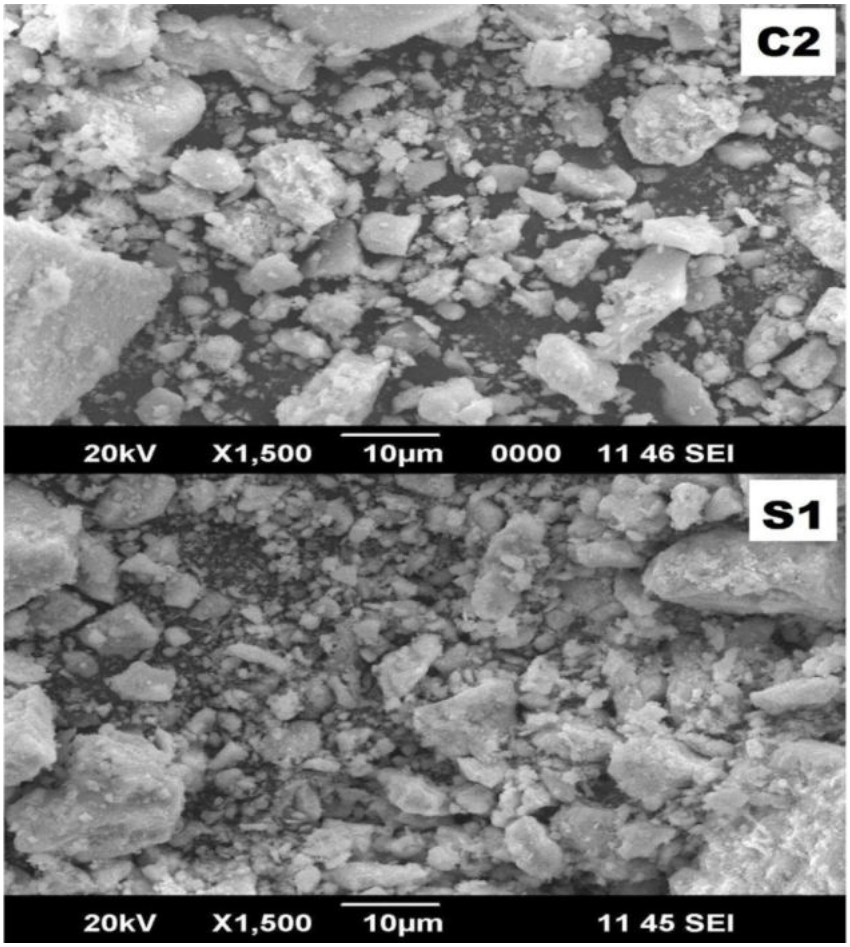

Fig.6.6 SEM images of CeO_2 nanoparticles and CeO_2/SnPc nanocomposite

For collecting the EDX pattern of the synthesized nanocomposite sample, JEOL model JED-2300 with Bruker X flash 6/10 EDS detectors are used. Fig.6.7 shows the EDX analysis results of C2. It exhibits that the nanocomposite contains Ce, Sn, O, C and N. Thus, the EDX study confirms the formation of CeO_2/SnPc nanocomposite. The mass and atom percentages of the sample are presented in Table 6.2.

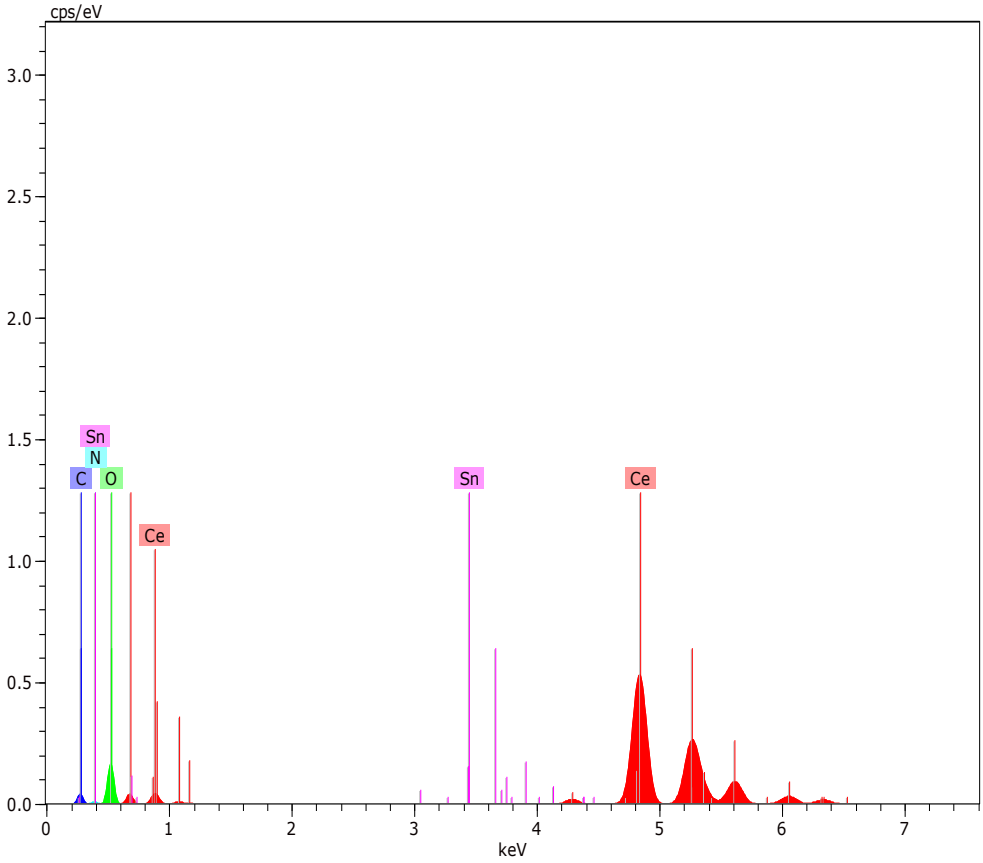

Fig.6.7 EDX pattern of CeO_2/SnPc nanocomposite

Table 6.2 EDX data of CeO_2/SnPc nanocomposite

Element	AN	Series	Norm. wt. %	Atom. %
Ce	58	L	76.52	25.53
O	8	K	15.57	45.5
C	6	K	5.65	22
N	7	K	2.07	6.9
Sn	50	L	0.19	0.08
		total	100	100

6.3.2.4 FTIR analysis

The FTIR spectra of CeO_2 and CeO_2/SnPc samples are recorded by Thermo Nicolet, Avatar 370 and presented in Fig. 6.8. The FTIR illustrated absorption band at 483 cm^{-1} is a typical peak for the Ce-O stretching vibration [6, 7]. The peak at 715 cm^{-1} is due to the phthalocyanine ring vibration [8]. The IR active band near 940 cm^{-1} is related to the metal ligand vibration, indicating the presence of SnPc in the sample [9]. The IR bands at 1617 and 1386 cm^{-1} correspond to physically adsorbed water molecule . The intensity of the hydroxyl peak at 2000- 3760 cm^{-1} is weak, indicating that the water content in the sample is very low. It is observed that the IR bands of CeO_2/SnPc nanocomposite are slightly shifted towards the lower wave number side due to the presence SnPc. In brief, FTIR analysis of the synthesized nanocomposite shows the successful attachment of SnPc to CeO_2.

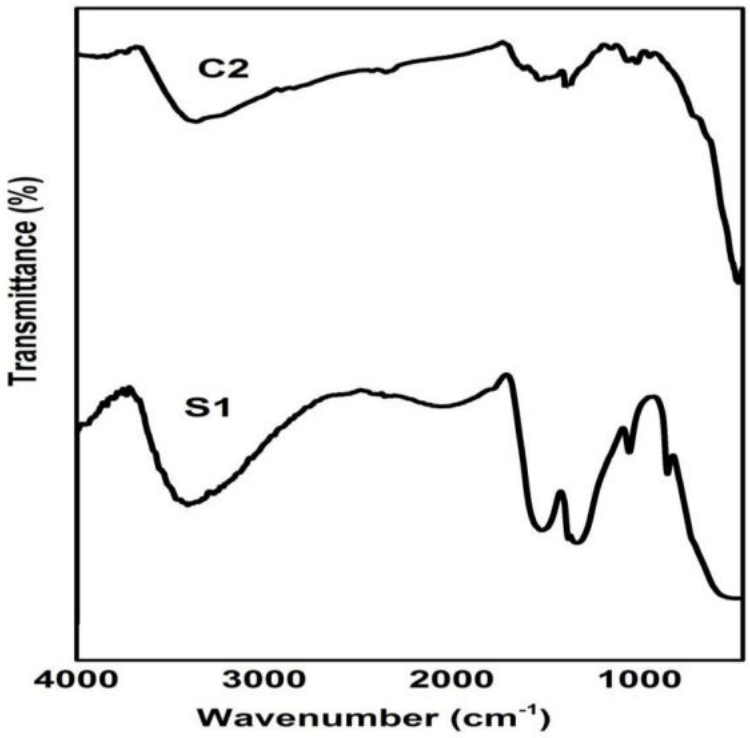

Fig.6.8 FTIR spectra of CeO_2 nanoparticles and CeO_2/SnPc nanocomposite

6.3.2.5. Raman spectroscopy

Raman studies of the CeO_2 and CeO_2/SnPc composite are performed by Raman spectrometer, Bruker RFS-27, using Nd-YAG laser, at room temperature. The Raman scattering spectra of CeO_2/SnPc nanocomposite are recorded in the spectral range of 400–1600 cm^{-1}, as displayed in Fig.6.9. The Raman active band at 467cm^{-1} in the sample C2 is attributed to the fluorite structure, which is due to the symmetrical stretching vibration mode of Ce-O8 [10]. The equilibrium geometry of SnPc is C_{4v} point group symmetry. Here each molecule contains 57 atoms and 165 fundamental vibrations. The number of each irreducible representations are:

$$\Gamma_{vib} = 22A_1 + 19A_2 + 21B_1 + 21B_2 + 41E,$$

where A_1, B_1, B_2 and E are Raman active modes [11]. The most prominent band of SnPc is at 680 cm^{-1}, which is due to vibrations of A_1 symmetry. Raman active modes for CeO_2/SnPc nanocomposite sample are listed in Table 6.3, along with literature values of SnPc. From Table 6.3, it can be observed that the nanocomposite sample contains most prominent Raman active modes of SnPc and symmetrical stretching mode of Ce-O8. Thus, Raman studies also confirm the formation of CeO_2/SnPc nanocomposite.

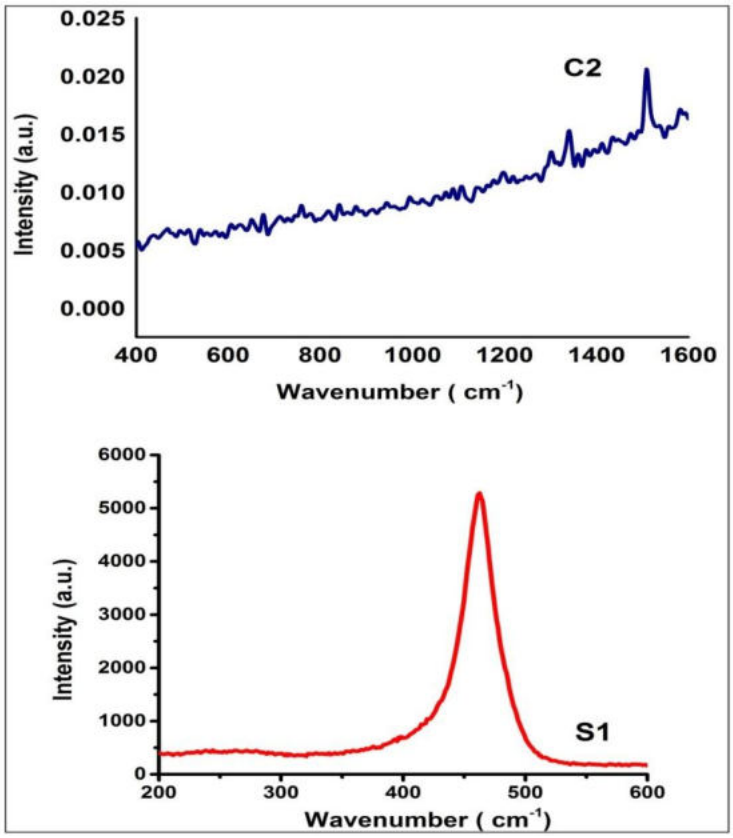

Fig.6.9 Raman spectra of CeO_2 nanoparticles and CeO_2/SnPc nanocomposite

Table 6.3 Raman active modes of CeO_2/SnPc nanocomposite

Vbrational frequency		**Symmetry**	**Description**
CeO_2/SnPc	**SnPc [11]**		
172	185		Macrocycle deformation
467	-		Symmetrical stretching mode of Ce-O8
478	482	B2	Isoindole deformation
676	680	A1	Macrocycle breathing
759	765		Macrocycle ring stretch
841	830		Macrocycle ring stretch
943	953	B2	Benzene breathing
1106	1107		C-H bend
1142	1141	A1	Pyrrole breathing
1197	1184		C-H bend
1301	1311		C-H bend
1340	1342	A1	C=C pyrrole stretch
1519	1527		C-N pyrrole stretch

6.3.3 Optical properties

UV-visible absorption and photoluminescence spectra of the prepared nanocomposite are carried out by following the procedure as given in *Section 2.4.3.*

6.3.3.1 UV-vis absorption spectroscopy

Optical properties of the CeO_2/SnPc nanocomposite in terms of its absorption spectra are collected by Shimadzu UV-2600 UV-Visible spectrophotometer. Kubelka Monk transformation is used for measuring absorbance, which is recorded as a function of wavelength in the range 200-800 nm. Fig.6.10 shows the UV-Visible absorption spectra of CeO_2 nanoparticle and CeO_2/SnPc nanocomposite. Both samples show strong absorption band centred at 250 nm in the UV range, which is originating from the charge transfer transition from O^{2-} (2p) to Ce^{4+} (4f) orbitals in CeO_2 [9, 12]. It can be seen from Fig. 6.10 that the nanocomposite sample contains B Band (Soret) centered at 371nm and Q Bands in the region 645-720 nm,which is due to the electronic transitions from $\pi \rightarrow \pi^*$ orbits [13]. The Soret band in the UV region and Q-bands in the visible region of absorption spectrum originate from molecular orbitals within the aromatic 18π electron system and from overlapping orbitals on the Sn in SnPc. The conjugated double bonds within the crystal structure create electron orbitals and these electrons are able to transfer energy throughout the structure and are responsible for the absorption peaks at Q

and B bands [14, 15]. The absorption threshold edge at 440 nm in CeO_2 nanoparticles is slightly red shifted to 491 nm when SnPc is added to it, which may be due to particle size variation. Table 6.4 presents the optical band gap energy and absorption edge of the samples S1 and C2.

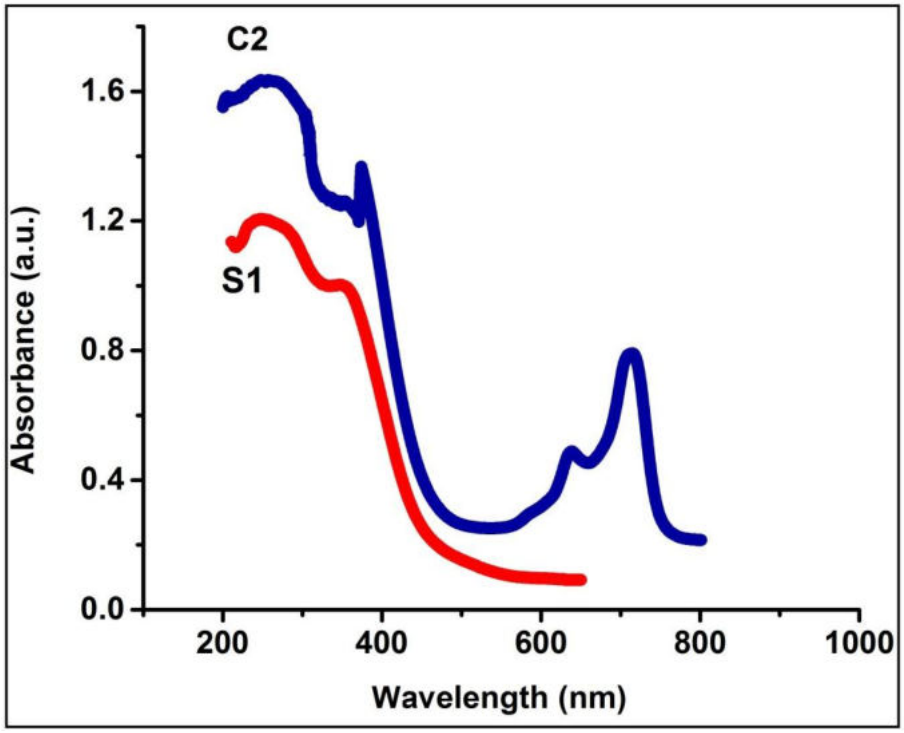

Fig.6.10 Optical absorption spectra of CeO_2 nanoparticles and CeO_2/SnPc nanocomposite

Band gap values of CeO_2 and CeO_2/SnPc samples are measured from Tauc plot [16], as discussed in *Section 2.4.3.1.* The optical band gap values obtained are 3.42 and 3 eV respectively for nanophase CeO_2 and CeO_2/SnPc nanocomposite. Tauc plot for the samples S1 and C2 are displayed in Fig.6.11. The decrease in optical band gap energy of CeO_2/SnPc nanocomposite is due to crystallite growth. The improved absorption intensity, red shifted absorption bands and extended visible

absorption confirms the presence of tin phthalocyanine in the synthesized nanocomposite [1]. Moreover, the addition of SnPc can help us to extend the optical absorption spectrum of CeO_2 from the UV region to the entire span of visible light in addition to enhanced absorption intensity. In short, modification of the optical absorption properties of the nanocomposite can be used for visible light-driven photocatalytic applications [17] .

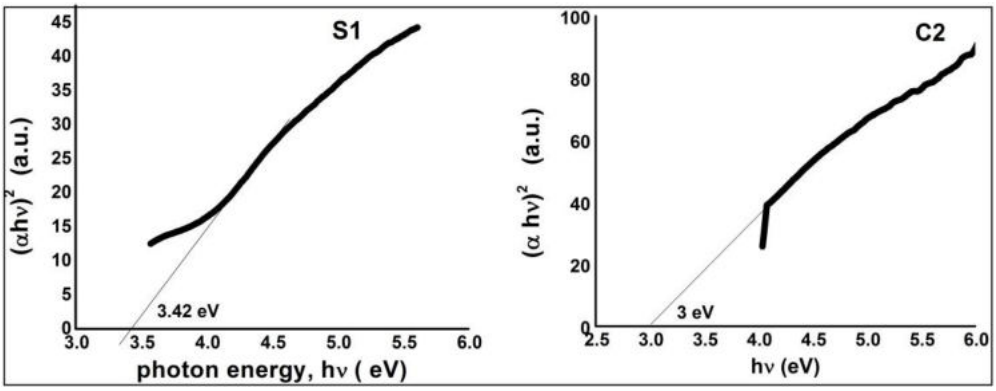

Fig.6.11 Tauc plot of CeO_2 nanoparticles and CeO_2/SnPc nanocomposite

Table 6.4 Optical band gap energy of CeO_2 nanoparticles and CeO_2/SnPc nanocomposite

Sample	Optical band gap energy (eV)	Absorption edge (nm)
S1	3.42	440
C2	3	491

6.3.3.2 Photoluminescence spectroscopy

PL emission spectra of CeO_2 and CeO_2/SnPc nanocomposite samples are recorded at room temperature using a Fluoromax-3 spectrophotometer, in the range 350–600 nm at an excitation wavelength of 330 nm and a slit width of 5 nm. Fig.6.12 shows PL spectra of CeO_2 and CeO_2/SnPc nanocomposite samples.

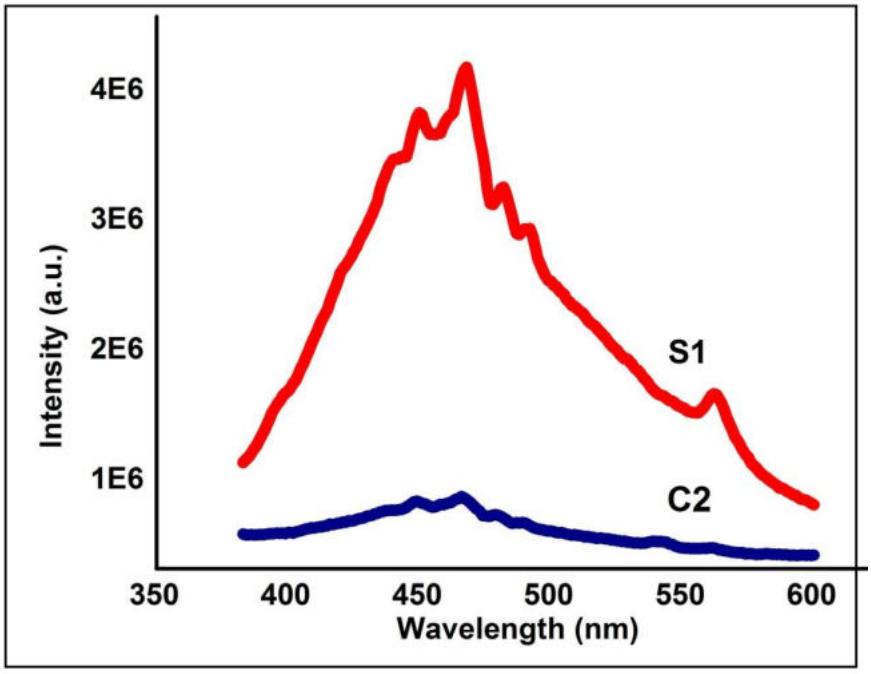

Fig.6.12 PL spectra of CeO_2 nanoparticles and CeO_2/SnPc nanocomposite

The PL emission spectra showa broad emission in the spectral range from 370 to 550 nm along with well defined shoulder peaks at 479 and 489 nm. Both S1 and C2 samples exhibit similar type of PL spectra with a maximum emission in the blue- green region. Intense blue bands are observed at 449 nm (2.76 eV) and 466 nm (2.66 eV), respectively,

for samples S1 and C2. The emission bands at 479 nm (2.58 eV), 489 nm (2.54 eV) and 561 nm (2.21 eV) are also noticed for both the samples. The strong emission at 466 nm (2.66 eV) is related to the defects such as dislocations, which is helpful for fast oxygen transportation [10]. It is observed from Fig.6.12 that the PL intensity of the composite sample is much smaller than that of CeO_2. The presence of Sn can improve the life time of excitations by proper transferring and trapping of photo-excited charges through synergistic effect of optimum concentration of the SnPc and associated crystal defects [1,17]. Hence, the intensity of PL spectra is lower for CeO_2/SnPc nanocomposite samples. The above property indicates that synthesized nanocomposite can be used in solar cells and photocatalysis [17].

Fig.6.13 exhibits the CIE chromaticity diagram of the synthesized CeO_2/SnPc nanocomposite sample and CeO_2 nanoparticles. The *x* and *y* chromaticity coordinates under the excitation of 330 nm are calculated in CIE XYZ colour space. The greenish-blue emission is obtained with CIE coordinates (0.18846, 0.26176) and (0.1756, 0.2811) for CeO_2 nanoparticles and CeO_2/SnPc nanocomposite , respectively (Table 6.5). This result is consistent with PL spectra of the samples. In brief, the synthesized nanocomposite with suitable concentration of SnPc can be used to construct CeO_2 phosphors for near-ultraviolet (NUV) light-excited greenish-blue light-emitting diodes (LEDs) [18] .

Table 6.5 Chromaticity coordinates of CeO_2 nanoparticles and CeO_2/SnPc nanocomposite

Sample	*x*	*y*
S1	0.18846	0.26176
C2	0.1756	0.2811

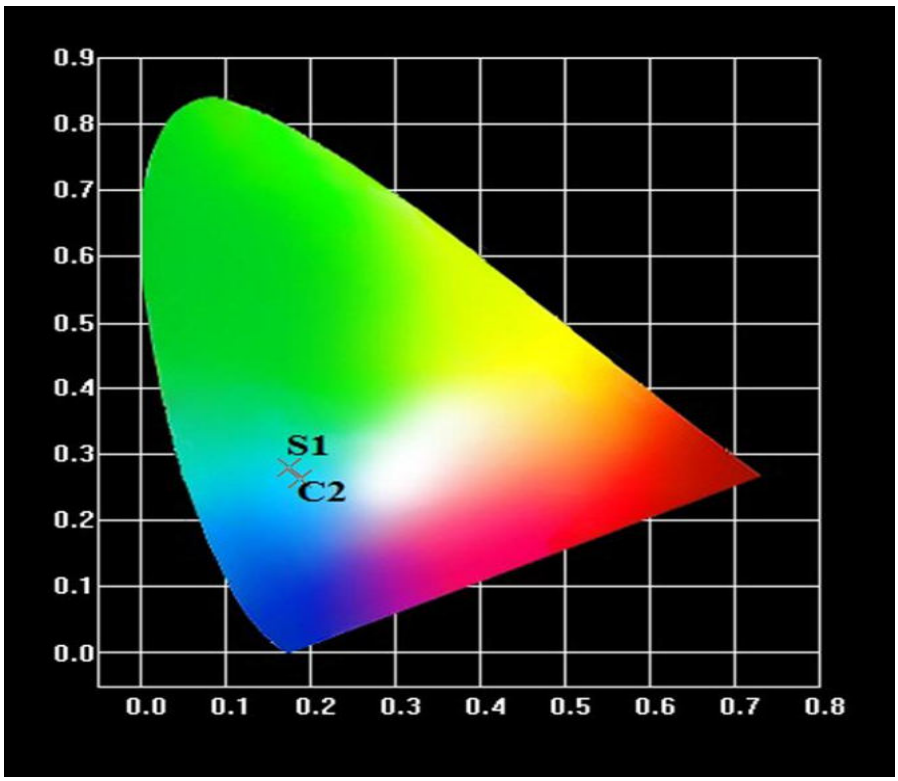

Fig.6.13 CIE chromaticity diagram of CeO_2 nanoparticles and CeO_2/SnPc nanocomposite

6.3.4 Electrical properties

The electrical studies are carried out by following the procedure given in *Section 2.4.4.* In order to study conduction mechanism and dielectric properties of CeO_2/SnPc nanocomposite, powder samples are

consolidated in the form of cylindrical pellet of diameter 13 mm and thickness 1.4 mm. Both the faces of the pellets are covered with air drying silver paste for good electrical contact. Dielectric measurements as a function of frequency in the range of 100 Hz−10 MHz are measured at various temperatures (303, 393 and 423 K) using Wayne Kerr H-6500B model impedance analyzer.

6.3.4.1 Frequency and temperature dependence of dielectric constant

The characteristic dependence of dielectric constant of CeO_2/SnPc sample with frequency for different temperatures are displayed in Fig. 6.14. From the figure, it can be observed that the dielectric constant shows an increase with temperature, but a decrease with frequency. At room temperature, the value of ε' is 37 at 100 Hz and remains almost unaltered at frequencies above 1 MHz. The dielectric constant is high in the low frequency region, exhibits a gradual decrease with increase in frequency and attains almost constant value in the high frequency regime. This is a normal dielectric behaviour arising due to Maxell-Wagner type polarization mechanism as explained in Koop's phenomenological theory [19, 20]. The variation of dielectric constant with frequency is clearly explained in the *Section 3.3.4.1*. Interfacial polarization plays a major role in this case. The value of ε' changes from 37 to 50, when temperature varies from 303 to 423 K. The observed

behavior revealed that the material exists in the form of molecular dipoles, which remain frozen at low temperature, while at high temperature the dipoles rotate freely and increase the orientation polarization [21], which in turn results in the increase in dielectric constant.

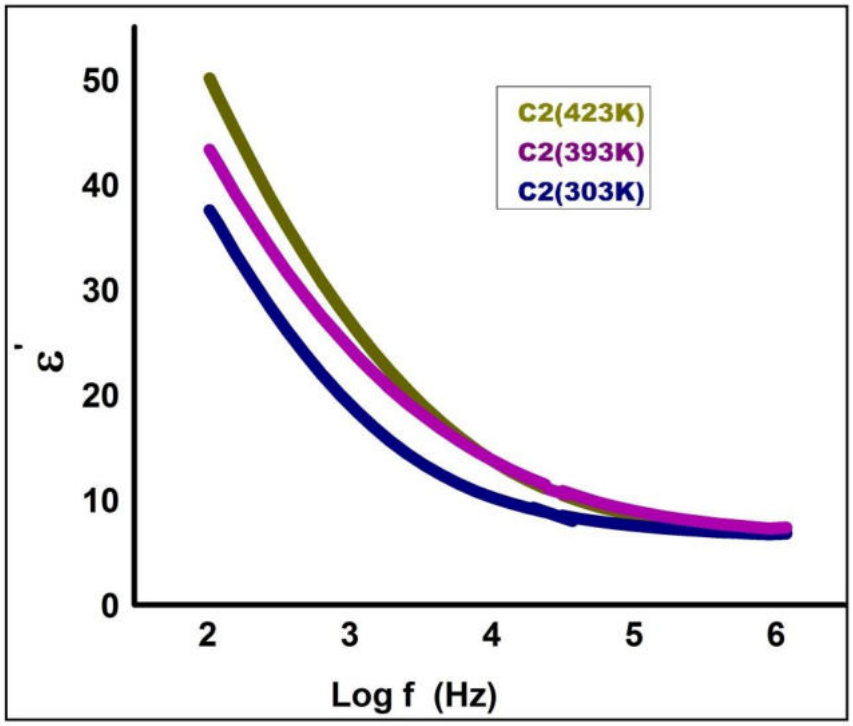

Fig.6.14 Variation of dielectric constant of CeO_2/SnPc nanocomposite with frequency at different temperatures

Fig. 6.15 shows that the dielectric constant is low for the nanocomposite sample as compared to nanophase CeO_2. At room temperature, the value of ε' is 66 at 100 Hz for the CeO_2 nanoparticles. The addition of SnPc into CeO_2 reduces the value of the dielectric constant from 66 to 37 (100 Hz) at room temperature. The decrease in dielectric constant for the nanocomposite is due to changes in the space

charge distribution caused by the addition of SnPc [22]. The considerably low values of dielectric constant is probably due to the submicroscopic inhomogeneities, presence of impurities such as oxygen in the samples and the low packing density of the synthesized materials [23], thus keeping the stronger influence of M-Pc in nanoceria.

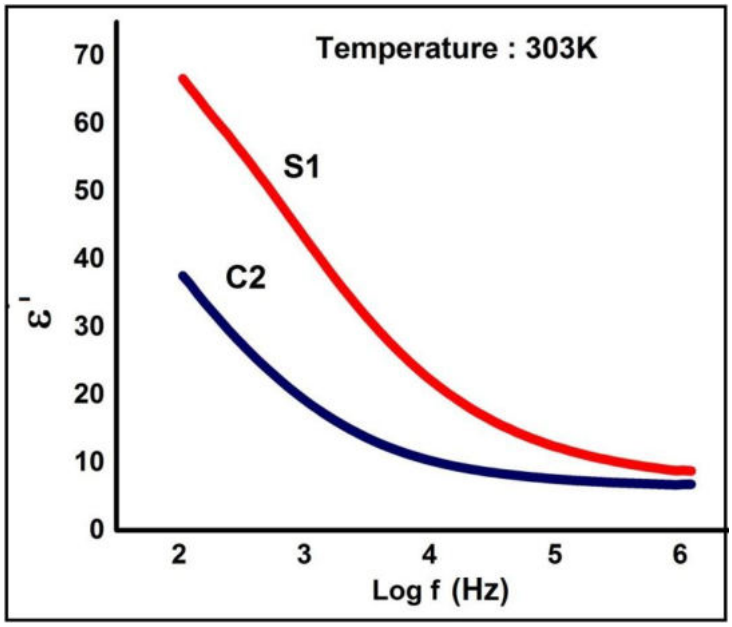

Fig.6.15 Variation of dielectric constant with frequency of CeO_2 and CeO_2/SnPc at 303 K

A low dielectric constant material is needed for substrate applications to avoid signal delay [24], whereas a high dielectric constant is preferred for miniaturization [25]. The low dielectric constants and loss factor values favour the use of the composite material in substrate applications and in low temperature co-fired ceramic (LTCC) modules as 3D wiring for circuit boards [26].

6.3.4.2 Frequency and temperature dependence of tangent loss

The dielectric loss originates from conduction loss, dipole loss and vibrational loss [27]. As the temperature increases, the AC conductivity σ_{ac} increases, which increases the electrical conduction loss and hence, the tangent loss [28]. The variation of *Tanδ* with frequency and temperature for CeO_2/SnPc nanocomposite sample is displayed in Fig. 6.16. It can be observed that the values of *Tanδ* initially decrease with frequency and then remain almost unaltered at higher frequencies. At 303 K, the value of *Tanδ* is 0.47 at 100Hz. As the frequency of the applied field increases the absorption current gets reduced, so the tangent loss will be decreased.

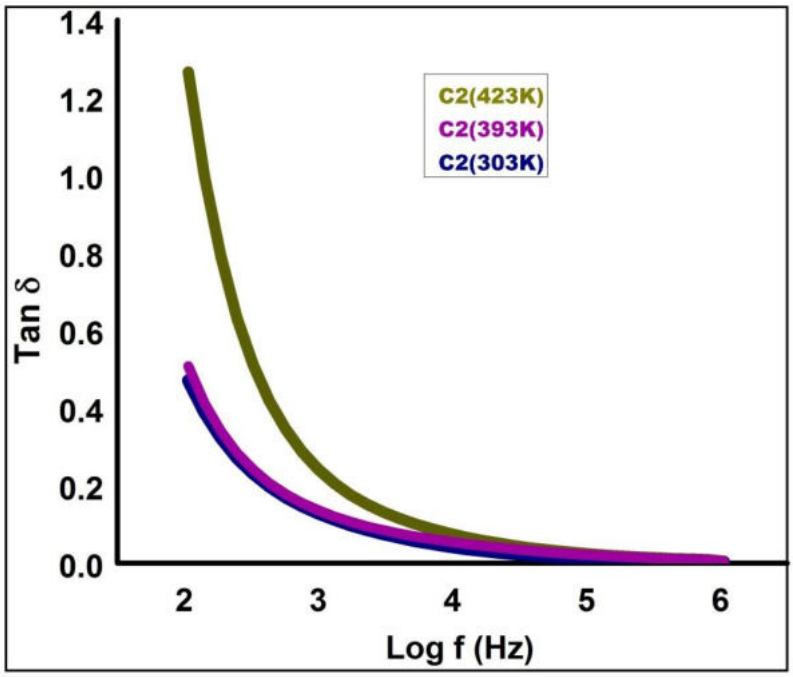

Fig.6.16 Variation of tangent loss with frequency of CeO_2/SnPc at different temperatures

The dielectric loss for the sample C2 is small as compared to S1, as shown in Fig.6.17. The presence of SnPc changes the *Tanδ* value of nanoceria from 7 to 0.47 at 100 Hz. CeO_2/SnPc nanocomposite with low values of dielectric constant and loss tangent at low temperature is important for the fabrication of materials for ferroelectric, photonic, microelectronic and optoelectronic devices [29].

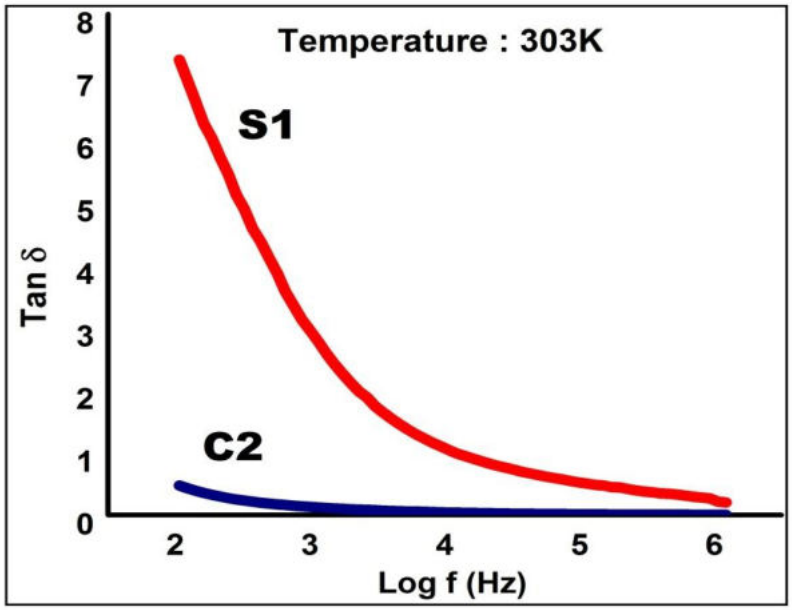

Fig.6.17 Variation of tangent loss with frequency of CeO_2 and CeO_2/SnPc at 303 K

6.3.4.3 Frequency and temperature dependence of AC conductivity

The relaxation of an electric field in a charge carrier system is attributable to the charge hopping of mobile carriers, which can lead to both short-range AC conductivity and long-range DC conductivity [30]. The variation of AC electrical conductivity of CeO_2/SnPc as a function of frequency at different temperatures is presented in Fig.6.18. Microstructure of the samples plays a key role in the frequency

dependence of conductivity [1]. It can be seen from Fig.6.18 that the conductivity increases with frequency, which confirms small polaron transport or hopping of holes in the sample [31]. As the frequency of the applied field increases, hopping of holes also increases there by increasing the conductivity. When temperature increases, there is easy transition of charge carriers from valence band to conduction band due to small-size of particles in the sample, which results in increased conductivity [32, 33].

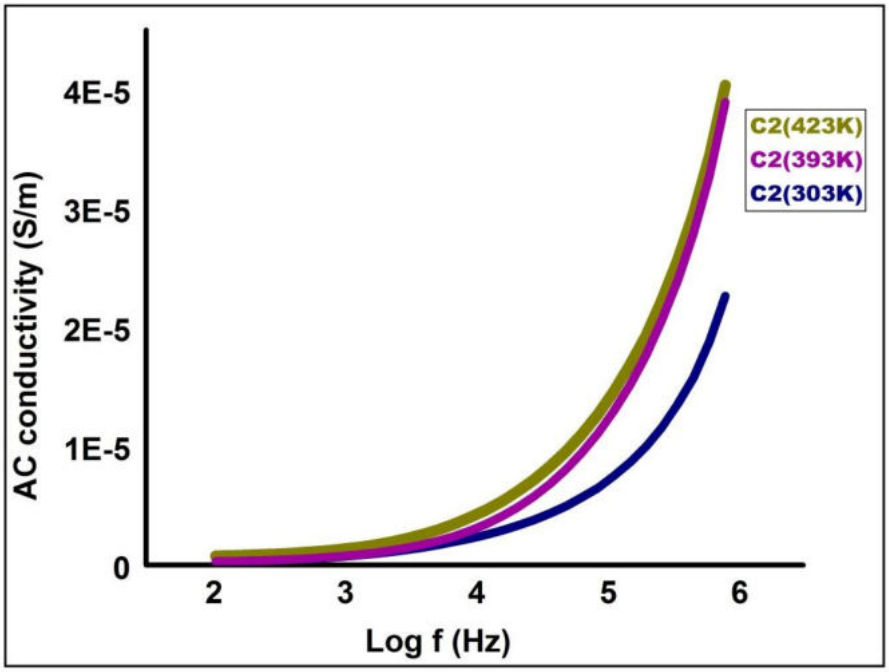

Fig.6.18 Variation of AC conductivity with frequency of CeO_2/SnPc at different temperatures

Fig. 6.19 compares the AC conductivity of CeO_2/SnPc with nanoceria. The figure demonstrates a decrease in AC conductivity of CeO_2 when SnPc is added. This may occur due to trapping of charge carrier (holes) between localized sites [34].

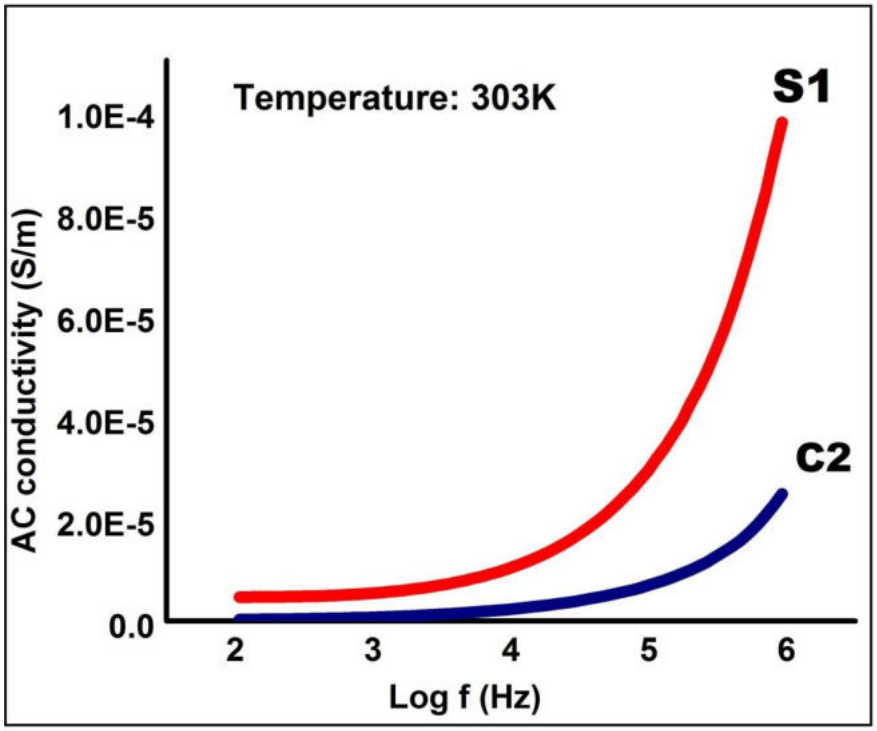

Fig.6.19 Variation of AC conductivity with frequency of CeO_2 and CeO_2/SnPc at 303K

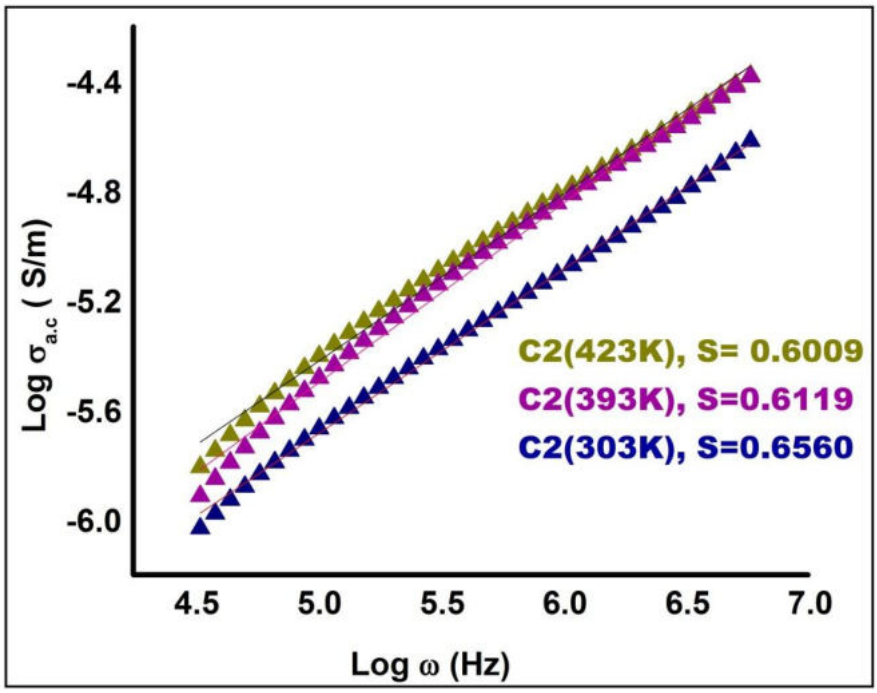

Fig.6.20 *Log(σ_{ac})* versus *log(ω)* plots of CeO_2 /SnPc nanocomposite

Figure 6.20 shows the $log(\sigma_{ac})$ versus $log(\omega)$ plots of the synthesized nanocomposites at different temperatures. Values of the frequency exponent *S* are calculated from the slope of the straight lines of the data presented in Fig.6.20. It is found that the value of *S* decreases (0.6560 to 0.6009) with increase in temperature from 303 to 423 K for the CeO_2/SnPc nanocomposite. The values of *S* of all samples lies between zero and unity, indicating that hopping is the main conduction mechanism thereby proving the Jonscher's universal power law [35].

6.4 Conclusions

- CeO_2/SnPc nanocomposite with an average particle size of 7.5 nm are successfully synthesised by solvent evaporation method.
- The TGA/DTA/DTG studies confirm that the composite is thermally stable in the range 300–700 ^oC .
- The structural properties of the nanocomposite sample is characterized by XRD, TEM, FTIR and Raman studies, and their results confirm the formation of CeO_2/SnPc in the sample.
- Compositional analysis using EDX detects the presence of cerium, tin, carbon, oxygen and nitrogen in the synthesized nanocomposite
- FTIR and Raman spectroscopic studies confirm the successful attachment of SnPc in CeO_2.

- UV–vis absorption studies indicate that nanocomoposite has good light absorption in the UV and visible region. The optical band gap values obtained is 3 eV for CeO_2/SnPc nanocomposite. A decrease in band gap energy together with an improved absorption intensity of the composite has been observed.
- PL spectra and CIE diagram show the existence of wide emission peaks in the greenish-blue region, when excited with near-ultraviolet light. This makes CeO_2/SnPc a promising material in photocatalytic, solar cells, NUV light-excited LEDs, and optoelectronics applications.
- Dielectric constant, tangent loss and electrical conductivity of CeO_2/SnPc nanocomposite is found to depend on both temperature and frequency.
- The dielectric constant and tangent loss decreases with increase in frequency and reaches a steady low value in the high frequency region. The nature of the curves remained the same when the temperature is raised, but the values are shifted upwards.
- The AC electrical conductivity of nanocomposite has a small value at low frequency region, which increases rapidly as frequency is increased. It conforms small polaron hopping and thus, electronic barrier hopping model. Electrical conductivity follows Jonscher's universal power law.

- It is observed that the dielectric constant (ε′), the loss factor (*Tanδ*) and the AC conductivity (σ_{ac}) for the CeO_2/CoPc nanocomposite are lower than those of nanoceria.
- The desired structural, optical and electrical properties of CeO_2/SnPc nanocomposite can make it a promising material for potential electronics applications.

References

[1] K. K. Babitha, K. P. Priyanka, A. Sreedevi, Bincy Abraham, J. K. Thomas and Thomas Varghese , J. Mater. Sci: Mater. Electron., 28 (2017) 1115–1123.

[2] A. A. Ansari, M. A. M. Khan, M. N. Khan, S. A. Alrokayan, M. Alhoshan, M. S. Alsalhi, J. Semiconduct., 32 (2011)1.

[3] P. H. Cury Camargo, K. G. Satyanarayana, F. Wypych, Mat. Res.,12 (2009)1.

[4] B. D. Cullity, Elements of X-Ray Diffraction, Addison-Wesley, MA (1967).

[5] G. K. Williamson and W. H. Hall, Acta. Metall., 1(1953) 22.

[6] S. B. Khan, M. Faisal, M. M. Rahman, A. Jamal, Sci. Total Environ.,409 (2011) 2987–2992

[7] F. Niu et al., Mater. Lett., 63 (2009) 2132–2135.

[8] Pawan Kumar, Arvind Kumar, Chetan Joshi, Raghuvir Singh, Sandeep Saran, Suman L. Jain, RSC Adv. 5 (2015) 42414–42421

[9] S. Phoka, P. Laokul, E. Swatsitang, V. Promarak, S. S.eraphin, S.Maensiri, Mater. Chem. Phys. 115 (2009) 423–428 .

[10] K. K. Babitha, A. Sreedevi, K.P. Priyanka, Boby Sabu and Thomas Varghese, Indian J. Pure Appl. Phys.,53 (2015) 596-603.

[11] Carol Jennings, Richardo Aroca, Ah-Mee Hor and Rafik.O.Loutfy, Spectrochimi. Acta, Part A: Molecular Spectroscopy, 41(9) (1985) 1095-1099.

[12] Z. Wang, Z. Quan and Lin, J. Inorg. Chem., 46 (2007) 5237.

[13] K. R. Rajesh and C. S. Menon, Indian J. Pure Appl. Phys. 43 (2005) 964–971.

[14] M. J. Stillman, T. N. Nyokong, in Phthalocyanines: Properties and Applications, vol. I, eds. by C.C. Leznoff, A B P Lever (VCH publishers lnc., New York, 1989), Chap. 3.

[15] S.B. Brown, Introduction to Spectroscopy for Biochemistry (Academic Press, London, 1980).

[16] J. Tauc, Amorphous and Liquid Semiconductors, 1 ed.Plenum Press, New York (1974).

[17] K. K. Babitha, K. P. Priyanka, A. Sreedevi, O. P. Jaseentha and Thomas Varghese. Int. J. Appl. Ceram. Technol., (2016) 1–8.

[18] F. Hussain, M. Hojjati, M. Okamoto, and R. E. Gorga, J. Compos. Mater., 40(17) (2006) 1511–1575.

[19] C. G. Koops, Phys. Rev., 83 (1951) 121-124.

[20] K. W. Wagner, Am. Phys., 40 (1973) 317.

[21] K. K. Srivastava, A. Kumar, O. S. Panwar, L. N. Laksh minarayan, J. Non-Cryst. Solids, 33 (1979) 205.

[22] G. C. Montanari, D. Fabiani, F. Palmieri, D. Kaempfer, R. Thomann, and R. Mulhaupt, IEEE Trans. Dielectr. Electr.Insul., 11 (2004) 754.

[23] A. M. Saleh, S. M. Hraibat, R. M. L. Kitaneh, M. M. Abu-Samreh, S. M.Musameh, J. Semicond., 33(8) (2012).

[24] R. R. Tummala Rao, J. Am. Ceram. Soc., 74(5) (1991)895-908.

[25] K. M. Long, K. M. Luk, IEEE Antenna Propag., 43 (1995).

[26] S. Vidya, S. Solomon, J.K. Thomas, J. Mater. Sci. Mater. Electron. (2015); doi:10.1007/s10854-015- 2823-8.

[27] J. M. Stevels, in Handbush der Physics, Springer, Berlin (1957) 307.

[28] M. M. El-Nahass, A. M. Farid, K. F. Abd, K. F. Abd El-Rahman, H. A. M. Ali, Physica B, 403 (2008) 2331–2337.

[29] K. P. Priyanka, K.K. Babitha, A. Sreedevi, X. Sheena, E. M. Mohammed, T. Varghese, J. Electroceram.32(4) (2014) 361-368; doi:10.1007/s10832-014-9919-z.

[30] D. K. Ray, A. K. Himanshu, T. P. Sinha, Indian J. Pure Appl. Phys., 45(2007) 692–699.

[31] P. S. Vijayakumar, H. Pohl, J. Polym. Sci. Polym. Phys., 22 (1984) 1439.

[32] M. K. Akhtar, Y. Xiong, S.E. Pratsinis, AIChE J. 37 (1991) 1561.

[33] Z. Ding, X. Hu, G.Q. Lu, P.L. Yue, P.F. Greenfield, Langmuir 16 (2000) 6216.

[34] K. K. Babitha, K. P. Priyanka, H. Hitha, S. Rintu mary, E. M. Mohammed, S. Sankararaman, and Thomas Varghese J Electron. Mater., (2017) DOI: 10.1007/s11664-017-5653-z.

[35] B. M. Greenhoe, M. K. Hassan, J. S. Wiggins, K. A. Mauritz, J. Polym. Scie. Part B: Polymer Physics, (2016); DOI: 10.1002/polb.24121.

..... ❀ .....

Chapter 7

SUMMARY AND SCOPE FOR FUTURE WORK

The main objective of the present study, as brought out in section 1.3, is to synthesize and characterize cerium oxide nanoparticles and their phthalocyanine nanocomposites (CeO_2-CoPc/SnPc). The research work has been systematically described in 7 chapters. A general introduction on nanomaterials and nanoceria is presented in Chapter 1. CeO_2 nanocrystals are synthesized using simple chemical precipitation method and are characterized using various tools as mentioned in Chapter 2. The structural, optical and electrical characterizations of the synthesized CeO_2 nanoparticles before and after electron beam irradiation are presented in Chapters 3 and 4 respectively.

Phthalocyanine (CoPc/SnPc) composites of CeO_2 are synthesized by solvent evaporation method and their properties are investigated using structural, optical and electrical characterization techniques. The method of synthesis and characterization results of CeO_2/CoPc and CeO_2/SnPc along with discussion are presented in Chapters 5 and 6 respectively.

A summary of the synthesis and characterization of cerium oxide nanoparticles and their phthalocyanine nanocomposites (CeO_2-CoPc/SnPc) and dose dependent effect of electron beam irradiation on the properties of cerium oxide nanoparticles is presented in the current chapter. The important outcomes, promising applications of the materials synthesized and an outline of future prospects are mentioned as concluding remarks of the chapter.

7.1 Summary of the Present Work

Cerium oxide nanoparticles are successfully synthesized by chemical precipitation method and are characterized by various tools. TGA/DTA analysis shows that the material is thermally stable in the temperature range of 200-850°C. The effect of calcination temperatures (400, 550, 700 and 850°C) on the structural, optical and electrical properties of the cerium oxide nanoparticles are studied and it was found that it results in an increase in intensity of diffraction peaks, decrease in FWHM, increase in crystallite size, decrease in micro-strain and dislocation density, decrease in lattice constant and unit cell volume. XRD analysis confirms cubic fluorite structure for CeO_2. An average particle size of 7.3 nm is estimated for CeO_2 nanoparticles calcined at 400°C. The average crystallite size of nanophase CeO_2 is found to increase with increase in the calcination temperature due to the thermally promoted crystallite growth. TEM results provide a clear picture for

grain growth and increase in crystallinity due to calcination. HRTEM image shows the polycrystalline nature of the sample. SEM analysis shows that particles are not in uniform shape and are agglomerated. The EDX analysis confirms the presence of all the elements expected for CeO_2. FTIR and Raman spectra results confirm the formation of CeO_2. Raman bands are red shifted and their intensity is found to increase with increase in calcination temperature.

Optical absorption spectra show that synthesized cerium oxide nanoparticles have good UV absorption. CeO_2 calcined at 400^oC has an optical band gap of 3.42 eV. The optical band gap values are found to decrease with the increase in calcination temperatures. PL bands are modified and shifted towards blue region with the increase in calcination temperature. The intensity of PL emission bands are found to decrease with the increase in calcination temperature due to the increase of particle size. Greenish-blue emission of CeO_2 nanoparticle is confirmed by CIE chromaticity diagram. Present studies indicate that non-stoichiometry, defects and size variation of particles have a great influence on optical band gap, PL and Raman band modification. The observed optical properties of CeO_2 nanoparticles show that it is a promising material for photocatalytic, cosmetic and optoelectronic applications.

The effect of calcination on the electrical properties of the synthesized nanoparticles is also investigated and it was found that room temperature dielectric constant obtained for CeO_2 nanoparticles calcined at 400^oC is 66 at 100 Hz, which constitutes the highest value ever reported. This indicates that CeO_2 nanoparticle could be a promising material for the high dielectric gate in CMOS devices. The values of dielectric constant and dielectric loss are found to increase with the increase in temperature and to decrease with the increase in frequency. It is also found that the values of dielectric constant, dielectric loss and AC conductivity are decreased as calcination temperature is raised. Frequency dependent polaron hopping mechanism in AC conductivity is confirmed by Jonscher's power law.

The effect of 8 MeV electron beam irradiation on the thermal, structural, optical and electrical properties of cerium oxide nanoparticles are investigated. It is found that electron beam irradiated CeO_2 samples show a decrease in crystallite size with lattice expansion. XRD results show that CeO_2 nanoparticles with average particle size 7.3 nm is decreased to 5 nm when irradiated with 5 kGy electron beam. But the size of CeO_2 nanoparticle is reduced only up to 6.4 nm after a dose of 10 kGy irradiation. TEM, SEM, FTIR and Raman studies confirm structural modifications of the electron irradiated CeO_2 samples. Electron beam irradiation introduced defects in the lattice of CeO_2. A band gap of 3.59

and 3.45 eV are obtained for CeO_2 irradiated with 5 and 10 kGy respectively. Improvement in the intensity of absorption peak suggests that the irradiation produced sufficient defects. The increase in PL intensity indicates higher photocatalytic activity for the irradiated samples. Furthermore, the defects and crystallite size variation result in large micro-strain and dislocation density, enhanced optical band gap as well as photoluminescence intensity, broadening of Raman line and reduction of Raman intensity.

EB irradiation produces high dielectric constant, dielectric loss and AC conductivity for cerium oxide nanoparticles. The dielectric constant of CeO_2 nanoparticle is changed from 66 to 1750 at 100Hz, when it is irradiated with a dose of 5 kGy electron beam. EB irradiation leads to faster ionic transport in the material, which results in high conductivity. In short, high energy EB irradiation of a suitable dose can help us to enhance the structural, optical, photoluminescence and electrical properties of CeO_2 nanoparticles for micro- and optoelectronics applications.

Solvent evaporation method has been successfully employed for the synthesis of CeO_2/CoPc nanocomposite. TGA/DTA/DTG studies confirm that the composite is thermally stable in the range 120–700°C. The structure and morphology of the nanocomposite are characterized by XRD, TEM and SEM. Average particle size is found to be 7.72 nm for

the composite. Compositional analysis using EDX confirms the presence of all the elements expected for the CeO_2/CoPc nanocomposite. Formation of the various bonds in CeO_2 and CoPc is confirmed through FTIR spectrum analysis. Raman spectroscopic studies confirmed the successful attachment of CoPc on CeO_2 by showing the presence of Raman active modes of both CeO_2 and CoPc in the spectrum.

Optical absorption studies show that CeO_2/CoPc nanocomposite has an extended light absorption from UV to visible region. In addition, a decrease in bandgap energy together with an improved absorption intensity of the nanocomposite is observed. A band gap of 2.9 eV is obtained for CeO_2/CoPc nanocomposite. PL spectrum and CIE diagram show the existence of wide emission peaks in the greenish-blue region when excited with near-ultraviolet light. The intensity of PL spectrum is found lower for CeO_2/CoPc nanocomposite.

The addition of CoPc into CeO_2 reduces the value of the dielectric constant from 66 to 39 (100 Hz) at room temperature. Low values of loss tangent indicate that the synthesized nanocomposite can have high frequency applications. AC conductivity in CeO_2/CoPc nanocomposite is observed to be dependent on Jonscher's power law which confirms conduction by polaron hopping. Moreover, the modified structural and electrical properties of the CeO_2/CoPc nanocomposite can be used for the

fabrication of materials for photonic, microelectronic and electro-optic devices.

CeO_2/SnPc nanocomposite is successfully synthesized by solvent-evaporation method and its thermal, structural, optical and electrical properties were studied. XRD analysis shows that average crystallite size obtained for CeO_2/SnPc is 7.5 nm. Thermal analysis shows that the synthesized nanocomposite sample is thermally stable in the range of 300-700^{o}C. HRTEM image shows the polycrystalline nature of the sample. Both TEM and SEM results show that particles are not in uniform size and shape and that they are agglomerated. Compositional analysis using EDX detects the presence of cerium, tin, carbon, oxygen and nitrogen in the CeO_2/SnPc nanocomposite. Raman spectroscopic studies confirm the successful attachment of SnPc on CeO_2 by showing the presence of Raman active modes of both CeO_2 and SnPc in the spectrum.

Optical absorption analysis shows that the optical absorption spectrum of CeO_2 is extended from the UV region to the entire span of visible light when SnPc is added into it. An optical band gap of 3 eV is obtained for CeO_2/SnPc. Improved absorption intensity, red shift in absorption bands and decreased optical band gap are observed for the nanocomposite. PL spectra and CIE diagram of CeO_2/SnPc nanocomposite show the existence of wide emission peaks in the

greenish blue region, when excited with near-ultraviolet light. The intensity of PL spectra is lower for CeO_2/SnPc nanocomposite.

The electrical properties of the nanocomposite strongly depend on frequency and temperature. The addition of CoPc into CeO_2 reduces the value of the dielectric constant from 66 to 37 (100 Hz) at room temperature. AC studies prove the Jonscher's power law dependence of AC conductivity in CeO_2/SnPc nanocomposite and confirm polaron hopping. The low dielectric constants and loss factor values favour the use of the composite in substrate applications in low temperature co-fired ceramic (LTCC) modules as 3D wiring in circuit boards.

7.2 Major Findings of the Study

The important outcomes of the present investigation have been listed below.

- Cerium oxide nanoparticles are synthesized by simple chemical precipitation method without using any capping agent.
- Studies based on the effect of calcination temperature confirm changes in the structural, optical and electrical properties of CeO_2 nanoparticle.
- Room temperature dielectric constant obtained for the synthesized CeO_2 nanoparticle sample is 66 at100 Hz, which constitutes the highest value ever reported.

- The electron beam irradiation with 5 kGy dose offers high value of dielectric constant (1750 at 100 Hz) at room temperature.
- The electron beam irradiation produces changes in the structural properties of cerium oxide nanoparticles, which results in the modifications of their optical and electrical properties. This is the first report of the influence of high energy electron beam irradiation on the structural, optical and electrical properties of CeO_2 nanoparticle.
- Electron beam irradiation with a suitable dose can be applied for tuning band gap, photoluminescence and dielectric properties of cerium oxide nanoparticles for potential applications.
- The room temperature dielectric constant of CeO_2 irradiated with a dose of 5 kGy electron beam is 1750 at 100Hz.
- CeO_2/CoPc and CeO_2/SnPc nanocomposites are successfully synthesized by simple solvent evaporation method.
- The addition of M-Pc (Co, Sn) in CeO_2nanoparticles can extend the optical absorption spectra of CeO_2 from the UV region to the entire span of visible light.
- The modified structural, optical and electrical properties of the CeO_2-CoPc/SnPc nanocomposites can be used for the fabrication of materials for photonic, microelectronic and optoelectronic devices.

7.3 Scope for Future Work

The work presented in this thesis can be extended in several directions and are briefly presented as follows:

- Cerium oxide nanoparticles are reported to have multiple applications. More extensive and systematic studies are required to explore their potential applications.
- The study can be extended to analyze the applications of CeO_2/CoPc and CeO_2/SnPc nanocomposites.
- Further studies are needed for understanding the effect of EB irradiation on the properties of CeO_2/CoPc and CeO_2/SnPc nanocomposites.
- More extensive and systematic studies on the structural and electrical properties of CeO_2 nanoparticles and EB irradiated CeO_2 are needed to explore their novel properties for applications in CMOS devices.

....